INSTITUTO TECNOLÓGICO DE BUENOS AIRES – ITBA
DEPARTAMENTO DE INGENIERÍA MECÁNICA

Diseño y Análisis de un Sistema de Propulsión para CubeSats basado en Vapor Sobrecalentado

AUTORES: Giraudy, Tomás (Leg. Nº 56386) - Scarone, Franco (Leg. N° 56036)

DOCENTE TITULAR: Dr. Ing. Leslabay, Pablo

TRABAJO FINAL PRESENTADO PARA LA OBTENCIÓN DEL TÍTULO DE INGENIERO MECÁNICO

BUENOS AIRES

PRIMER CUATRIMESTRE, 2022

Resumen

En este trabajo se diseña un sistema de propulsión orbital de gas caliente del tipo Resisto-Jet a base de agua, para su implementación en Cube- y MicroSats de al menos 6U, como sistema de maniobra orbital. Se busca obtener un dispositivo autocontenido en 1U, con un tanque auto presurizado de agua líquida al momento de operación, que evite la introducción de bombas o de sistemas de presurización externa. Se busca minimizar la utilización de partes móviles, y el uso de materiales tóxicos o restringidos. El aprovechamiento del calor interno de este tipo de satélites previene el congelamiento generalizado del equipo, y la necesidad de realizar precalentamiento de trabajo para mejorar la eficiencia asegura que todos los conductos y válvulas del dispositivo estén por encima de la temperatura de congelamiento del propelente al momento de dispararlo. El sistema propuesto consiste en un tanque con el propelente, un tanque auxiliar presurizado por la presión de vapor a la temperatura de trabajo, para este diseño particular establecida en 73ºC, un evaporador de agua separado del tanque por una válvula, y que retiene al propelente en posición aprovechando a su propia tensión superficial y el reducido gradiente de presiones dentro del dispositivo, y un sobrecalentador por resistencia eléctrica que eleva la temperatura del flujo másico evaporado, a su vez contribuyendo a la evaporación del paso previo a través de un diseño anidado que permite reutilizar las pérdidas de calor por radiación. Se utilizan modelos analíticos en estado estacionario de termodinámica y transferencia de calor para definir las dimensiones de los componentes internos y la reutilización de calores, cumpliendo con cotas de potencia y de energía disponible en las baterías típicas de un CubeSat. Una eficiencia de potencia de entre un 78 y 81% es esperada, mientras la eficiencia energética esperada de cada ciclo de impulso es de entre un 62 y un 67%. Se espera obtener valores de impulso específico de entre 171 y 172s al eyectar vapor de agua a baja presión a por lo menos 900°C a través de una tobera convergente-divergente. El budget de potencia disponible para la propulsión se establece en 50W. Como ejemplo se genera un sistema para un CubeSat de 6U con una masa de 10Kg y ΔV de 50m/s, con empuje de 16mN y 250g de propelente requeridos. El modelo analítico y paramétrico introducido en este trabajo permite generar los cambios necesarios para adaptar el sistema de propulsión a diferentes misiones, siempre manteniendo la eficiencia. El empuje generado dependerá de la potencia disponible, y en parte de la energía total asignada a la propulsión. El ΔV total dependerá exclusivamente de la masa de propelente disponible. Se presenta un plan de ensayos, aprovechando la cámara de vacío disponible en la universidad. Esto permite caracterizar y validar los distintos componentes del sistema de propulsión. Se espera poder medir el flujo másico, el empuje e impulso específico del prototipo en un futuro cercano.

Palabras clave: Monopropelente, Propulsión eléctrica, Resistojet, CubeSat, Vapor sobrecalentado

Abstract

An H2O ResistoJet type propulsion system is designed for its use in CubeSats larger than 6U as an orbital maneuvering system. Designed to be self-contained in one unit, its electrically heated evaporator, and superheater systems are fed by a self-pressurized liquid water tank, thus characterized by its simplicity due to the lack of pumps or external pressurizing systems. Moving parts and the use of toxic materials are minimized. Internal heat from these satellites prevents equipment freezing, and the need to preheat the system to improve efficiency ensures that all ducts and valves of the device are above the propellant's freezing temperature before firing it. The proposed system consists of a propellant tank, with an auxiliary tank pressurized by water's vapor pressure at the system's working temperature established at 73°C for this design, a water evaporator separated from the tank by a valve retaining propellant in position, taking advantage of its surface tension and the reduced pressure gradient in the device, an electrically powered superheater that raises the temperature of the evaporated mass flow as well as contributing to the previous step's evaporation through a nested design that allows the device to reuse radiation lost heat, and an EDM manufactured convergent-divergent nozzle that discharges the hot fluid to generate thrust, resulting in efficient and clean propulsion. Steady-state thermodynamic and heat transfer analytical models are used, defining the dimensions and materials of the inner components to meet the power and energy restrictions of a typical CubeSat battery system. A steady-state power conversion efficiency between 78% and 81% is expected, while the energy conversion efficiency expected in each impulse event is expected between 62% and 67%. The expected specific impulse is 171-172s, ejecting low-pressure steam reaching the nozzle at a temperature above 900°C. The power budget available for propulsion is established at 50W. As an example, a device is generated for a 6U CubeSat with a mass of 10Kg and a ΔV of 50m/s, with 16mN thrust and 250g of required propellant mass. The analytical and parametric model introduced in this work gives the ability to make changes necessary to adapt the propulsion system to different missions, maintaining efficiency. Generated thrust depends exclusively on the available power and the total energy assigned for propulsion. Total ΔV depends exclusively on the mission requirements, which are easily regulated with the available propellant mass. A test plan is presented, taking advantage of the vacuum chamber available at the university. This allows for characterization and validation of the different propulsion system components. It is expected that the prototype's mass flow, thrust, and specific impulse could be measured in the near future.

Keywords: Monopropellant, Electric propulsion, Resistojet, CubeSat, Superheated steam

Contents

List of Figures

List of Tables

1 Introduction

Nowadays, the space industry is undergoing a new age thanks to the widespread use of CubeSats (figure 1.1). These are nanosatellites made of multiple modular units 100 mm x 100 mm x 110 mm in size with a weight of up to $1.33Kg$ each, allowing for a flexible, quick, and cheap design. Because of their size and weight, CubeSats can be deployed in constellations enabling the possibility of multi-point sensing, making more data available for decision making, and enhancing coverage with a reduced cost. The most common layouts are 3U, 6U (2x3), and 12U (4x3) referring to the number of modules involved. Cubesats' structure is mostly aluminum-based, although 3D printed structures with metallic plating have been used due to their lower weight. Deployable or body-mounted photovoltaic solar cells are used to harvest solar energy, according to their available surface and the payload's power requirement. Energy is stored in commercially available Li-Ion or Li-Po batteries, with bus voltages of up to $12V$, with capacities ranging between 20 and $80Wh$.

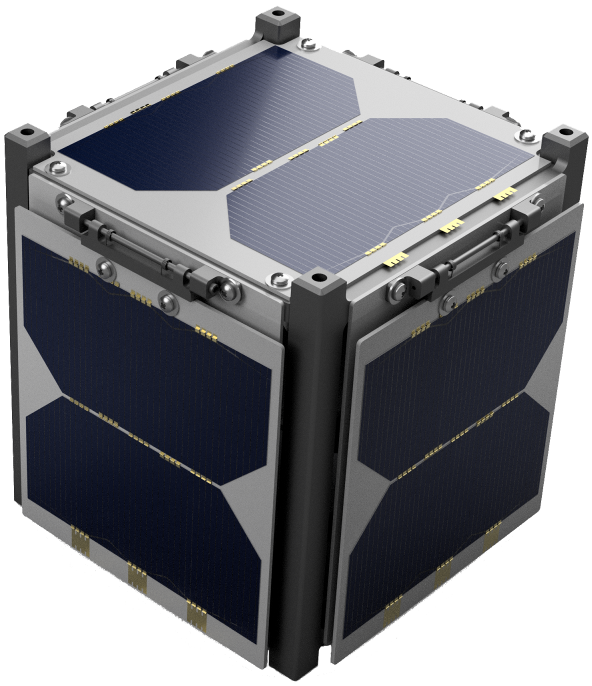

Figure 1.1: Typical 1U CubeSat

CubeSats can be categorized by their mission applications. These include, but are not limited to, the following [1]:

- **Earth science and spaceborne applications**
  Spaceborne Earth Observation helps understand Earth's evolution and environmental changes across time and space, making it useful for natural resources exploitation, and weather and climate change prediction. As an example, in 2014, 56 3U satellites were launched to form the FLOCK constellation, intended to provide daily earth imaging with a 3m to 5m resolution. Figure 1.2 shows 28 of the CubeSats [2].

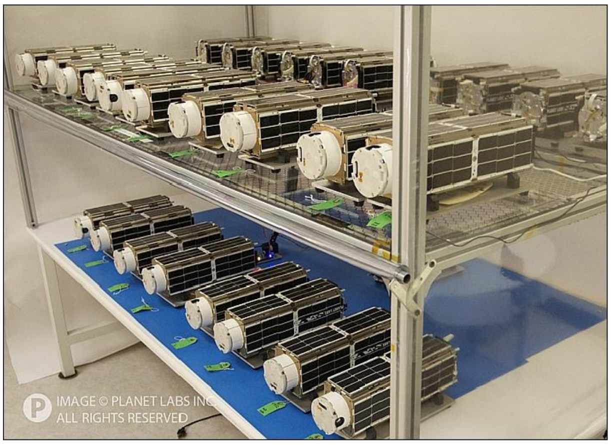

Figure 1.2: 28 Flock CubeSats before being sent to the launch site

- **Deep space exploration**
  The number of CubeSats being propelled beyond Low Earth Orbit (LEO) is increasing as of recent, performing science or technology missions in deep space. The Mars Cube One (MarCO) mission displayed in figure 1.3 consisted of two identical 6U CubeSats for supporting telecommunications relay during entry, descent, and landing of the InSight Mars Lander, which provides daily reports of weather in the surface of Mars [3].

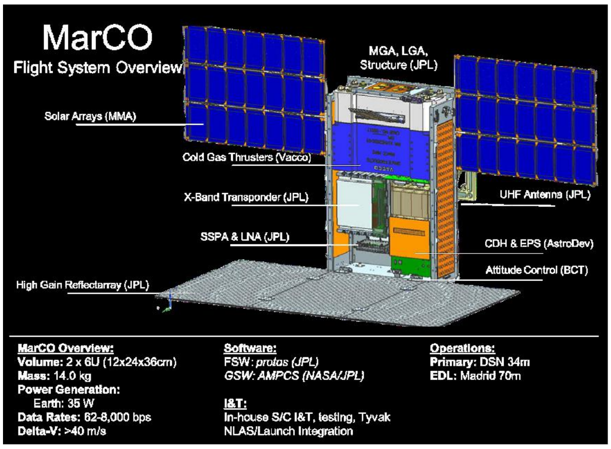

Figure 1.3: Overview of the MarCO CubeSat

- **Heliophysics: space weather**
  Conditions on the sun, solar wind, and within earth's ionosphere and magnetosphere are called space weather. They can damage technology such as terrestrial electric grids and deployed satellites in space, also putting tripulated missions at risk, particularly during future deep space exploration. To understand and predict the space weather effects CubeSats have been launched since 2010, such as the RAX-1 and RAX-2.

- **Astrophysics**
  For a better understanding of the universe and its evolution, satellites such as S-Cube were

launched. During 2016 S-Cube studied flux of meteors' composition and size.

- **Spaceborne in situ laboratory**
  CubeSats are used to study the effects of microgravity or space radiation during extended periods on biological organisms. Similar studies can be done on earth for a short amount of time, therefore more information is gained from performing them in space. PHARMASAT-1 studied the efficacy of an antifungal drug on a biological organism from 2009 to 2012.

- **Technology demonstration**
  CubeSats can be launched to study technologies intended to be used in bigger satellites and to demonstrate technologies to use in future CubeSats. GRIFEX3U, a 3U CubeSat launched in 2015, successfully tested an integrated circuit with a new image reading and processing technology, preparing it for its use in the GEO-CAPE mission concept: a geostationary satellite intended to study atmospheric chemistry and pollution transport.

To perform their tasks successfully key parameters of satellites need to be precisely controlled. Satellites such as PHARMASAT-1 and other spaceborne laboratories require strict temperature control for experiments to be conclusive. Both altitude and satellite orientation need to be controlled for image-providing satellites. Developments of subsystems regulating the key parameters previously mentioned, among others, will enhance and expand capabilities of CubeSats.

1.1 Propulsion systems

Propulsion systems are used for orbit correction and transfer, or to deploy and maintain constellations of satellites (benefits described in section 1). Except for electrostatic propulsion systems, all other systems use a convergent-divergent (CD) nozzle to increase the gas exhaust speed. The systems are characterized by the different mechanisms used to reach the needed gas enthalpy for the CD nozzle to transform it into kinetic energy.

Two basic parameters to characterize a propulsion system are thrust and specific impulse (I_{sp}). Thrust represents the force that moves the satellite forward. I_{sp} represents the change in linear momentum per unit of mass expelled and measures how efficiently gas enthalpy converts into thrust.

The most common types of propulsion systems are the following [4]:

- **Chemical thrusters**
  An exothermic chemical reaction of two components gives as a result a high temperature and enthalpy product which is expelled through the CD nozzle. The CubeSat's battery does not play a major role in terms of energy needed for operation, but a complex system is needed to store the reactive. Monopropellant thrusters catalytically decompose a liquid propellant, while in bipropellant thrusters either solid or liquid fuel reacts with an oxidizer.

- **Cold gas thrusters**
  These thrusters expel a pressurized cold gas, with its pressure regulated by a valve. The benefit of these systems is their simplicity, at the cost of low efficiency.

- **Electric thrusters**
  Batteries act as the primary energy source in these systems. Electric thrusters can be divided in three categories:
  - *Jets*: An electic resistor (resistojets) or an electric arc (arcjets) serve as the energy source for the fluid's enthalphy increase. These systems demand a lot of electric energy, but they can work with fluids at a lower pressure in comparison to cold gas thrusters or chemical thrusters.
  - *Electrostatic*: The gases are ionized and then directioned by an electric field. The same electric field accelerates the particles.
  - *Electromagnetic*: Similar to the electrostatic jets, they use a magnetic field instead of an electrical one.

The principal characteristics of the different propulsion systems are shown in table 1.1.1 [4].

Type	Propellant	I_{sp} [s]	Thrust [N]	Advantages	Disadvantages
Solid (chemical)	NH_4ClO_4 + Al + polymers	280-300	50-5·10^8	Simple Trustworthy Low cost	Limited performance One mode of operation High thrust
Liquid (chemical)					
Monopropellant	H_2O_2, N_2H_4	150-225	0.05-0.5	Simple	Low performance
Bipropellant	O_2 y RP-1, N_2O_4 and MMH	300-350	5-5·10^5	High performance	Complex
Cold gas	N_2, NH_3, Freon	50-75	0.05-200	Simple Trustworthy Low cost	Heavy Limited performance and not constant
Electric					Need energy from batteries
Resistojet	N_2, NH_3, H_2O	30-300	1·10^{-4}-0.5	High performance Low power	Low thrust
Arcjet	NH_3, N_2H_4, H_2	450-1500	0.05-5	High performance Simple feeding system	High power
Electrostatic	Hg/A/Xe/Cs	1200-6000	5·10^{-6}-0.5	High performance	High power Risky
Electromagnetic	Argon, N_2H_4	2000-4000	2-200	High performance	High power Risky

Table 1.1.1: Propulsion system comparison

Figure 1.1.1 from [5] shows a comparison of thrust versus specific impulse for different propulsion systems. Ion and electrospray systems fall under the electrostatic thrusters category, while hall and pulsed plasma systems fall under the electromagnetic thrusters category. Resistojets' thrusts range between 0.1 and 50mN, and I_{sp} ranges between 30 and 300s.

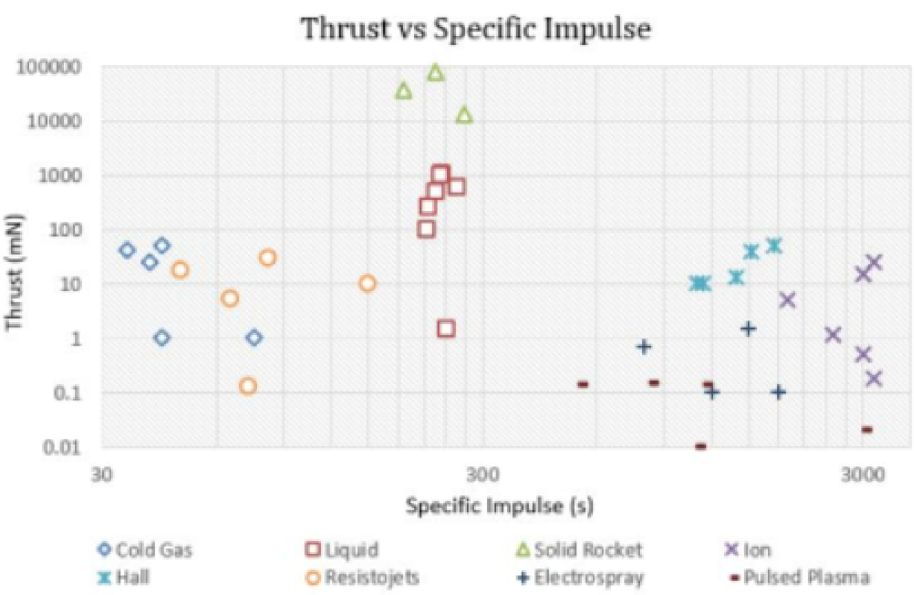

Figure 1.1.1: Thrust versus I_{sp} for various thruster types

2 Objectives

This project's objective is to design a resistojet type propulsion system for its use in CubeSat's orbital maneuvering system using superheated, self-pressurized steam as propellant and electricity as its energy source.

A resistojet type of propulsion system is chosen because of its simple design, with a higher specific impulse than simple cold-gas thrusters as seen in figure 1.1.1.

Resistojets are mainly static, with moving parts including actuators in vectorized one-nozzle designs, and valves such as on-off valves for standard operation, impulse bit propulsion, or thrust directioning systems in multiple nozzles systems. The amount of moving parts should be kept at a minimum, providing the highest achievable reliability, as failure events of the moving components must not be undermined since they would result in a failed mission.

To simplify the design even further, usage of pressurizing systems, such as pressurizing tanks or a high-pressure tank with a pressure regulator, is avoided, allowing the equilibrium between gaseous and liquid propellant to regulate the pressure inside the tank. Water saturation pressure is lower than 10kPa in usual satellite temperatures, resulting in storage and tubing of simple design. Furthermore, it has the added benefit of making the nozzle easier to fabricate as described in section 3.1.4.

Chemical, electrostatic and electromagnetic thrusters are discarded due to their design complexity. Liquid thrusters require the design of two high-pressure storage and feed systems for fuel/oxidizer or fuel/catalyzer in addition to a combustion chamber, which is also present in solid thrusters. As electrostatic and electromagnetic systems tend to require high power (>200W) to function, they are rarely used in a small CubeSat arrangement.

Model validation can be achieved by experimental testing as described in section 10. This experimental setup will measure the propulsion system's I_{sp}, in addition to providing more insight on heat transfer involving low-pressure steam, therefore aiding in the design so that the desired steam's superheating is achieved.

3 Working principle, subsystems and specifications

The resistojet is placed in the satellite, as presented in figure 3.1. Energy stored in the batteries $E_{batteries}$ is consumed by the different wires at a rate P_{wires} in the device. Part of the heat is transferred to the flowing propellant, but also heat q_{lost} is lost through the control volume boundaries (the subsystems' surfaces exposed to outer space or the interior of the satellite). Heated mass-flow $\dot{m}$ leaves the control volume with a velocity v_{exit} that generates the thrust that propels the satellite. As the tank gets discharged, energy in the control volume is lost, corresponding to the decreasing liquid propellant mass.

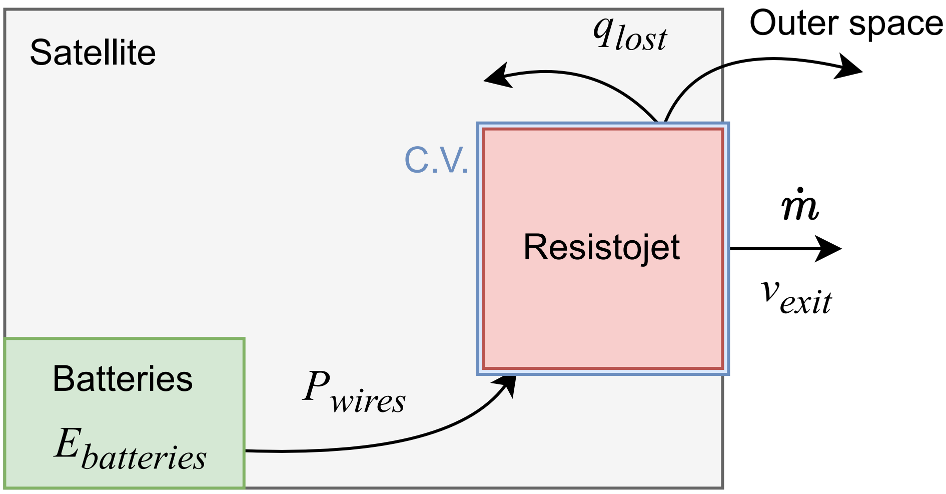

Figure 3.1: Resistojet control volume within the satellite and outer space

The most important parameters for the design are ΔV, which represents the satellite's change in velocity while propelled, specific impulse I_{sp} representing the propulsion's efficiency as described in section 1.1, and thrust. All of these variables are affected by the fluid's exit velocity, according to equations 3.1 to 3.3.

Equation 3.1 is derived from the Tsiolkovsky rocket equation [4], assuming constant exit velocity, with propellant mass m_p and satellite dry mass m_s.

$$\Delta V = v_{exit} \left(ln \left(1 + \frac{m_p}{m_s} \right) \right) \tag{3.1}$$

In equation 3.2, g_0 represents the earth's gravitational acceleration.

$$I_{sp} = v_{exit} g_0 \tag{3.2}$$

Thrust F is the result of multiplying the mass flow $\dot{m}$ and its' exit velocity.

$$F = \dot{m} v_{exit} \tag{3.3}$$

These equations, for simplicity at this stage, assume a fully expanded fluid, with the effect of over or underexpansion taken into account in section 4.2. By expelling a high-velocity fluid, propulsion-related parameters increase, indicating that it is an important variable to study. It is analyzed by looking at specific impulse since it is the result of multiplying the exit velocity by a known constant value.

The energy balance for the device is represented by equation 5.8.8. An optimal device should minimize lost heat for the used power in the wires, while discharging the fluid through the nozzle at low enthalpy and high velocity, to generate as much thrust as possible in an efficient manner.

$$P_{wires} - q_{lost} - \dot{m}\left(h_{exit} + \frac{v_{exit}^2}{2}\right) = \frac{dU_{CV}}{dt} \tag{3.4}$$

At steady state, terms with mass flow are present, and internal energy change is due to the tank being emptied.

When starting the propulsion system mass flow is 0, but wire power is consumed raising the temperature (and internal energy) of the components. Considering the batteries' capacity is limited, focus should also be on minimizing startup energy.

Section 3.1 describes the subsystems' tasks and how they interact with each other.

3.1 Subsystems

As figure 3.1.1 describes, the ResistoJet is divided into 4 main subsystems:

1. Tank
2. Evaporator
3. Superheater
4. Nozzle

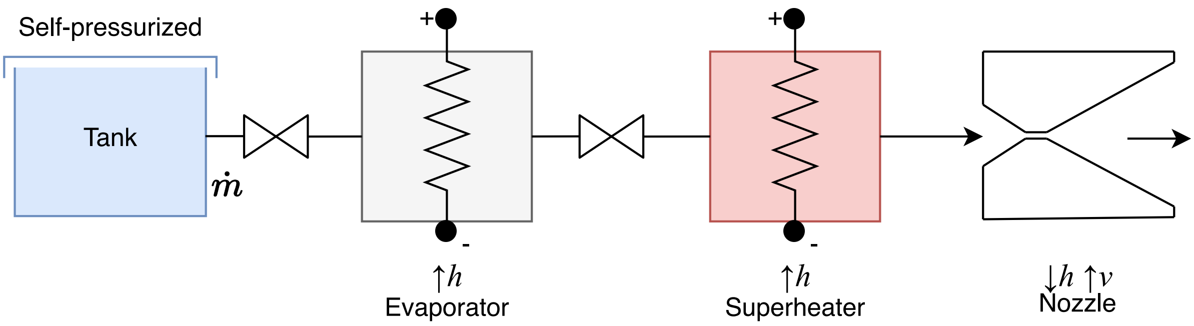

Figure 3.1.1: Typical resistojet layout

The subsystems are described following the propellant flow, starting with the tank and finishing with the nozzle.

3.1.1 Tank

The tank must store enough propellant to achieve the change in velocity (ΔV) necessary for the satellite, determined by the mission requirements. Equation 3.1.1 shows required propellant mass for a mission-specified ΔV.

$$m_p = m_s \left(e^{\frac{\Delta V}{I_{sp} g_0}} - 1 \right) \tag{3.1.1}$$

Propellant mass m_p depends on the propulsion systems' specific impulse I_{sp}, indicating that by maximizing specific impulse for a specified ΔV, propellant mass is minimized. Satellite dry mass m_s also affects the propellant mass. Satellite dry mass is approximately 1.33Kg per CubeSat unit and g_0 represents the earth's gravitational acceleration, having a fixed value of $9.81 \frac{m}{s^2}$. Decreasing propulsion system mass can also decrease the propellant mass needed, but it has a lower impact than maximizing specific impulse, as the propulsion system including the tank only occupies 1 unit out of 6, 12, or more units of the CubeSat. The use of g_0 results from the calculation of I_{sp}, described in section 4.2.

As mentioned in section 2, tank pressure is determined by the tank's temperature and liquid-vapor equilibrium of water. Decreasing the fluid's temperature can have significant effects on several parameters of the device:

- It results in less power consumption in the tank's electrical resistor, as the tank radiates heat to the interior of the satellite.
- Less energy is used heating the propellant mass to be used in an impulse event.
- Equilibrium pressure increases with temperature, requiring increased tank thickness to withstand the internal pressure. A thinner tank occupies less space and decreases the weight as well as startup energy of the system.

At the same time, the tank pressure needs to be high enough to compensate for the propellant's circuit pressure drop up to the nozzle inlet. In this scenario, startup energy associated with heating the entirety of the liquid propellant mass to its operating point can decrease the impulse event time significantly. An auxiliary tank can be utilized, heating only the propellant to be used in one impulse event. That way, the battery capacity can be used more efficiently, allowing for longer impulse events.

3.1.2 Evaporator

The evaporator receives liquid propellant coming from the tank and changes its state from liquid to vapor. Evaporation is achieved through contact with a high-temperature solid, and during this process, the propellant does not change its temperature. This is particularly interesting as the evaporator subsystem can be used as a constant temperature heat sink.

The energy needed for evaporation comes from two sources: an electrical resistor and heat losses from the vapor's heating. An efficient design ensures that the heat losses fall short and never evaporate the total of the needed mass flow, giving room for the resistor to be used as a process's control variable and ensuring stable operation.

3.1.3 Superheater

This subsystem raises the gaseous propellant's enthalpy and prepares it to discharge through the nozzle. It must accommodate a resistor that heats a solid component with ducts where the fluid raises its temperature.

Since the heating wire dissipates heat, its' temperature is the maximum temperature of the system. Therefore, the maximum fluid's temperature will never exceed the heating wire's melting point. The wire's length and diameters must be selected so that at its operation limit temperature, it dissipates enough power to heat the fluid and to account for thermal losses while working at voltages and currents according to the satellite's energy bus restrictions.

Ideally, the wire heats the propellant directly, but absorption of steam is negligible at low pressures and short distances [6]. Therefore, the solid component with ducts is also at a high temperature, as it needs to raise the temperature of the fluid. Due to the solid's high temperature, the startup energy of the system is high, with heat lost through components in contact with the solid or through radiation to other parts of the propulsion system. Minimizing heat losses and startup energy increases the system's efficiencies and extends the duration of the impulse event.

Maximizing thermal resistances minimizes heat losses between the superheater and other components to achieve high-temperature gradients in small volumes with low heat flux. Calculation of thermal resistances takes into account the components' materials as well as their heat exchange area. Usage of materials with low thermal conductivity and high reflectivity (or low emissivity) is required. In addition, low superheater volumes allow small heat exchange areas while still accommodating the heating wire and the fluid ducts.

3.1.4 Nozzle

A convergent-divergent nozzle converts the enthalpy gained by the fluid in the superheater into kinetic energy, resulting in impulse. The higher the enthalpy of the propellant at the nozzle's inlet, the higher the fluid velocity at the nozzle's exit, thus, increasing the devices' ΔV, thrust, and specific impulse.

Since the device is in outer space the backpressure is zero. The nozzle is choked with the fluid unable to reach full expansion. The nozzle must be long enough to accelerate the fluid, but an excessively long nozzle would increase heat losses through radiation to space, decrease the fluid's pressure and temperature and cause condensation or deposition, or exceed the allowed extra volume outside the cubic CubeSat structure [7]. On the other hand, a short nozzle fails to accelerate the fluid and results in specific impulse loss, with more propellant required to achieve the required ΔV.

As both nozzle dimensions and inlet conditions determine the mass flow, the nozzle is designed along with the superheater to reach adequate specific impulse and efficiencies while complying with the energy bus and overall system restrictions.

3.2 Specifications

Once the propulsion system is separated in subsystems, its important parameters are identified and specifications that would ensure good performance of the device are set.

Without the use of stored energy in the batteries, the device would be no more than a cold-gas propulsion system. Both power and energy used to heat the propellant are critical aspects for the device as it determines the minimum battery capacity needed on board and the system's propulsion per battery cycle. While power usage needs to be lower than the batteries maximum deliverable power, a smaller start up energy results in more energy available for actual propulsion in each battery cycle, therefore, design should aim for the smallest amount of energy to reach steady state. These goals are achieved by reducing heat-losses, and the system's overall heat capacity (mass times specific heat capacity) or operation temperatures. Because the propulsion's efficiency is reflected in I_{sp}, having a low maximum working temperature is not an option, and clever design should isolate high temperature components from the rest of the system. The design's mass should also be kept to the minimum to decrease the launching costs of the satellite, the propellant mass needed, and the system's volume.

Also, the propulsion's system volume is kept limited, allowing the satellite to carry the batteries and the payload, among other necessary systems for its successful operation.

Resistojets as the COMET water-based propulsion system developed by Bradford Space or the Steam TunaCan Thruster developed by SteamJet Space Systems are products that fit the restrictions of the project as they use superheated steam to propel CubeSats [8, 9].

Specific impulse from the analyzed competitors are below 185s. A 200s specific impulse target is set for the design to improve the designs already available. 200s of specific impulse require steam superheating up to at least 900K considering an ideal nozzle, therefore the superheater's temperature needs to be above 900K. However, higher fluid temperatures are required to account for different specific impulse losses, explained in section 5.

Minimum tank temperature is chosen to be 278K, as CubeSats have an average interior temperature of 273 to 283K [10], and microsatellites temperatures range between 283K and 303K [11]. If a tank temperature higher than 303K is required, heating with a resistor is necessary.

No ΔV requirements are imposed, as ΔV depends on each mission and can be adjusted easily regulating the propellant mass to be carried, as it is observed in subsection 3.1.1.

GOMspace supplies batteries for a capacity of 80Wh, and power requirements of up to 74W, with its specifications in table 3.2.1 [12].

Configuration	Number of cells	Capacity [Wh]	V_{range} [V]	$V_{nominel}$ [V]	Capacity [Ah]
2S-4P	8	77	6 - 8.4	7.4 V	10.4
4S-2P	8	77	12 - 16.8	14.8 V	5.2
8S-1P	8	77	24 - 33.6	29.6 V	2.6

Table 3.2.1: GOMspace Battery datasheet

AAC Clyde Space provides data for its OPTIMUS batteries capacity, voltage and size, displayed in table 3.2.2, showing a maximum capacity of 80Wh and output power of 40W [13].

Technical Specifications

General

Material	Lithium Polymer
Vacuum	10-5 torr
Operating Temperature	-10°C to +50°C
Storage Temperature	Recommended: -10°C to +10°C 1 Year: -20°C to +20°C 3 Months: -20°C to +45°C 1 Month: -20°C to +60°C
Vibration	To [RD-2]

OPTIMUS Range

Model	OPTIMUS-30	OPTIMUS-40	OPTIMUS-80
Capacity	30 Wh	40 Wh	80 Wh
Mass (typical)	268 g	335 g	670 g
Length	95.89 mm	95.89 mm	95.89 mm
Width	90.17 mm	90.17 mm	90.17 mm
Height*	21.55 mm	27.35 mm	56.94 mm
Charge/Discharge Current	1.95 A	2.6 A	5.2 A

*Height from top PCB to lowest component

General Electrical Characteristics

EoC Voltage	8.26 V (typical)
Full Discharge Voltage	6.2 V (typical)
Charge Voltage Limit	8.4 V (max)
Discharge Voltage Limit	6.2 V (min)
Charge/Discharge Current Rate	1.53 (fraction of capacity)
Quiescent Power Consumption	< 0.1 W (30 Wh & 40 Wh) < 0.2 W (80 Wh)
Interfaces	Standard CubeSat PC104
Power Buses	3V3 and 5V
Serial Ports	I2C

Table 3.2.2: AAC Clyde Space OPTIMUS Battery datasheet

Table 3.2.3 shows specifications of an AAC Clyde Space STARBUCK-NANO CubeSat power conditioning and distribution unit, with a limiting voltage of 12V [14].

The requirements shown in table 3.2.4 are a result of the analysis of market available water ResistoJets, and related systems such as batteries or energy buses. Maximum voltage of 6V and current of 10.4A are selected, enabling selection of either GOMspace 2S-4P or AAC Clyde Space OPTIMUS-80 batteries.

Technical Specifications

General

Design Life	5 years in LEO
Regulated Power Buses	3.3V, 5V, and 12V
Latching Current Limit (LCL)	10 Configurable
Interfaces	I2C
Max. Battery Voltage	8.2V
Operating Temperature	-40°C to 85°C
Storage Temperature	-50°C to 100°C
Vacuum	10^{-5} torr
Radiation Tolerance	10 KRad
Vibration	To [RD-3]

Product Information

Product	Nano-Pico	Nano	Nano-Plus
Integrated Battery	Yes 10 or 20Wh	No	No
Intended Use	1U CubeSat	2U and 3U CubeSat with body panels	3- 12U CubeSat with deployable panels
Mass (typical)	86 g	86 g	148 g
Length	95.89 mm	95.89 mm	95.89 mm
Width	90.17 mm	90.17 mm	90.17 mm
Height*	16.2 mm	16.2 mm	20.82 mm

** Height from top PCB to lowest component*

Table 3.2.3: AAC Clyde Space Power STARBUCK-NANO conditioning and distribution unit datasheet

Parameter	**Value**
I_{sp}	>200s
T_{tank}	278-303K
$P_{propulsion}$	<50W
$E_{battery}$	77Wh
Volume (without tank)	<0.5U
Satellite total units	6U
Voltage	6 V
Current	10.4 A

Table 3.2.4: Requirements for the propulsion system

4 Design process and calculations

Proper design of the propulsion system requires the calculation of both solid temperatures and fluid temperatures. Both have to be connected during the design process, as heat is transferred between the heating wires (directly or through another component) and the fluid. In addition, the resistors have limitations set by the CubeSat's power bus, but power consumption also affects temperatures in the device.

With the different subsystems of the resistojet described in section 3.1, it is clear that they are interconnected in a very complex manner, with trade-offs that involve all parts of the propulsion system. To account for all of the interactions between these subsystems, a simulation logic is explained in figure 4.1 that allows for a calculation for a proposed design of the characteristics such as specific impulse, thrust, or various efficiencies. Iteration and analysis of the process results can lead to a viable design. Sections 4.1 to 4.5 provide in-depth explanation of the calculations performed by every subprocess, in blue in figure 4.1. Section 4.6 describes how the calculation process starts, how subprocesses interact with each other, and how model convergence is ensured. Inputs are shown in gray to the left, outputs in red, with checks to comply with satellite or model restrictions in yellow. Inputs, outputs, and checks are clarified in each of the subprocesses subsections.

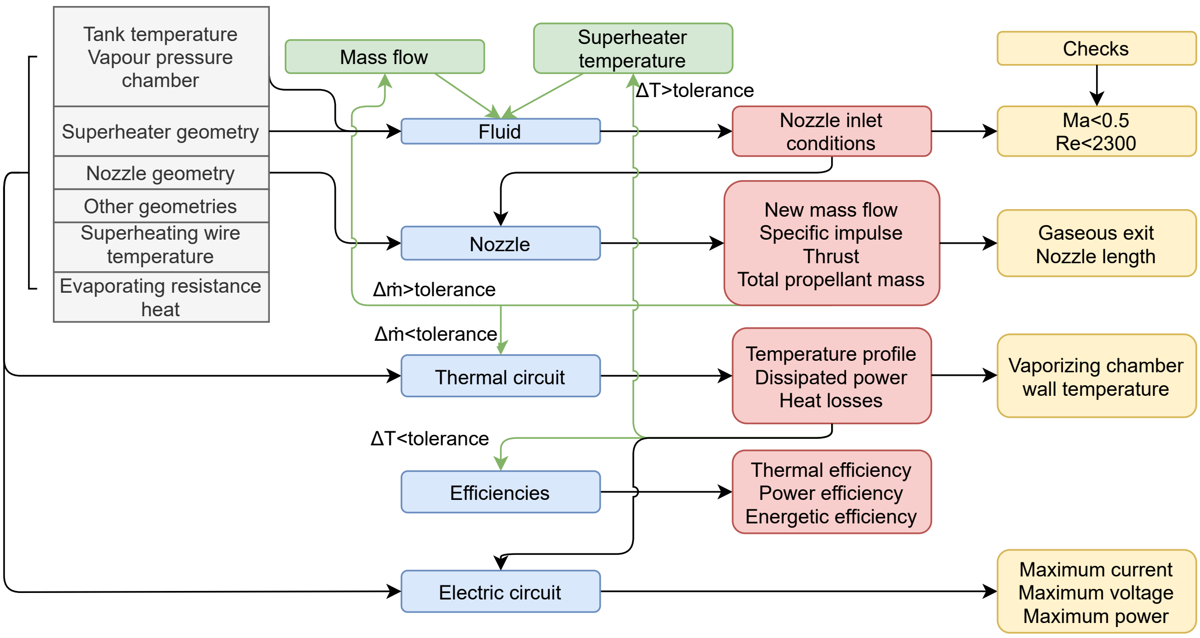

Figure 4.1: Simulation logic

4.1 Fluid simulation

In addition to the duct geometries selected, inputs to this model include the tank's temperature, the system's mass flow, and a wall temperature T_s representing the solid that exchanges heat with the fluid.

The simulation is subdivided into two processes:

- Local losses: model used to calculate pressure drop in local losses such as diameter changes or sudden contractions
- Heat transfer: model used to simulate heat transfer between the solid and a stretch of duct

4.1.1 Local losses

Local losses are calculated as described in [15]. The process is assumed adiabatic, considering that across the process the fluid does not exchange heat with the environment. Figure 4.1.1 depicts an example of the process.

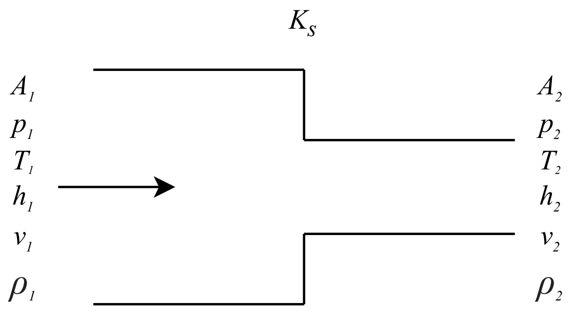

Figure 4.1.1: Local loss process

A mass flow with known properties goes through a sudden contraction and the exit properties are unknown. The unknown exit properties are 5: temperature T, pressure p, velocity v, enthalpy h and density ρ, calculated with the help of the XSteam function, according to the following 5 equations:

- Total enthalpy conservation due to it being an adiabatic process

$$h_1 + \frac{{v_1}^2}{2} = h_2 + \frac{{v_2}^2}{2} \tag{4.1.1}$$

- Static loss coefficient equation: K_s is determined by the geometry that causes the pressure loss

$$K_s = \frac{2\left(p_2 - p_1\right)}{\rho_2 {v_2}^2} \tag{4.1.2}$$

- Continuity equation

$$\dot{m} = \rho_1 v_1 A_1 = \rho_2 v_2 A_2 \tag{4.1.3}$$

- Density as a function of pressure and temperature for water vapor

$$\rho = f\left(p, T\right) \tag{4.1.4}$$

- Specific enthalpy as a function of pressure and temperature for water vapor

$$h = f\left(p, T\right) \tag{4.1.5}$$

4.1.2 Heating

Mass flow, temperature, and pressure serve as the input for a 1-D Rayleigh-Fanno flow model used to simulate heat exchange between the solid superheater and the propellant, with pressure loss due to friction [16]. The superheater's duct is discretized in its axial direction and according to the superheater's inlet conditions Mach number (which can be obtained by dividing the gas speed and the speed of sound, obtainable via XSteam), temperature and pressure are calculated for the next node. Equation 4.1.6 is solved by using a 4$^{\text{th}}$ order Runge-Kutta method and Mach number is obtained. Ma represents the fluid's Mach number, γ represents the specific heat ratio for the fluid (obtained via XSteam for each temperature and pressure), f is the friction factor, D_h is the duct's hydraulic diameter, A is the duct's cross-section and $\frac{dT_o}{dx}$ represents the spatial derivative of the total temperature.

$$\frac{dMa}{dx} = \frac{Ma\left(1+\frac{\gamma+1}{2}Ma^2\right)}{1-Ma^2}\left(\gamma Ma^2\frac{f}{D_h} + \frac{(1+\gamma Ma^2)}{2T_0}\frac{dT_0}{dx} - \frac{\gamma Ma^2}{A}\frac{dA}{dx}\right) \tag{4.1.6}$$

The total temperature derivative for node i is calculated according to the energy equation 4.1.7. q_i represents the heat exchanged (in $\frac{W}{m^2}$), D_i is the duct's diameter, $\dot{m}$ represents the mass flow and C_{p_i} is the fluid's constant pressure specific heat.

$$\frac{dT_{0_i}}{dx} \approx \frac{\Delta T_{0_i}}{\Delta x} = \frac{q_i \pi D}{\dot{m} C_{p_i}} \tag{4.1.7}$$

As inside the duct the governing heat exchange mechanism is forced convection, heat exchanged q_i can be calculated according to equation 4.1.8. T_{s_i} represents the solid temperature for node i, and h_{c_i} is the forced convection coefficient for node i.

$$q_i = h_{c_i}\left(T_{s_i} - T_{0_i}\right) \tag{4.1.8}$$

With the temperature derivative from equation 4.1.7, the total temperature for node *i+1* can be calculated according to equation 4.1.9.

$$T_{0_{i+1}} = T_{0_i} + \Delta T_{0_i} \tag{4.1.9}$$

Finally static temperatures and pressures are calculated according to equations 4.1.10 and 4.1.11.

$$\frac{T(x)}{T(0)} = \frac{T_0(x)}{T_0(0)}\frac{1+\frac{\gamma-1}{2}\left(Ma(0)\right)^2}{1+\frac{\gamma-1}{2}\left(Ma(x)\right)^2} \tag{4.1.10}$$

$$\frac{p(x)}{p(0)} = \frac{A(0)}{A(x)}\frac{Ma(0)}{Ma(x)}\sqrt{\frac{T(x)}{T(0)}} \tag{4.1.11}$$

Due to power limitations and a high temperature needed at the nozzle's inlet, mass flow is low and therefore laminar even for very small duct diameters. For laminar flows, Nusselt number Nu_D and friction factor f are determined by equations 4.1.12 and 4.1.13 [6]. Both equations only apply when the fluid's Reynolds number Re is less than 2300 and when the Mach number is less than 0.5. Terms related to the fluid's bulk total temperature T_0 and solid temperature T_s are applied due to the high temperature difference between the fluid's inlet and outlet as recommended in [6]. i subindexes denote usage of temperatures and pressures at node i for the calculation of fluid's properties such as the thermal conductivity k.

$$Nu_{D_i} = \frac{h_{c_i} D}{k_i} = 3.657 \left(\frac{T_{0_i}}{T_{s_i}} \right)^{0.25} \tag{4.1.12}$$

$$f_i = \frac{64}{Re_i} \left(\frac{T_{s_i}}{T_{0_i}} \right)^{0.14} \tag{4.1.13}$$

Equation 4.1.6 involves fluid total temperature's derivative with respect to the local position in the duct, which as shown in equation 4.1.7 depends on the fluid's constant pressure specific heat, considered constant at each node. Since the temperature on the following node is calculated with the temperature derivative and therefore C_p, a mesh convergence condition is presented to ensure that the constant C_p hypothesis is valid.

Energy conservation is denoted by equation 4.1.14 in its integral form for a tube of length L. Total temperature is also described in terms of enthalpy and speed.

$$\int_0^L q\pi D dx = \int_{T_{0_{(x=0)}}}^{T_{0_{(x=L)}}} \dot{m} C_p dT_0 \tag{4.1.14}$$

If the total temperature is also described in terms of enthalpy and speed, the energy conservation equation can be written as equation 4.1.15. The right-hand side of equation 4.1.15 is given by the inlet and outlet total temperatures given by the model. Kinetic energy is not included, since total temperatures are used.

$$q_{Integral} = \dot{m} \left(h \left(T_{0_{(x=L)}} \right) - h \left(T_{0_{(x=0)}} \right) \right) \tag{4.1.15}$$

Heat per unit area exchanged by the fluid between two nodes q_i is calculated with the fluid convection correlations. When multiplied by the heat exchange area, the total exchanged heat in the duct from nodes *1* to n is obtained as shown in equation 4.1.16.

$$q_{Discrete} = \sum_{i=1}^{n-1} q_i \pi D \tag{4.1.16}$$

To check that mesh refinement is adequate, the heat sum must not vary greatly from the power calculation with enthalpies and velocities. Therefore, error equation 4.1.17 to check convergence is presented. In this analysis, ϵ is kept below 1%.

$$\left| \frac{q_{Integral} - q_{Discrete}}{q_{Integral}} \right| < \epsilon \tag{4.1.17}$$

4.2 Nozzle simulation

The nozzle simulation receives as inputs a mass flow and total properties at the inlet of the nozzle. According to the predefined nozzle geometry, calculations for thrust and specific impulse are performed.

To simplify calculations, several hypothesis are made:

- Isentropic nozzle, with no friction or heat losses
- Steam as an ideal gas, with calculation of the specific heat ratio according to section 4.2.1
- Efficiency considerations are applied only to specific impulse and thrust
- Pressure in outer space is considered zero.

Isentropic nozzle's equations for ideal gases are presented (4.2.1 to 4.2.3), obtaining temperature, pressure and density as a function of the Mach number Ma, the inlet temperature, pressure and density (T, p and ρ respectively, denoted with a 0 subscript), and the specific heat ratio for the fluid γ [17].

$$\left(\frac{T_0}{T}\right) = 1 + \frac{\gamma - 1}{2} Ma^2 \tag{4.2.1}$$

$$\left(\frac{p_0}{p}\right) = \left(1 + \frac{\gamma - 1}{2} Ma^2\right)^{\left(\frac{\gamma}{\gamma-1}\right)} \tag{4.2.2}$$

$$\left(\frac{\rho_0}{\rho}\right) = \left(1 + \frac{\gamma - 1}{2} Ma^2\right)^{\left(\frac{1}{\gamma-1}\right)} \tag{4.2.3}$$

As mentioned in section 3.1.4 dimensions of the nozzle's throat, more specifically its area, determine flow in the superheater. As the backpressure is 0, the pressure ratio of the nozzle is higher than the critical pressure ratio for any inlet pressure, resulting in a choked flow.

It is convenient to calculate the nozzle's thrust by separating it into two parameters: the nozzle's characteristic velocity c^* and its thrust coefficient C_f [18], represented in equations 4.2.4 and 4.2.5. c^* represents the potential of the propellant to create thrust and depends almost exclusively on the thermodynamic characteristics of the propellant. C_f represents how the nozzle can convert the propellant's enthalpy into kinetic energy and generate thrust, depending almost exclusively on the nozzle's geometry.

The left-hand side (LHS) of equation 4.2.4 takes into account the nozzle's inlet total pressure p_t, choke area A^* and mass flow $\dot{m}$, while calculation of the right-hand side (RHS) involves the ideal gas constant for water vapor R, the nozzle's inlet total temperature T_t and the ratio of specific heats γ.

$$c^* = \frac{p_t A^*}{\dot{m}} = \sqrt{\frac{RT_t}{\gamma}} \left(\frac{\gamma + 1}{2}\right)^{\frac{\gamma+1}{2(\gamma-1)}} \tag{4.2.4}$$

As mentioned in section 3.1.4, dimensions of the nozzle's throat, more specifically its area, determine flow in the superheater. Since the mass flow used to calculate c^* with the LHS of the equation (c^*_{LHS}) is an input to the nozzle model, a verification must be performed by calculating the RHS of the equation (c^*_{RHS}). If differences between both sides of the equations are found, a new mass flow is calculated. Another fluid heating simulation is performed to determine the new total temperature and pressure at the inlet. The new mass flow calculation is explained in depth in section 4.6. The nozzle simulation results are only valid when both sides of equation **??** are equal.

Thrust coefficient calculation involves the Mach number at the exit of the nozzle Ma_e and γ, but the dependence of C_f and γ is not strong and is set when choosing water vapor as the propellant. Ma_e is directly correlated with the nozzle's exit area, which is selected to ensure the exit of the propellant in gaseous state avoiding condensation[19] or deposition[20] by using equations 4.2.1 and 4.2.2 and taking into account CubeSat restrictions for extra volume outside the satellite's structure.

$$C_f = \frac{\left(\frac{\gamma+1}{2}\right)^{\frac{\gamma+1}{-2(\gamma-1)}}}{Ma_e\sqrt{1+\frac{\gamma-1}{2}Ma_e^2}}\left(\gamma Ma_e^2+1\right) \tag{4.2.5}$$

The characteristic velocity and thrust coefficient allow for the calculation of effective exhaust velocity C (equation 4.2.6), I_{sp} (equation 4.2.7) and F (equation 4.2.8). Note that these variables were already defined in section 3, but in this case, the fluid can be under or overexpanded. Effective exhaust velocity is not the actual exhaust velocity, but it also includes the term associated with pressure at the exit of the nozzle. C can turn into the exhaust velocity v_{exit} mentioned previously if the fluid is at full expansion when exiting the nozzle, in this case with Ma_e tending to infinity (backpressure in space is zero).

$$C = C_f c^* \tag{4.2.6}$$

$$I_{sp} = \frac{C}{g_0} \tag{4.2.7}$$

$$F = \dot{m}C \tag{4.2.8}$$

If a specific impulse efficiency for the nozzle $\eta_{I_{sp}}$ and thrust efficiency η_F is added to the model, real specific impulse and thrust can be calculated (equations 4.2.9 and 4.2.10).

$$I_{sp_{real}} = \eta_{I_{sp}} I_{sp} \tag{4.2.9}$$

$$F_{real} = \eta_F F \tag{4.2.10}$$

A real specific impulse is obtained, that is constant for every stage of propulsion (if more than 1 is needed). Since I_{sp} is constant, propellant mass can be calculated according to equation 3.1.1.

4.2.1 Ratio of specific heats

As it is observed, the ratio of specific heats γ is involved in equations 4.2.1 to 4.2.5. The MATLAB function XSteam [19] provides both constant pressure and volume specific heats C_p and C_v, and γ is defined according to equation 4.2.11.

$$\gamma = \frac{C_p}{C_v} \tag{4.2.11}$$

To establish a γ to be used in the previously mentioned nozzle equations, the nozzle inlet conditions are useful to calculate the fluid's entropy. Since the nozzle is assumed to be isentropic, C_p and C_v can be obtained from the XSteam function for a range of temperatures while maintaining a constant entropy and γ can be calculated. The range of temperatures has the nozzle's inlet temperature as the upper boundary and the lower temperature is determined by the range of validity of equations provided by XSteam. Finally, the γ to be used results from an average of the obtained specific heat ratios for different temperatures.

Figure 4.2.1 shows possible values for γ, ranging from 1.21 to 1.27.

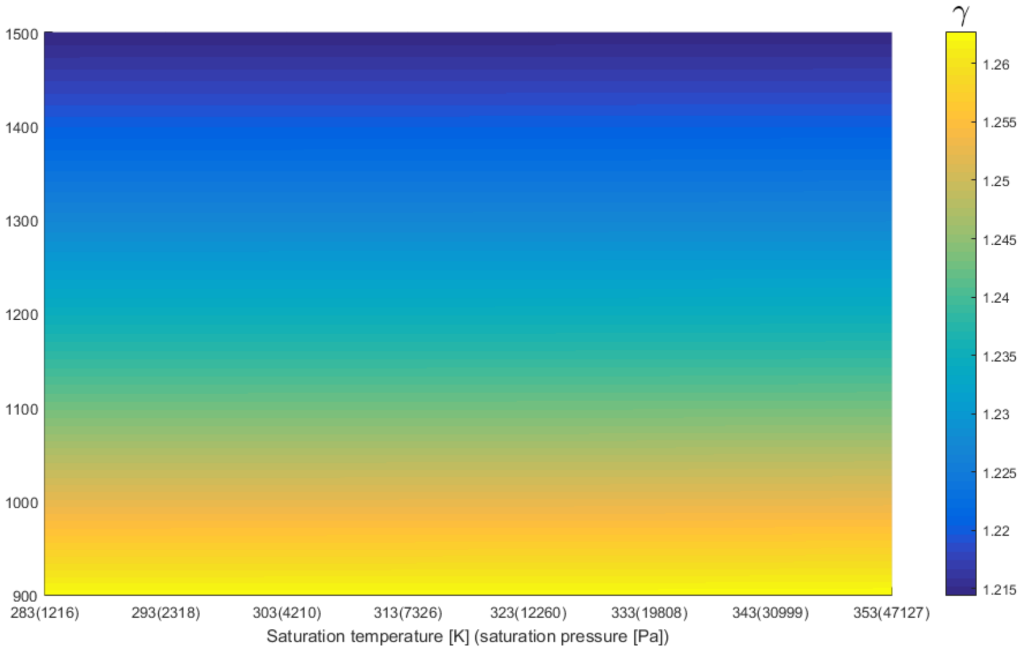

Figure 4.2.1: Ratio of specific heat for possible nozzle inlet conditions

4.3 Thermal circuit

The thermal circuit can calculate temperatures for the components in both idle and active operation, as well as heat losses during operation. Inputs for this model are the heating wire's temperature and heat taken by the fluid during evaporation and superheating.

A steady-state model with 1-D resistances is proposed to accelerate the design process, as it is solved much faster than a 2-D or 3-D finite element analysis. However, a more complex model and experimental testing are needed for validation. A general overview of the utilized method is presented in this section, with the final thermal circuit to be used explained in section 5.8.3 with it's hypotheses and boundary conditions.

Nodes j and k are connected by the thermal resistance R_i, as it is shown in equations 4.3.1 and 4.3.6. q_j represents the heat flux entering in node j.

$$\frac{T_j - T_k}{R_i} = q_j \tag{4.3.1}$$

$$\frac{T_k - T_j}{R_i} = q_k \tag{4.3.2}$$

Thermal resistances are split in three categories:

- Rectangular coordinates: Calculated according to equation 4.3.3, where k is the material's conductivity, L is the material's length and A is the material's cross section area.

$$R_{axial} = \frac{L}{kA} \tag{4.3.3}$$

- Cylindrical coordinates: Calculated according to equation 4.3.4. d_o is the cylinder's outer diameter, d_i is the inner diameter and L represents its length.

$$R_{radial} = \frac{ln\frac{d_o}{d_i}}{2\pi Lk} \tag{4.3.4}$$

- Radiation: Iterative process to solve a linear system of equations. For iteration n, temperatures calculated in iteration $n-1$ are used for resistance calculation. Convergence is met when the difference between the calculated temperatures and the previous step results are below $10^{-3}K$. σ represents the Stefan-Boltzmann constant, ϵ represents the material's emissivity, and F_{jk} represents the view factor between surfaces A_j and A_k.

$$\begin{gathered} q_{k_n} = F_{j-k} A_j \epsilon \sigma (T_j^4 - T_k^4) \\ q_{k_n} = \frac{(T_{j_n} - T_{k_n})}{R_{RAD\ i_n}} \\ (T_j^4 - T_k^4) = (T_j^2 + T_k^2)(T_j^2 - T_k^2) = (T_j^2 + T_k^2)(T_j + T_k)(T_j - T_k) \\ \frac{1}{R_{RAD\ i_n}} = F_{j-k} A_j \epsilon \sigma (T_{j_{n-1}}^2 + T_{k_{n-1}}^2)(T_{j_{n-1}} + T_{k_{n-1}}) \end{gathered} \tag{4.3.5}$$

Equations for nodes j and k can be put together to form an individual resistance matrix $[k]_i$ as it is shown in equation 4.3.6.

$$\begin{gathered} [\mathbf{k}]_i \{\mathbf{T}\}_i = \{\mathbf{q}\}_i \\ \begin{bmatrix} \frac{1}{R_i} & -\frac{1}{R_i} \\ -\frac{1}{R_i} & \frac{1}{R_i} \end{bmatrix} \begin{Bmatrix} T_j \\ T_k \end{Bmatrix} = \begin{Bmatrix} q_j \\ q_k \end{Bmatrix} \end{gathered} \tag{4.3.6}$$

The individual matrix for each resistance $[\mathbf{k}]_i$ can be added to a global matrix $[\mathbf{K}]$ that connects every resistance in the system [21]. Note that [21] performs the assembly for structural elements, but the assembly method can still be applied for thermal resistances. Finally, equation 4.3.7 determines the relation between the geometry, the heat fluxes, and temperatures of the design.

$$[\mathbf{K}]\{\mathbf{T}\} = \{\mathbf{q}\} \tag{4.3.7}$$

The boundary conditions for the model involve both heat fluxes and temperatures:

- Heat fluxes
  - Evaporation
  - Superheating
- Temperatures
  - Outer space
  - Satellite's interior
  - Wire

As the geometry of the components is already defined, the resistance matrix $[\mathbf{K}]$ is defined. Therefore, for a specific node, both heat flux and temperature can't be prescribed. This would result in an unsolvable system: likely, the equation will not be fulfilled if all of the equation's variables are fixed. Since heat flux leaving the superheater comes from the fluid model, its' temperature cannot be prescribed and the temperature and heat flux that satisfies both models is reached through an iterative process. Other nodes also need to have prescribed heat fluxes or temperatures. Nodes representing heat sinks or sources such as the wire, outer space, or the satellite's interior have their temperature fixed. The rest of the nodes have a heat flux assigned: the heat flux is zero unless it receives or releases heat to the fluid.

Two subsets of nodes are created, separating temperature and flux vectors into four vectors:

- Prescribed temperatures $\{\mathbf{T_c}\}$
- Unknown temperatures $\{\mathbf{T_x}\}$
- Prescribed heat fluxes $\{\mathbf{q_c}\}$
- Unknown heat fluxes $\{\mathbf{q_x}\}$

Equation 4.3.7 can be rearranged into equation 4.3.8.

$$\begin{bmatrix} \mathbf{K_{11}} & \mathbf{K_{12}} \\ \mathbf{K_{21}} & \mathbf{K_{22}} \end{bmatrix} \begin{Bmatrix} \mathbf{T_x} \\ \mathbf{T_c} \end{Bmatrix} = \begin{Bmatrix} \mathbf{q_c} \\ \mathbf{q_x} \end{Bmatrix} \tag{4.3.8}$$

With equations 4.3.9 and 4.3.10 both unknown heat fluxes and temperatures can be obtained.

$$\{\mathbf{T_x}\} = [\mathbf{K_{11}}]^{-1} \left(\{\mathbf{q_c}\} - [\mathbf{K_{12}}]\{\mathbf{T_c}\}\right) \tag{4.3.9}$$

$$\{\mathbf{q_x}\} = [\mathbf{K_{21}}]\{\mathbf{T_x}\} + [\mathbf{K_{22}}]\{\mathbf{T_c}\} \tag{4.3.10}$$

Once temperatures are calculated, a temperature check is performed, as radiative resistances are involved in the model. If equation 4.3.11 is not satisfied, the radiative resistance is recalculated with the newly obtained temperatures for the nodes that it connects, the global resistance matrix is updated and the equation system in 4.3.7 is solved once again.

$$\|T_{calculated} - T_{assumed}\| < 10^{-3} K \tag{4.3.11}$$

4.4 Efficiencies

Efficiencies are calculated taking into account the thermal losses described in chapter 4.3.

Three main efficiencies are calculated in this submodel:

1. Power conversion efficiency (η_{power}):: ratio between gained energy by the mass flow up until the nozzle inlet (enthalpy and kinetic energy) and the used wire power at steady-state. It indicates if heat is actually being gained by the fluid or leaves the system.

2. Energetic efficiency (η_{energy}):: similar to power conversion efficiency, but is calculated as the ratio between energy gained by the fluid in an impulse event, and energy consumed. It differs from power conversion efficiency, as it takes into account the startup energy of the device. Having an energetic efficiency very distant from the power conversion efficiency indicates a costly startup from an energetic standpoint. As startup energy is minimized, their values tend to be similar.

3. Recovery efficiency ($\eta_{recovery}$): calculated as the ratio between heat leaving the superheater (the second hottest component after the wire) that contributes to evaporation, and total heat lost by the superheater. Recovery efficiencies close to 1 indicate that heat is reused almost completely. In general, high $\eta_{recovery}$ is linked with high η_{power}, as most of the heat flowing out of the device is expected to come from the superheater.

Equations for these efficiencies are presented at later sections, once a more defined control volume for the device is presented.

4.5 Electric circuit

Resistors are calculated using equation 4.5.1. This equation relates the electrical resistivity (ρ), length (l) and cross section of the electrical resistances (S).

$$R_{electric} = \frac{\rho l}{S} \tag{4.5.1}$$

With all resistors calculated, a correct electrical model can be used to simulate the electrical circuit involved in the propulsion system. Current and voltage are calculated using equation 4.5.2 and 4.5.3, making sure that the system's maximum current and voltage, and therefore power, is not surpassed. Both current and voltage are calculated according to P_{wire}, which is obtained in the thermal circuit.

$$I_{wire} = \sqrt{\frac{P_{wire}}{R_{electric}}} \tag{4.5.2}$$

$$V_{wire} = I_{wire} R_{electric} \tag{4.5.3}$$

The equation described previously can be used to design the electrical heaters to be used in evaporation, superheating, and any other heater needed based on the power budget assigned to each one.

4.6 Iteration process

Having described the calculation subprocesses, the complete iteration can be explained.

As shown in figure 4.1, geometries, tank temperature, vapor pressure, superheating wire temperature, and the evaporating resistor heat are used as input for the model. To start the iteration, a seed mass flow and seed superheater temperature need to be proposed, as they are required to run the fluid submodel. The fluid submodel outputs the nozzle inlet conditions for the flow and nozzle calculations are performed. Equation 4.2.4 has total pressure at the nozzle inlet on the left-hand side of the equation, while the total temperature is on the right side, but both come from the same subprocess. Since the geometry for the nozzle is selected previous to the process and remains unchanged during the whole iteration, changes in the mass flow will lead to changes in pressure and temperature at the nozzle inlet. Finally mass flow is determined when equation 4.2.4 is satisfied.

If equation 4.2.4 is solved for mass flow, equation 4.6.1 is obtained.

$$\dot{m} = \frac{p_t A^*}{\sqrt{\frac{RT_t}{\gamma}} \left(\frac{\gamma+1}{2}\right)^{\frac{\gamma+1}{2(\gamma-1)}}} \tag{4.6.1}$$

Revisiting equations in section 4.1, the final total temperature decreases with an increase in the mass-flow because of the increase in needed energy to heat the fluid and the constant convection coefficient assumed.

According to the temperature obtained from the fluid sub-model, two scenarios can be distinguished:

- Mass flow needs to be reduced, as the temperature is low.
- Mass flow needs to be increased, as the temperature is high.

A new mass flow for the iteration $k+1$ can be calculated according to equation 4.6.1 with the total temperature and pressure at the inlet of the nozzle, but for the obtained with the previously proposed mass flow (iteration k). If equation 4.6.1 is rearranged equation 4.6.2 is obtained.

$$\dot{m}_{new} = \dot{m}_k \frac{c^*{}_{LHS}}{c^*{}_{RHS}} \tag{4.6.2}$$

Calculation of the new mass flow with equation 4.6.2 can lead to very slow convergence or even divergence, therefore a user-selected relaxation factor β_1 between 0 and 1 is introduced. If β_1 is too small, divergence can occur, but a high value of β_1 can lead to slow convergence.

$$\begin{gathered}\dot{m}_{k+1} = \beta_1 \dot{m}_k + (1-\beta_1)\,\dot{m}_{new} \\ \dot{m}_{k+1} = \dot{m}_k \left(\beta_1 + (1-\beta_1)\,\frac{c^*{}_{LHS}}{c^*{}_{RHS}}\right)\end{gathered} \tag{4.6.3}$$

Fluid and nozzle simulations are performed recalculating the mass flow until convergence is reached, determined by equation 4.6.4, with K_f being a user-defined tolerance. The value of K_f

is assigned keeping into account that it represents the difference between the ratio of both sides of the characteristic velocity equation and 1 (ideal).

$$\left| \frac{c^*{}_{LHS}}{c^*{}_{RHS}} - 1 \right| < K_f \tag{4.6.4}$$

The fluid simulation uses the superheater's temperature as the input and calculates the heat exchanged with the superheater. The thermal circuit uses the exchanged heat as input and calculates the superheater's temperature. As the input temperature for the fluid model and the output from the thermal circuit need to be equal, an iterative process is performed to determine the final temperature.

Starting from a seed superheater's temperature T_{Si}, fluid and nozzle simulations are performed until the mass flow for that proposed superheater temperature is obtained. These models provide the thermal circuit the adequate heat fluxes to serve as input (evaporation and superheating), and by fixing the cable temperature to its' operation limit, a new superheater's temperature $T_{Scircuit}$ can be calculated. This calculated temperature is compared to the temperature proposed at the start and a new superheater temperature T_{Si+1} is obtained, to be used once again in the fluid and nozzle submodels.

The new superheater temperature is calculated according to equation 4.6.5. Due to similar reasons as in equation 4.6.3, a relaxation factor β_2 is applied.

$$T_{Si+1} = \beta_2 T_{Si} + (1 - \beta_2)\, T_{Scircuit} \tag{4.6.5}$$

The iteration process is finished when equation 4.6.6 is satisfied. K_T is a user-defined tolerance for the difference between the assumed and the calculated superheater's temperature.

$$|T_{Si} - T_{Scircuit}| < K_T \tag{4.6.6}$$

5 Thermal analysis

This section describes the engineering decisions for the device from a thermal standpoint analyzing several alternatives, including material selection and their geometries. Preliminary dimensions are defined by using different submodels, to be fine-tuned in section 7 by using the full simulation model present in section 4. Considering that the main goal of the device is generating high-speed fluid, the required temperature of the propellant at the nozzle inlet is first studied so that limit temperatures for other solid components are known and materials or construction methods can be chosen. Then, subsections for all 4 subsystems are present. Finally, a thermal circuit for the design is proposed to be used during fine-tuning and to connect the subsystems with the method described in section 4.

5.1 Required propellant temperature

Required propellant temperature is studied. The propulsion system is based on heating the propellant to generate thrust when it is discharged through the nozzle. Figure 5.1.1 shows how raising the fluid temperature improves the specific impulse of the device.

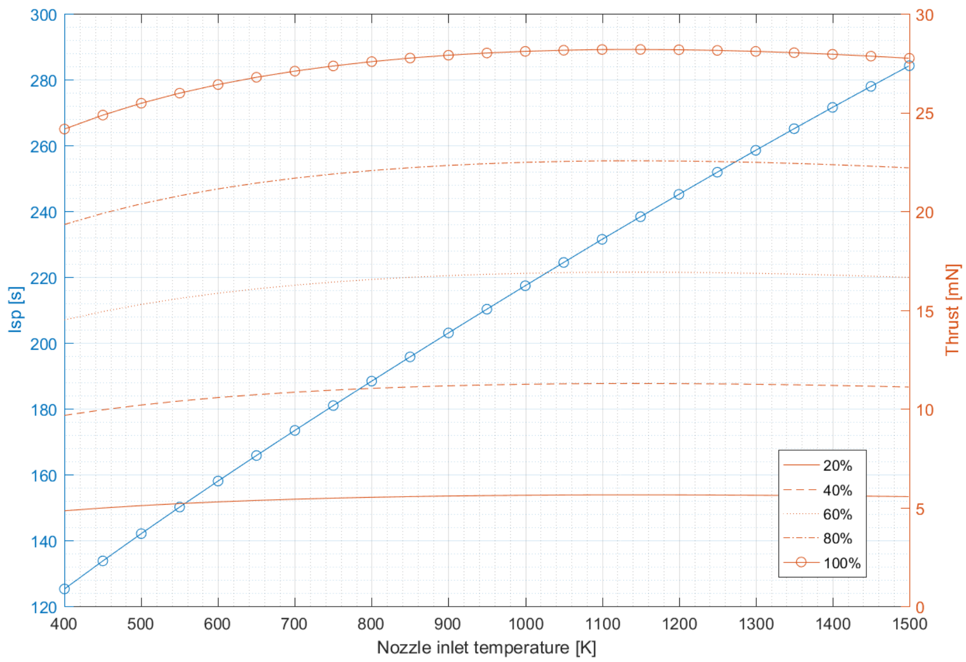

Figure 5.1.1: Specific impulse and thrust for various nozzle inlet temperatures and power conversion efficiencies

900K fluid is needed at the nozzle inlet to reach 200s of specific impulse. If nozzle efficiencies are taken into account, heating must exceed the previously mentioned 900K.

As the power usage for the different points in the plot is constant, thrust also varies, being quasi-constant for the entire temperature range studied. When power conversion efficiency decreases, thrust decreases due to reduced mass flow. While the discharge of a high-temperature fluid increases the system's propulsion efficiency characterized by specific impulses, it must be considered that a solid component has to reach an even higher temperature than the fluid. Therefore, the heating element's temperature is a limiting temperature in the design. Hot components need to be insulated for efficient usage of the very limited energy available in the satellite, diminishing heat losses to the exterior to a minimum. High-temperature superheating requires more insulation to maintain power conversion efficiency, which results in a higher volume and mass for the resistojet. Low-temperature superheating allows for a very compact and light system that carries with it a bigger tank, as is seen in figure 5.1.2 in the decreasing propellant mass needed for higher temperature superheating.

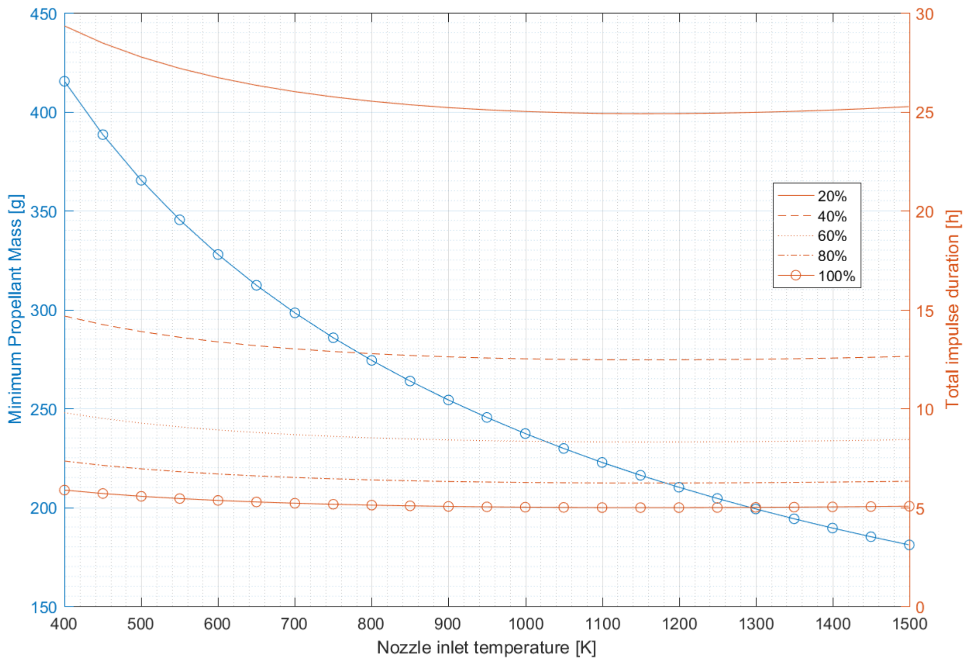

Figure 5.1.2: Propellant mass needed and impulse duration for various nozzle inlet temperatures and power conversion efficiencies

Figure 5.1.2 shows that the propellant mass needed is not affected by the system's power conversion efficiency, but a more efficient use of power and energy results in fewer impulse events and faster deployment of the satellite, observable in figure 5.1.3. Nevertheless, it must be remembered that the available space is a restriction in this propulsion system, it must be limited to 1U.

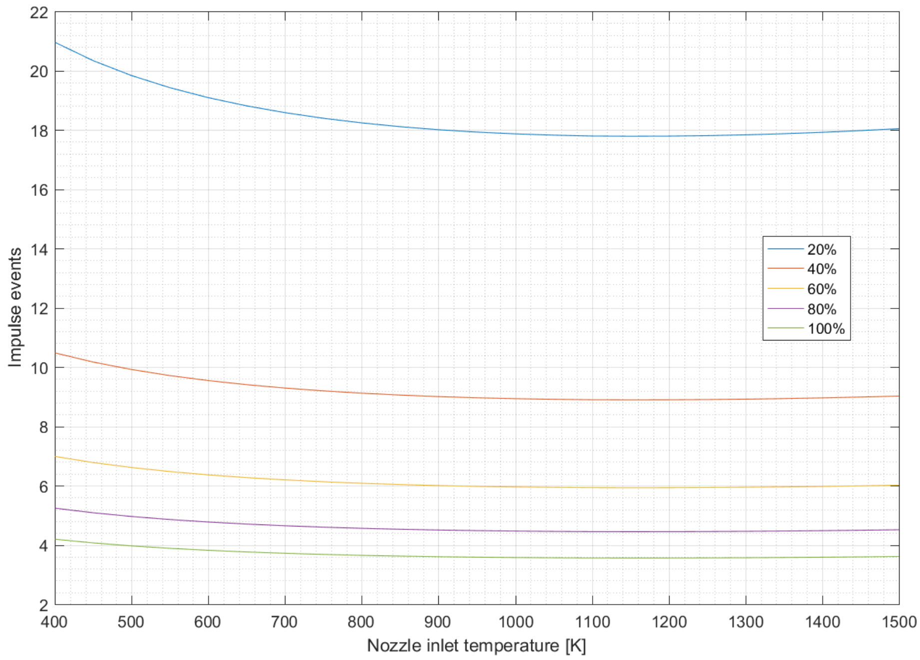

Figure 5.1.3: Total battery cycles for various nozzle inlet temperatures and power conversion efficiencies

Ultimately a mission-dependent adequate balance between mass, volume, and efficiency needs to be found. If the CubeSat can harvest enough energy to account for thermal losses but has a very limited volume for the propulsion system, a high-temperature superheating system with a low degree of insulation can be designed. On the other hand, if more volume is available for a CubeSat that has a low capability of harvesting energy from the sun, maximizing power conversion efficiency should be the main goal.

In this case, to achieve a specific impulse higher than 200s, 1300K is set as the target temperature at the nozzle inlet, resulting in almost 260s of ideal I_{sp}.

5.2 Heating Element

As it has been stated previously, the heating wire transfers heat to the superheater, and the superheater heats the propellant. To make the superheater as small and light as possible, the heating wire needs to operate at the highest temperature possible, dissipating enough heat for fluid heating and thermal losses. Since the wire is radiating and in contact with the solid superheater, the wire's temperature cannot exceed the superheater's maximum temperature, and the superheater needs to be an electrical insulator.

Several materials are available for the heating wire:

- Tungsten results interesting because of its melting point of above 3000K, but the wire is in contact with the solid superheater, and there is very limited availability of electrically insulating material that can withstand 3000K. Tungsten wire can be used at lower temperatures so that it is compatible with available materials, even if tungsten's spectral emissivity does not exceed 0.4. Heat exchange by radiation of very hot surfaces increases with the fourth-order of the hot surface's temperature, resulting in a small radiative area. However, tungsten wire's electrical resistivity is low compared to other candidates ($5.6 \cdot 10^{-8}\Omega m$ vs $1.5 \cdot 10^{-6}\Omega m$), resulting in wires of very small diameter so that both voltage and current meet the power bus restrictions.

- Some chromium alloys are electrical conductors with an electrical resistivity up to 100 times higher than tungsten, and infrared spectral emissivities ranging from 0.7 (Kanthal A1, FeCrAl, limit temperature 1670K) to 0.9 (Nikrothal 80, NiCr, limit temperature 1470K) [22]. These alloys can operate up to 1470K-1670K, while ceramic materials that allow continuous operation below 2000K are common. Usage of these alloys results in more rigid wire spires and simpler manufacturing of the cavity containing them. FeCrAl alloys result better than NiCr alloys in terms of heat transfer. Assuming a simple radiation model, according to equation 5.2.1, having both materials at their respective limit temperatures, FeCrAl alloys transfer more heat than NiCr alloys with the same radiative area for all receiver temperatures (see figure 5.2.1.

$$\begin{aligned} \frac{q_{FeCrAl}}{\sigma A} &= \epsilon_{FeCrAl}\left(T^4_{FeCrAl} - T^4_{receiver}\right) \\ \frac{q_{NiCr}}{\sigma A} &= \epsilon_{NiCr}\left(T^4_{NiCr} - T^4_{receiver}\right) \end{aligned} \tag{5.2.1}$$

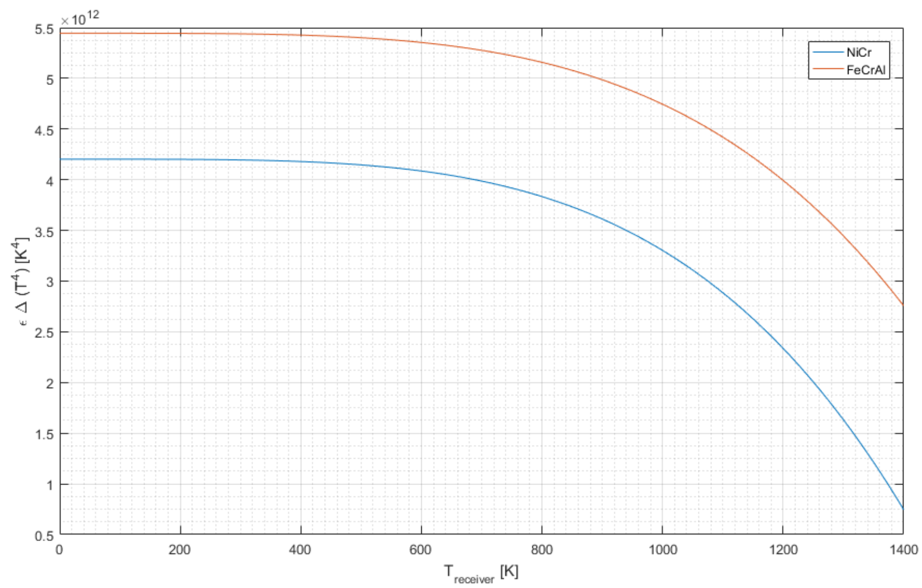

Figure 5.2.1: Heat transfer comparison for FeCrAl vs NiCrAl

5.3 Superheater

The superheater receives energy from the heating element and mainly transfers it to the fluid, but also loses heat as it is the second hottest element of the system. As described in section

3.1.2 minimizing its' volume reduces heat losses, but there's a trade-off between reducing heat losses and accommodating both heating wire and fluid ducts. The superheater is a component that affects every aspect of the propulsion system: thermally insulating a very hot component and redirecting lost heat for its recovery is what finally determines the system's efficiencies.

Initial restrictions for the superheater are described in section 5.3.1. Using the fluid submodel with different duct lengths and diameters, pressure losses and final fluid temperatures are evaluated in section 5.3.2 to select a duct geometry that will act as a starting point to reach the target 200s of specific impulse. Section 5.3.3 shows how the wire and the ducts are accomodated in the superheater. In section 5.3.4 heat transfer between the wire and the solid superheater is studied to determine the wire's section and exposed area in the proposed designs, selected to fit both dissipated power requirements as well as electrical requirements imposed by the energy bus. This is performed using part of the thermal circuit, specifically the resistance between the wire and the superheater, and the electric submodel. In section 5.3.5 insulation methods for the superheater are evaluated to improve the device's power conversion efficiency. Manufacturing concerns for the superheater are briefly discussed in section 5.3.6 and section 5.3.7 finally provides a summary of the conclusions drawn from the above-mentioned sections.

5.3.1 Initial restrictions

The main geometrical restriction encountered is that the superheater's fluid outlet must be aligned with the nozzle inlet, as the path between both must be kept as short as possible to prevent the fluid from losing heat. With the nozzle pointing towards outer space the superheater's outlet is defined, therefore it makes sense to fix the component by grabbing it from the outer and inner faces as depicted in figure 5.3.1: these fixing points are unavoidable conduction heat losses, but the superheater's remaining exposed area is connected to other parts of the propulsion system by either radiation or conduction, depending on which combination of both results in the most balanced design considering impulse and power conversion efficiency, volume and weight, and system controllability. It is also important to notice, that some of these connections by conduction and radiation will determine how much heat lost by the superheater is recovered and used to evaporate.

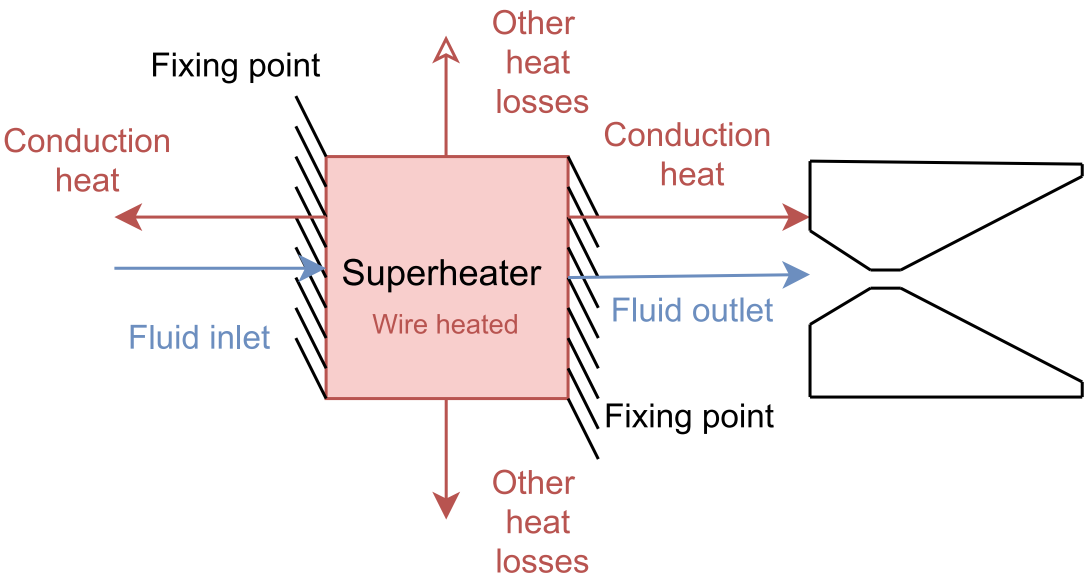

Figure 5.3.1: Superheater fixing and fluid diagram

The superheater is determined to be cylindrical, making the device as axisymmetrical as possible to simplify the heat transfer model. In addition, cylinders of a diameter d have a lower exposed area than squares of side d, decreasing heat losses. Regarding the superheater's aspect ratio, it is determined at a later stage, since it has an impact on heat transfer, and on how both ducts and wire are accommodated.

5.3.2 Duct geometry analysis

To generate the designs with adequate dimensions, several duct diameters and lengths are evaluated. To simplify the design and testing of the component, the duct's diameter is constant. Multiple ducts carrying a portion of the mass flow are not studied: to ensure equal flow in all ducts the superheater should contain a plenum increasing the solid's volume and increasing heat losses, or with a plenum outside the superheater multiple fluid inlets would increase the likelihood of leaks.

Using the fluid submodel, without integrating it yet into the full design process, allows for the first estimation of duct length and diameter for a range of efficiencies, but the following assumptions are made which are not final:

- Vapor chamber pressure: considering the satellite's interior temperature is roughly 283K, superheating is assumed. Even if the calculated saturation pressure in the first iteration is not finally the original one chosen, it is useful to observe trends for superheaters with different duct diameters and lengths. A difference of above 50K with the satellite's temperature is used to successfully simulate a wide range of duct diameters. If the initial pressure is not high enough the fluid can reach a Mach number above 0.5 towards the end of the duct invalidating simulation onwards, as the heat transfer correlation described in section 4.1 can no longer be used.

- Superheater temperature: assumed 1400K initially. The target temperature for the fluid is 1300K. 100K difference with the solid is proposed. It is unlikely that the fluid reaches a temperature equal to the superheater. Less heat transfer occurs the lower the temperature difference between fluid and solid, with less fluid temperature gain at later stages for longer ducts, but with the same impact on occupied volume and possible exposed area for heat transfer.

- Mass flow: it depends on a wide variety of variables that are not yet determined such as power conversion efficiency and propellant conditions at the nozzle's inlet among others, but it is impossible to achieve a viable product without making an educated guess first. As a starting point power conversion efficiencies η_{power} ranging from 20 to 100% are assumed according to equation 5.3.1. The final temperature is assumed as the superheater temperature since it is the temperature the fluid would reach in an infinite length duct, while the final pressure is assumed to be the starting pressure. Naturally, pressure at the nozzle inlet is lower due to friction, but enthalpy changes for water are much more sensitive to changes in temperature than to changes in pressure.

$$\dot{m} = \frac{\eta_{power} P_{budget}}{h(T_{sh}, p_{sat}(283K)) - h(283K, p_{sat}(283K))} \tag{5.3.1}$$

Figure 5.3.2 shows results for different ducts, with varying power conversion efficiencies and vapor initial pressures. Duct diameters vary from $1.5mm$ to $6mm$. However, manufacture of diameters between 1 and 1.5mm is also possible. Smaller diameters than $1mm$ are not studied due to the manufacturing restrictions imposed by the nozzle's throat diameter, being the smallest throat diameter $1mm$. With a Mach number of 1 at the nozzle's throat, the simulation imposed 0.5 Mach number limit is never reached if the superheater duct's cross-section is equal to the throat's.

It can be observed in figures 5.3.2b, d, f and h that the fluid's final temperature is not very dependant on the duct's diameter, as the forced convection coefficient does not depend on the fluid's Reynolds number. A very small decline in final temperature is observed with reduced diameters ($10K$) due to a higher pressure loss and a decrease in the fluid's thermal conductivity, but it is very small compared to the fluid's temperature jump in the component ($> 500K$ even for shorter ducts with high efficiency). Although slight temperature differences are seen in figures 5.3.2d and h, they are attributed to different starting temperature for the simulations, with different inlet temperatures (353K and 343K respectively).

On the other hand, power conversion efficiency and the duct's length are much more linked. Since the convection coefficient doesn't change with the mass flowing through the duct, less enthalpy jump and therefore temperature jump is to be expected for higher mass flows. For inefficient systems, the ducts can be short as the mass flow is inevitably lower than inefficient designs.

Changes in pressure due to the combined effect of heating and friction are related to the mass flow, diameter, and length. For a fixed mass flow, the Reynolds number is calculated according to equation 5.3.2.

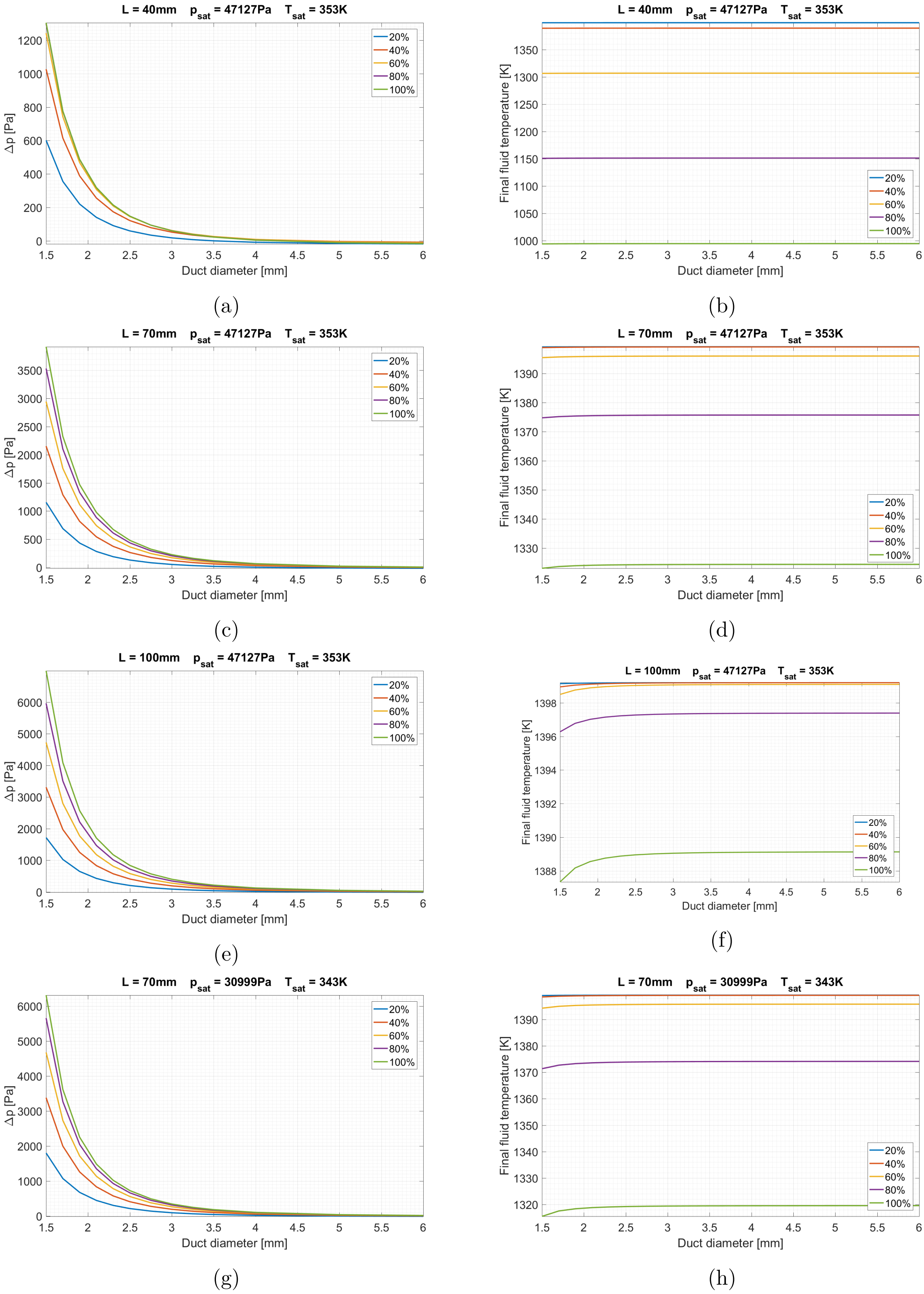

Figure 5.3.2: Pressure drops and final fluid temperatures for varying duct lengths, diameters, and initial steam pressures

$$Re_D = \frac{\rho v D}{\mu} = \frac{\dot{m} D}{A\mu} = \frac{4\dot{m}}{\pi D \mu} \tag{5.3.2}$$

The pressure loss ends up being related to fluid properties such as the dynamic viscosity μ and density ρ, and the superheater's parameters. Pressure losses due to friction for adiabatic compressible flow [15] are shown in equation 5.3.3.

$$\begin{aligned} dp &= -\frac{\rho v^2}{2} f \frac{dx}{D} = -\frac{\rho}{2}\left(\frac{\dot{m}}{\rho A}\right)^2 \frac{64}{Re_D}\frac{dx}{D} \\ dp &= -\frac{\mu}{\rho}\frac{128\dot{m}}{\pi D^4} dx \end{aligned} \tag{5.3.3}$$

Figure 5.3.2 (a, c, e and g) show a very steep decrease of pressure drop (due to the combined effect of friction and heat transfer) with diameter, and also increased pressure drops for higher mass flows (higher efficiencies) and duct lengths. In addition, comparing figures 5.3.2c and 5.3.2g pressure loss increases when the input pressure is decreased, as density is lower across the whole process.

The following conclusions to determine an adequate superheater duct geometry can be drawn:

- Duct length depends on the desired fluid temperature at the outlet and the system's overall power conversion efficiency. High fluid temperature designs require longer ducts, but enlarging the superheater's volume, keeping in mind that large superheaters impact the efficiencies of the system.

- Duct diameter depends on the steam's initial pressure. Small diameters require steam pressures that are only achieved by active tank heating, which impacts the system's startup energy. Diameters of more than 3mm have very low-pressure losses, but take up more space resulting in previously described efficiency and controllability issues.

- Vapor inlet pressure should be raised as little as possible from 283K to satisfy the Mach number conditions in the duct, keeping in mind that higher inlet temperature requires more preheating.

From this limited analysis, it is observed that a duct length of the order of 70mm is adequate. It successfully heats mass flows above 1300K even for 100% power conversion efficiency, resulting in an ideal specific impulse above 250s. Of course, this is subject to changes, as the superheater temperature is still unknown, but serves as a good starting point to start a design iteration.

Duct diameter is selected at a later stage as this submodel alone does not provide enough information about the decision. The two main parameters that affect the duct's diameter are the following:

- Final volume of the superheater: important when designing for improved power and energy efficiency and controllability. Low duct diameters allow for more compact superheaters with decreased heat losses.

- Required steam's initial pressure: determines how much power needs to be used in the tank to raise the liquid propellant's pressure. High duct diameters require less tank heating due to decreased friction pressure losses.

5.3.3 Duct and wire disposition and superheater dimensions

To minimize the volume occupied by the superheater, the duct in the cylinder takes a complex shape explained in figure's 5.3.3 transversal section. Only the component with the ducts is shown in this section for simplicity.

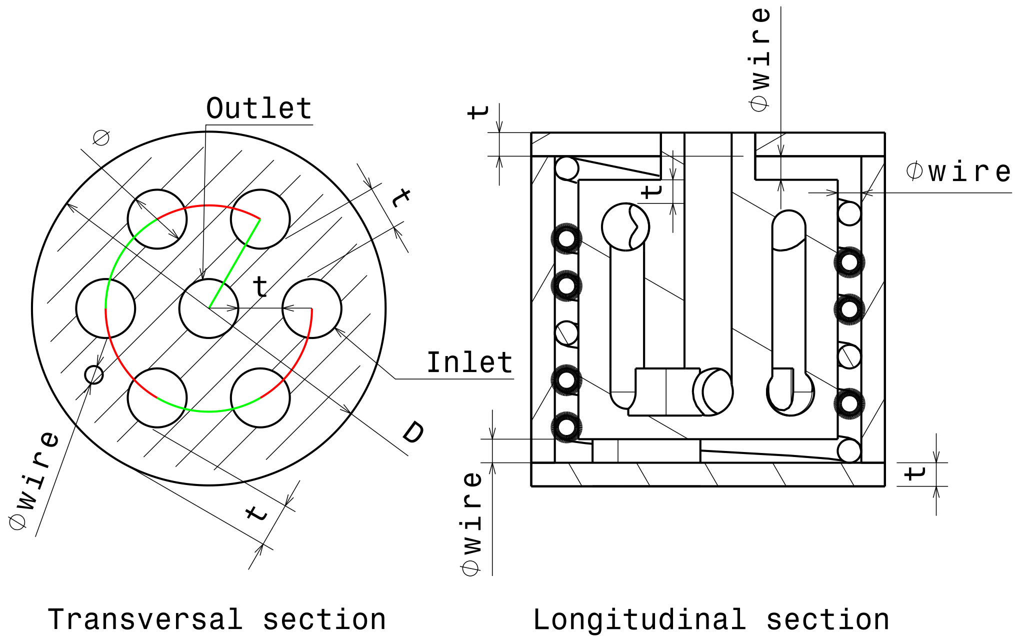

Figure 5.3.3: Superheater parametric dimensions

The duct is composed of several straight ducts that are connected through upper and lower curved ducts. Figure 5.3.3 shows red lines representing curved ducts, connecting straight ducts on the outlet side of the superheater. Green lines connect straight ducts on the inlet side. To have a constant spacing between all ducts, a central duct which is the outlet duct is surrounded by 6 ducts.

With a fixed spacing between the ducts and fixed duct diameter, changing the duct's length changes the straight duct's dimension and the overall length of the superheater. Minimum thickness is also involved as seen in the longitudinal section of figure 5.3.3.

The heating wire is seen in the longitudinal section, enclosed by three extra ceramic components and the component containing the ducts. The wire, therefore, radiates to the ceramic, modeled in more detail in section 5.3.4.

The superheater is, therefore, dimensioned defining 4 variables:

- Superheater's minimum thickness t
- Superheating's resistor diameter ϕ_{wire}

- Superheater's duct diameter ϕ
- Superheater's duct length

The minimum thickness for the superheater is considered $1mm$. The rest of the variables are determined at a later stage by using the full simulation model that includes both solid and fluid thermal analysis.

5.3.4 Wire-Superheater heat transfer

The wire is either in contact with the superheater or radiating to it through two very close surfaces as depicted in figure 5.3.4.

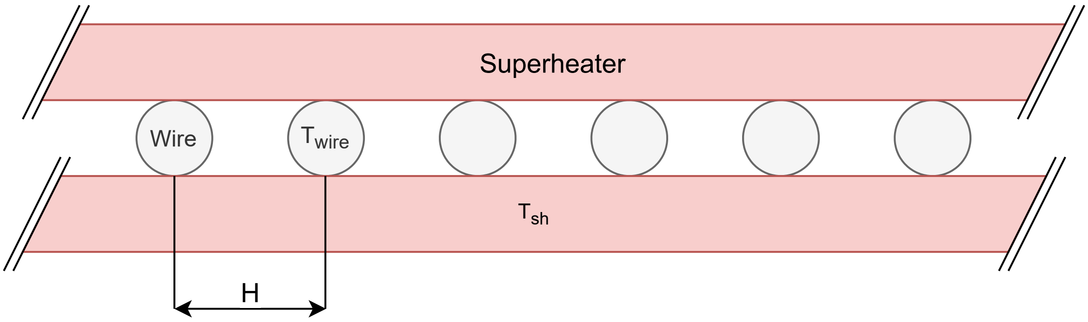

Figure 5.3.4: Wire and superheater geometric disposition

Assuming the worst-case scenario, the wire is radiating through its' surface to the superheater and no contact resistance is modeled. Therefore, the view factor between the superheater and the wire F_{w-sh} is very important to determine the required wire length and diameter. Heat transferred between the wire and the superheater is determined by equation 5.3.4, and it depends on both material's temperatures T_{sh} and T_{wire}, emissivities ϵ_{sh} and ϵ_{wire}, heat exchange areas A_{sh} and A_{wire}, as well as the previously mentioned view factor.

$$q = \frac{A_{wire}\sigma(T_{wire}^4 - T_{sh}^4)}{\frac{1}{\epsilon_{wire}} + \frac{1}{F_{w-sh}} + \frac{A_{wire}}{A_{sh}}\frac{1-\epsilon_{sh}}{\epsilon_{sh}}} \tag{5.3.4}$$

To increase the transferred heat both materials' emissivities should be maximized. The wire's material is FeCrAl and has a moderate emissivity as reported in section 5.2 and a high limit temperature, but the material selected for the superheater must have an emissivity that allows adequate heat transfer. Sintered ceramic materials are materials that could provide emissivities higher than 0.8 and as high as 0.95 [23]. Of those ceramic materials, silicon nitride is the most attractive due to it fulfilling all the requirements for the superheater: it is electrically insulating, with high emissivity, an acceptable thermal conductivity ($25\frac{W}{mK}$), and can be manufactured through sintering, enabling for complex shapes to fit the fluid's duct with no leakage in the smallest volume possible [24].

Increasing the wire's radiative area improves heat transfer, but it also affects electrical and volume restrictions. If the wire's cross-section is too big, the current will surpass the bus-imposed 10.4A limit and the final superheater's volume will increase.

The superheater's radiated area should be minimized and the view factor between both components must be maximized, but these two variables are connected.

Wire spires radiate at adjacent spires, therefore the wire interferes with itself when transferring heat to the superheater. This interference is modeled with the wire's view factor found on [25] according to the wire's separation H and radius r. View factor between two cylinders F_{w-w} is determined by equation 5.3.5.

$$F_{w-w} = \frac{\sqrt{(\frac{H}{r})^2 - 4} - \frac{H}{r} + 2arcsin\left(\frac{2}{\frac{H}{r}}\right)}{2\pi} \tag{5.3.5}$$

View factor F_{w-sh} is affected by one cylinder radiating to two other cylinders (one on each side). Equation 5.3.6 determines the final view factor to use in the wire-superheater heat transfer.

$$F_{w-sh} = 1 - 2F_{w-w} \tag{5.3.6}$$

The inner component of the superheater is designed to have a determined length and diameter, therefore A_{sh} varies only with wire diameter, not with wire distance. View factor F_{w-sh} increases with wire distance H, but A_{wire} decreases the more separated wires as fewer spires fit in the superheater. An equilibrium between wire diameter, distance, and length must be found to maximize heat transfer and achieve voltages and currents allowed by the energy budget.

To estimate the required length for the wire, and the diameters that satisfy both voltage and current requirements, equation 5.3.4 is solved for the wire's length with some assumptions:

- 50W dissipated through the superheating resistor
- View factors between 0.64 (minimum view factor F_{w-sh} according to equations 5.3.5 and 5.3.6, for two cylinders in contact with eachother) and 1
- Superheater temperature is set at 1400K, with 0.95 emissivity
- Area ratio between superheater and wire is considered 1, due to no information on the superheater geometry This decreses the precission of the estimation
- Limit voltage is 6V
- Limit current is 10.4A
- Wire temperature is 1670K, with 0.7 emissivity and $1.52 \cdot 10^{-6}\Omega m$ electrical resistivity according to the manufacturer's data

Figure 5.3.5 shows that the expected wire diameter is between 0.65 and 0.95mm, with lengths from 350 to 150mm. Dotted lines represent limits for 6V and 10.4A for all configurations. Voltage and current variation with length can be seen in figure 5.3.6 for 1400K and view factor 1.

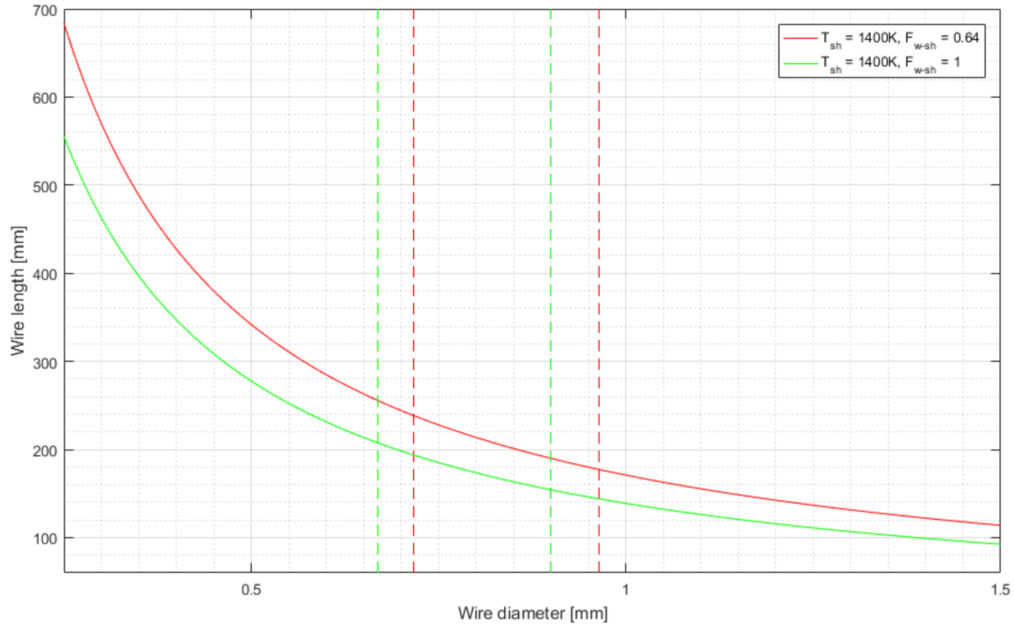

Figure 5.3.5: Wire length required versus diameter for various cases

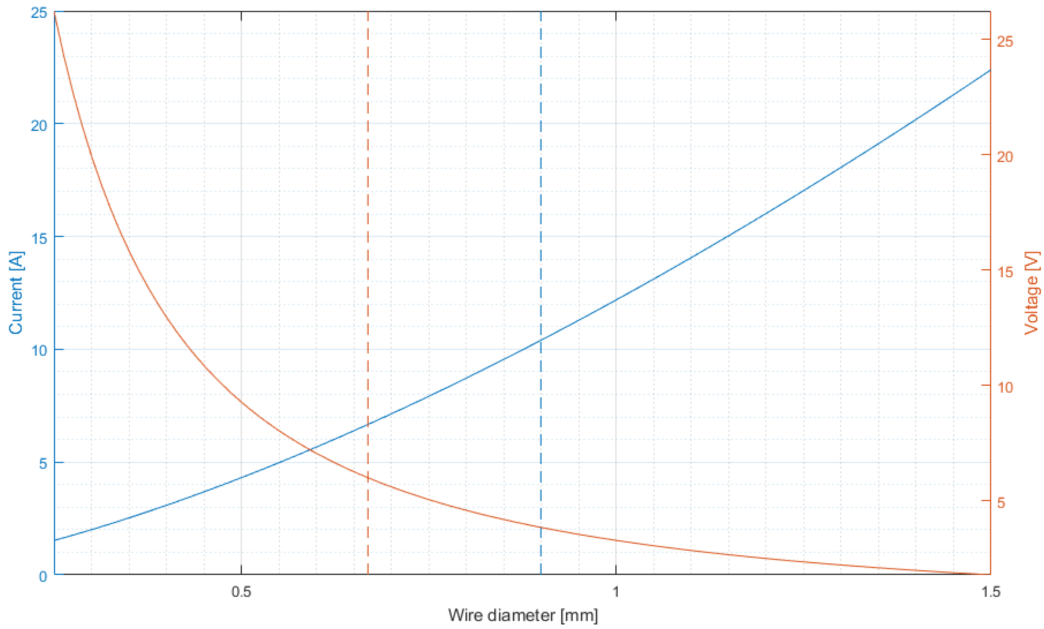

Figure 5.3.6: Current and voltage for every length and diameter, with superheater at 1400K and $F_{w-sh} = 1$

Diameter can be lower than 0.65mm due to the superheating resistor dissipating less than 50W, and the area ratio between the superheater and the wire being lower than 1.

The smallest diameter for Kanthal A1 wire is gauge 25 (0.45mm), therefore a wire that satisfies both thermal and electric requirements can be found.

5.3.5 Insulation analysis

Once a superheater concept has been proposed, methods for its' insulation can be explored. The superheater as a cylinder loses heat through its curved face, as well as through its planar faces where the inlet and outlet for the fluid are located.

The planar faces of the superheater are connected to the aluminum structure that holds it in its place, depicted in figure 5.3.7 as the inner and outer lids. As heat is lost through the sides of the superheater, a nested design is proposed where water surrounds the superheater. The superheater can't be submerged as all the heat would be used in evaporation and it would fail to raise its temperature much higher than the liquid water. Therefore water is stored in a compartment named water accumulator, physically separated from the superheater itself as depicted in figure 5.3.7, but receiving heat and using it to transform liquid water into steam. It is important to notice that not only heat lost through the side of the superheater will evaporate: part of the conduction losses through the fixing points can find their way to the water through the contact between the water evaporator and the lids.

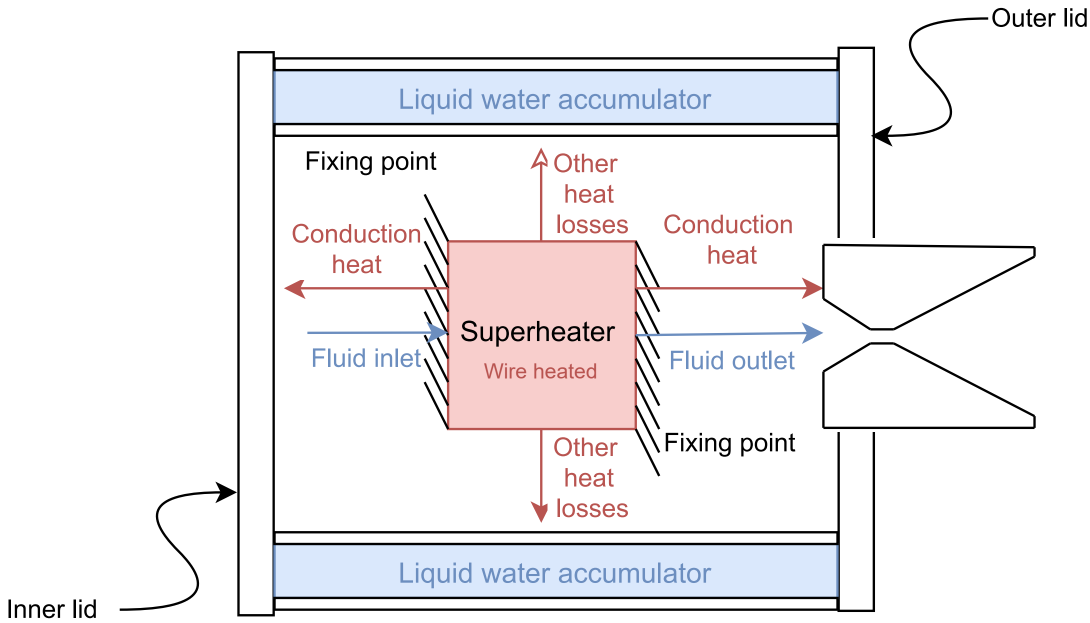

Figure 5.3.7: Superheater fixing, fluid and water location

5.3.5.1 Outlet and inlet insulation

Figure 5.3.8 shows paths for heat to leave the superheater.

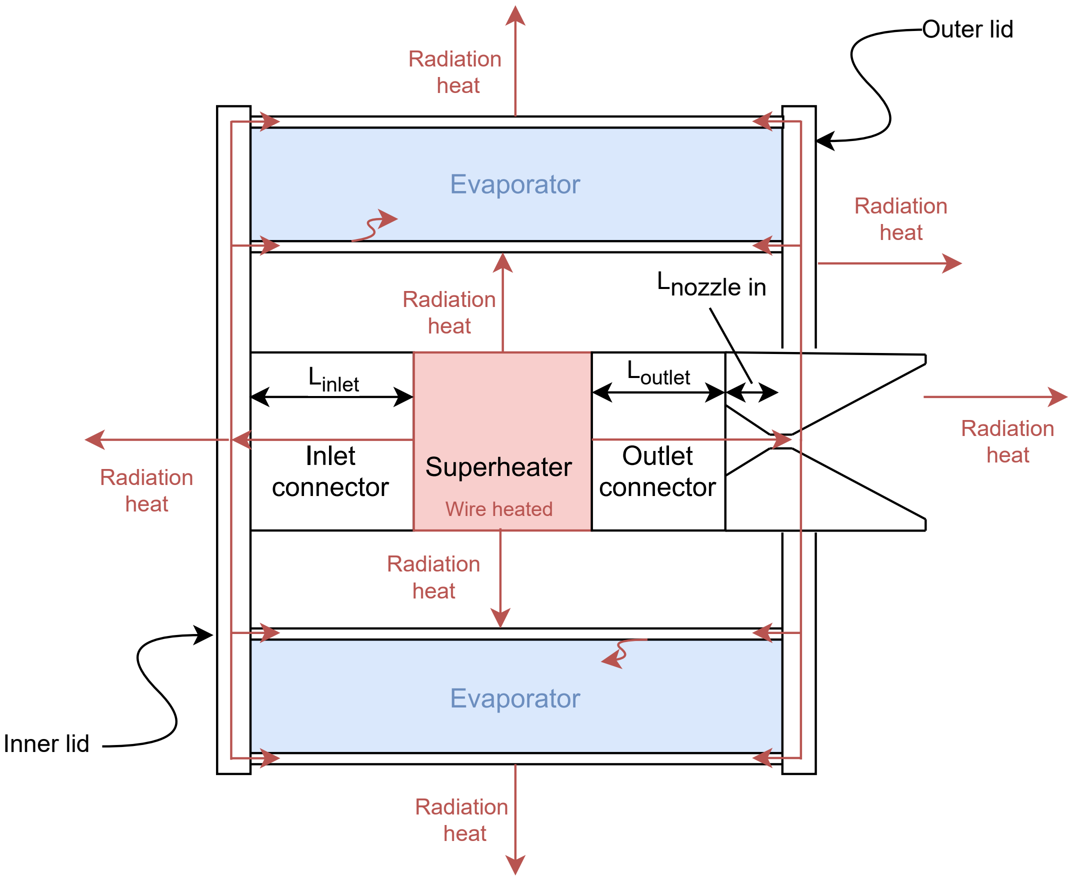

Figure 5.3.8: Outlet and inlet insulation, with heat paths in red

The metallic lids cannot be directly connected to the superheater, otherwise the whole device's structure's temperature will be similar to the superheater's, resulting in massive heat losses and very low efficiencies. Therefore, outlet and inlet insulations need to meet several conditions:

- Outlet:
  - Connector between superheater and nozzle required to be as short as possible to prevent fluid from losing temperature (and therefore specific impulse). Since heat is lost through the insulation, the temperature gradient is negative from the superheater to the nozzle, making the fluid lose heat. A longer connector also radiates more heat to the evaporator.
  - Nozzle fixing points to the lid are at similar temperatures as they are in contact with each other. The nozzle fixing points and the water accumulator walls are at a similar temperature due to the high conductivity of the aluminum lid. The temperature of the accumulator walls needs to be within a specific temperature range as it determines evaporated mass (described in section 5.4.
  - Nozzle surfaces as well as the lid's outer face radiate towards outer space losing heat. These heat losses should be reduced as much as possible keeping in mind that heat

coming from the superheater can either leave through radiation or be redirected to the water reservoir and result in more evaporated mass. If losses through radiation are low, but with a high heat flux coming from the superheater, this excess heat will result in evaporation.

- Inlet:
  - Connector between superheater and lid needs to be long enough to allow thermal gradient between the superheater and the inner lid. Excessive connector length can result in volume issues for the device and excessive evaporation.
  - Outer lid temperature similar to water accumulator's wall.
  - Reduce radiation losses to the inner satellite temperature.

Insulators are designed to prevent heat losses and to hold the superheater in place. Materials with the lowest thermal conductivity possible are used, but in some components, higher mechanical strength is required, negatively impacting thermal conductivity. Conduction connectors are split in two, with a very low conductivity ceramic fiber (0.2 $\frac{W}{mK}$ [26]) in a blanket form that is unable to withstand any mechanical load induced by lift-off, and a solid ceramic with high mechanical strength (800MPa compression strength) as alumina silicate with a conductivity of $2.2\frac{W}{mK}$ [27].

High strength ceramic is used as both the inlet and outlet duct for the superheater, while also ensuring that the superheater position is fixed.

5.3.5.2 Side insulation

As mentioned previously, it makes sense to use the heat coming from the side of the superheater to evaporate water. Therefore, alternatives between radiation and conduction are studied to connect the superheater to the evaporator.

Figure 5.3.9 shows a thermal circuit that allows comparing heat lost through different insulation proposals that alternate between conduction and radiation. A temperature of 1400K is set to the superheater and 400K is the determined temperature of the water accumulator's wall. 400K is selected as it is in the range of temperatures to be expected since liquid water at 350K (used as the saturation temperature in section 5.3.2). More details regarding the evaporator's temperature are given in section 5.4

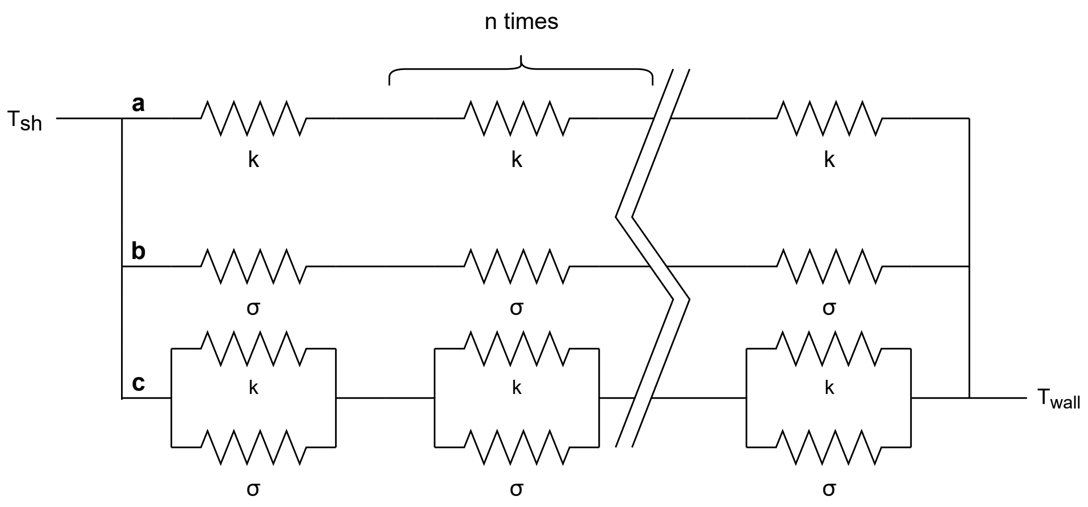

Figure 5.3.9: Thermal circuit used to compare heat transfer modes

Assuming a cylindrical superheater, there are three mechanisms for the heat to travel from the superheater to the water accumulator:

a. Regular conduction losses with varying insulation diameter, achieved by the accumulation of series resistances

b. Several series radiation resistances, having the radiative surfaces held by the lids (conduction resistances between radiative surfaces are considered negligible due to the high conductivity and low thickness of metallic components)

c. Radiation resistances with small conduction connectors, to account for the components holding the radiating surfaces

Resistances are calculated and the thermal circuit is solved as described in section 4.3. Solids for the three circuits are displayed in figures 5.3.10.

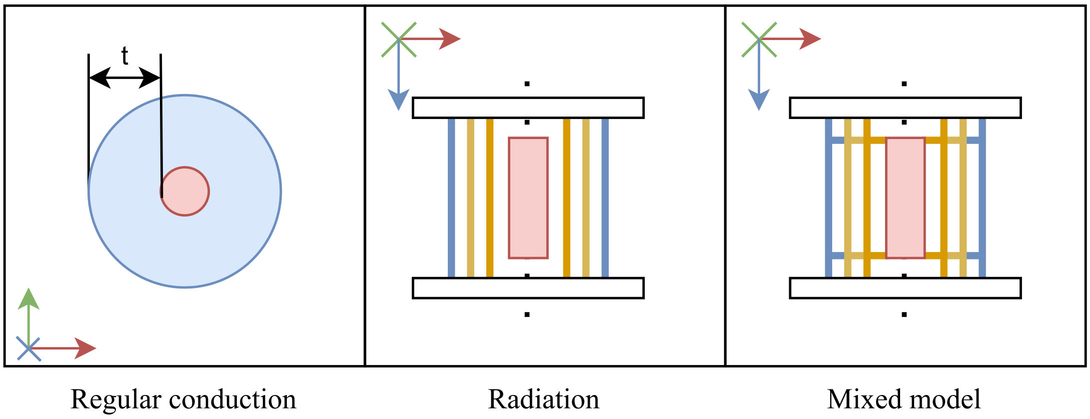

Figure 5.3.10: Solids for different heat transfer modes

Figure 5.3.11 shows heat lost from the side of the superheater for the three proposed insulation methods. Superheater diameter and length are assumed to be 18 and 15mm respectively since they can fit 70mm duct for 2.25mm duct diameter, a diameter that can be used with nozzles up to 2mm. It is seen that using a ceramic material with a thermal conductivity as low as $0.2\frac{W}{mK}$ [28] heat losses are several times greater than in systems that involve radiation.

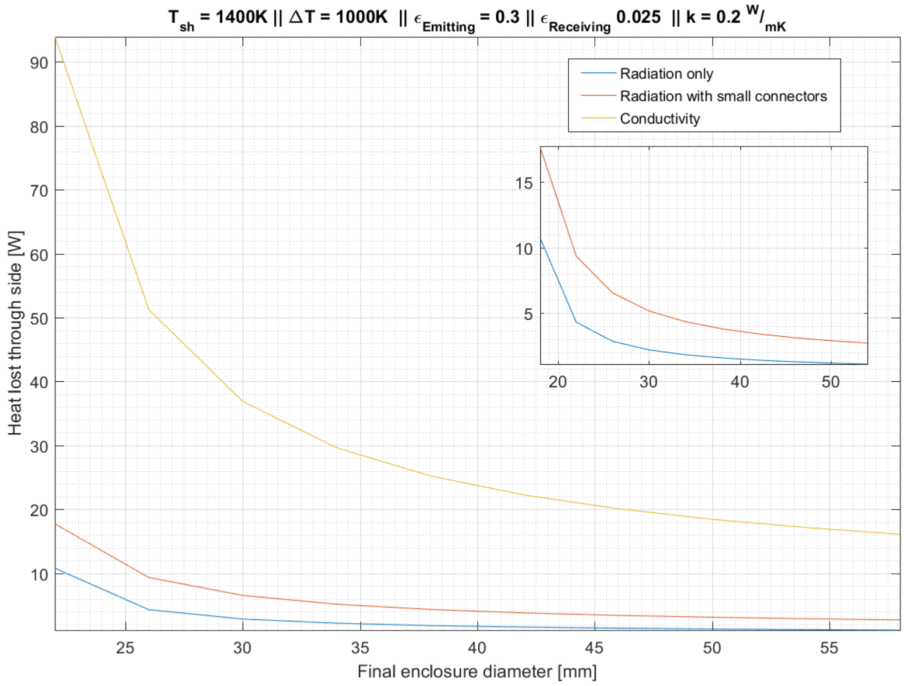

Figure 5.3.11: Heat lost from the superheater for different heat transfer methods and varying number of insulation stages

Having parallel radiation and conduction is a much better solution from an insulation perspective, but has a rather difficult manufacturing and a very clear disadvantage: thermally insulating separators must hold the radiative surfaces, having to endure vibrations during liftoff. Due to flexural and compression strengths lower than 1 MPa of the very insulating separator, this ends up discarded.

Radiation only heat transfer results in the best method for insulating the side of the superheater. While multiple radiation stages decrease heat losses by acting as a multi-layer-insulating blanket, this option is not viable as intermediate layers would be at high temperatures. Since aluminum inner and outer lids hold these metallic layers, heat would be conducted through the lids instead of being radiated through the layers. To decrease conducted heat from intermediate layers to the lid only one radiation resistance must be involved, with a radiated layer's temperature similar to the outer lid's temperature, and with a temperature differential with liquid propellants that enables controlled evaporation.

Heat transfer by radiation depends on the emissivities of both emitting and receiving surfaces: both emissivities should be reduced to decrease the exchanged heat. As stated in section 5.3.4

high emissivity is needed on the inside of the superheater to achieve heat transfer with efficient use of space in the superheater, but low emissivity on the outer face is required. Coatings that can withstand temperatures as high as 1400K with low infrared emissivity were not found. A metallic cover for the superheater of a material such as a grade 5 titanium results ideal: it can operate up to 1900K and has an emissivity of 0.3 at 1400K. The radiated layer is at a much lower temperature, and reflecting coatings are much more available: with gold plated metallic materials (temperature limit 700K) that can achieve infrared emissivities as low as 0.03 [29], heat losses are reduced even with one stage and the system gains controllability since less heat ends up evaporating propellant.

As the selected heat transfer method is radiation, the design must ensure that leaked propellant does not remain between the superheater and the radiated layer. This steam layer would act as a conduction resistance with thermal conductivity of at least $0.015\frac{W}{mK}$ (thermal conductivity for steam at 283K, lowest water temperature possible). It is observable in figure 5.3.11 that heat lost with thermal conductivity of $0.2\frac{W}{mK}$ is 90W and recalculating with a conductivity that is 10 times smaller heat lost should be 9W, approximately equal to the heat lost through radiation.

To generate a vacuum between the superheater and the radiating layer, paths for steam leakage into outer space are created between the nozzle and the outer lid. Since leakage exit can't generate thrust in any direction, two opposite slots are manufactured so that the net force exerted by the leaving fluid is zero. Figure 5.3.12 shows the slots performed on the nozzle, with red arrows showing the leaked propellant's path.

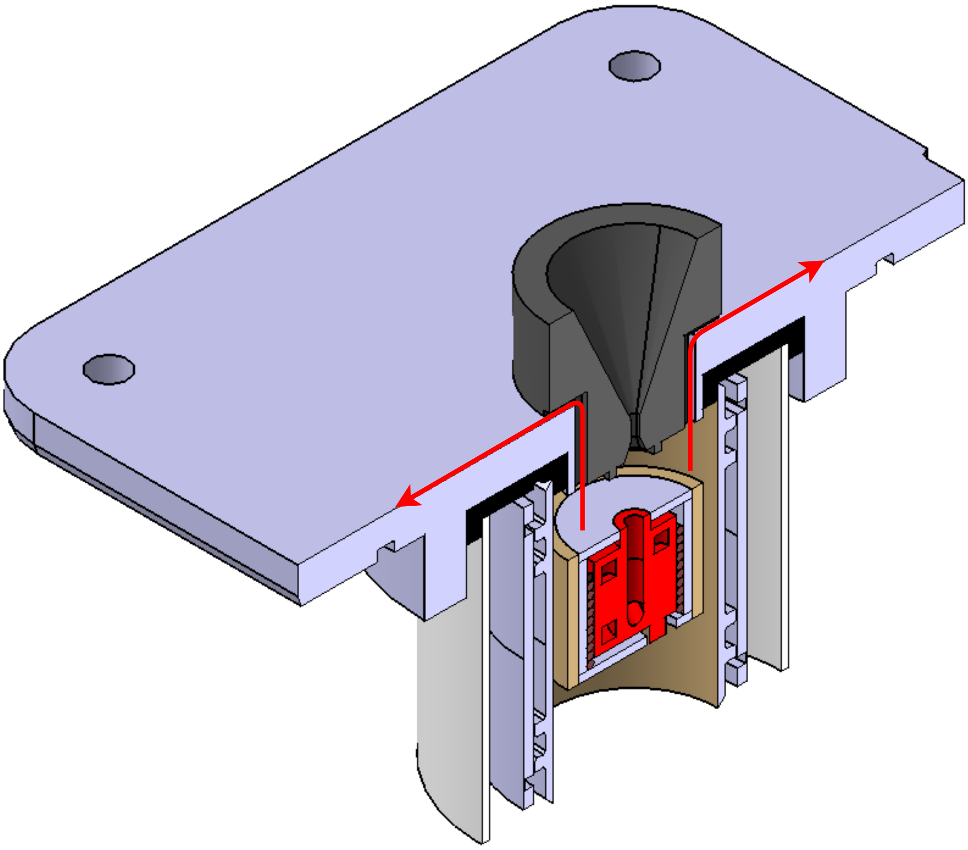

Figure 5.3.12: Vacuum generating slots and leakage path

5.3.6 Manufacturing

The superheater has a duct design that is not easily machined. Sintering is a manufacturing method that is compatible with the chosen material, and also allows for complex geometries with the adequate use of supports.

As sintered parts are costly, different materials or a slightly modified duct disposition can be used for testing, as long as the duct diameter and length are the same. The solid's temperature is the only factor affecting heat transfer if the material is conductive enough.

5.3.7 Superheater summary

The superheater is the most complicated subsystem of the device, and naturally many decisions are taken around its' restrictions and requirements. This section gives an overview of the engineering decisions taken from different heat transfer analyses concerning solid heating, fluid heating, and lost heat.

Design process in section 4 is not yet used, but preliminary dimensions available in table 5.3.1 are defined, ready to feed the complete model in order to get rid of any wrong assumptions or hypotheses made in the different models (i.e. steam initial pressure).

Symbol	Description	Value	Unit
D_{duct}	Duct diameter	2.25	mm
L_{duct}	Duct length	70	mm
L_{sh}	Superheater length	13.75	mm
D_{sh}	Superheater diameter (includes titanium cover)	18.75	mm
k_{sh}	Superheater thermal conductivity	25	$\frac{W}{mK}$
ϵ_{sh_i}	Superheater internal emissivity	0.9	-
ϵ_{sh_e}	Superheater external emissivity	0.3	-
ϵ_{cage}	Radiated surface emissivity	0.025	-
D_{wire}	Wire diameter	0.8	mm
L_{wire}	Wire length	250	mm
T_{sh}	Wire temperature	1670	K
q_{side}	Heat lost through side of superheater	$\sim$10	W

*All these variables are subject to changes

Table 5.3.1: Preliminar dimensions and relevant thermal characteristics of the superheater and related components

5.4 Evaporator

The evaporator has one requirement: supplying the superheater with gaseous propellant. This requirement can be split into two processes:

1. Steam generation
2. Steam separation from liquid water

This subsystem was placed surrounding the superheater in the previous section. This way evaporation is aided by lost heat from the superheater. A layer of static, liquid-propellant wraps the superheater to establish a low-temperature zone, with the propellant acting as a heat sink at a constant temperature. Figure 5.4.1 shows a diagram of how the evaporator ends up engulfing the superheater. In this diagram, the exterior shell is added, closing the steam chamber and connecting the inner and outer lids.

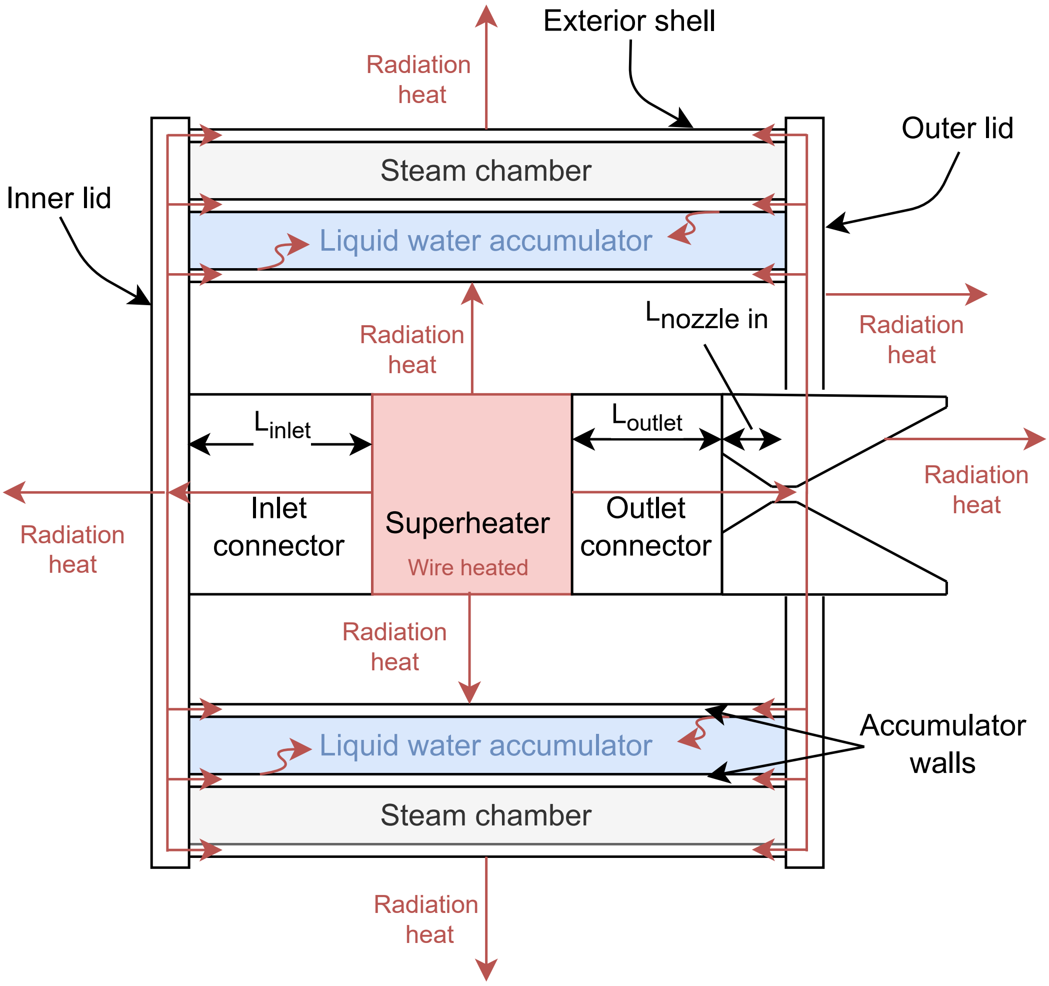

Figure 5.4.1: Outlet and inlet insulation, with heat paths in red

A short analysis is first presented on bubble formation in microgravity, and then heat sources that contribute to evaporation are listed.

5.4.1 Bubble formation and steam separation

Due to the absence of gravity, bubble nucleation, growth, and coalescence in space are not the same as in earth conditions. Experiments have shown nucleate pool boiling in microgravity to have different ranges of surface temperature and liquid subcooling, as the bubble's detachment mechanism from the surface changes. However, as long as the liquid is near saturation temperature, bubbles form with a maximum temperature difference of 100K between the heating wall and the liquid, with a heat flux of 500$\frac{kW}{m^2}$ [30].

The final temperature of the walls is unknown due to the absence in the bibliography of critical heat flux curves in microgravity since these curves provide the heat per unit area $q''(\Delta T_{wall-l})$ as a function of the temperature difference between the wall and the liquid. By varying the heat received by the evaporator, the design must achieve temperature differences of 0 to 100K between the liquid and solid walls while losing heat equivalent to the mass flow evaporation.

Figure 5.4.2 shows how water and vapor are disposed of in this subsystem and how bubbles are formed and separated from the liquid propellant.

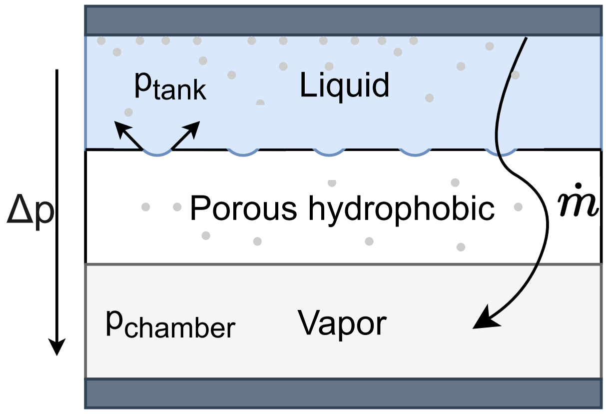

Figure 5.4.2: Evaporating process

Since the liquid is static, no inertia forces can detach the bubbles from the nucleating surfaces. The hydrophobic layer consists of a PTFE filter that allows the passage of bubbles into the steam chamber when they either nucleate on the filter surface, detach from the heating surface, or increase in size until they get in contact with the filter. The porous layer allows the passage of nucleated bubbles while the liquid is retained due to its surface tension.

By providing steam with a new mechanism to detach from the surface, the formation of a big bubble that engulfs the superheater, common in pool boiling events in microgravity [31], is avoided.

Steam is then discharged to a vapor chamber that will feed the superheater. This process is assumed to be isenthalpic, and having temperature and pressure for the liquid the specific enthalpy is known. The XSteam function allows for the calculation of the vapor's temperature according to its enthalpy, coming from the liquid properties, and pressure, obtained with equation 5.4.2.

Vapor pressure can be regulated taking into account that the pressure difference between the liquid and gas state is limited by the filter spacing and liquid-gas surface tension for water. Figure 5.4.3 shows the free body diagram for the interface between liquid and gas.

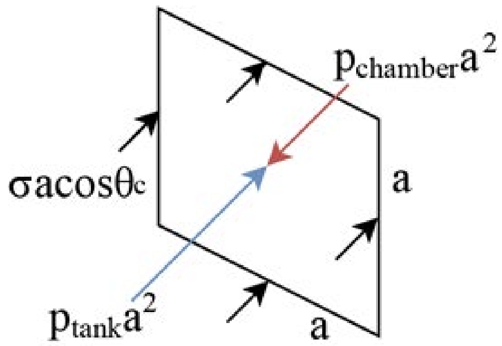

Figure 5.4.3: Force diagram for water in the mesh

According to the force diagram in figure 5.4.3, equation 5.4.1 determines the maximum pressure difference for a square mesh with spacing of side a, θ_c as the contact angle between the porous layer and the liquid, and σ as the surface tension between the liquid and gas. Equation 5.4.2 adds a safety factor f_s. Both equations still apply for a filter with circular holes of diameter a.

$$\Delta p_{max}a^2 + 4a\sigma cos(\theta_c) = 0 \tag{5.4.1}$$

$$p_{liquid} - p_{chamber} = \frac{\Delta p_{max}}{f_s} = -\frac{4\sigma cos(\theta_c)}{af_s} = 0 \tag{5.4.2}$$

A 20 micron PTFE filter has a contact angle of 120°. With a safety factor of 2 that results in a maximum Δp of 6000Pa even for temperatures up to 370K as it can be seen in figure 5.4.4. The mesh can withstand an easily measurable pressure drop without flooding the vapor chamber.

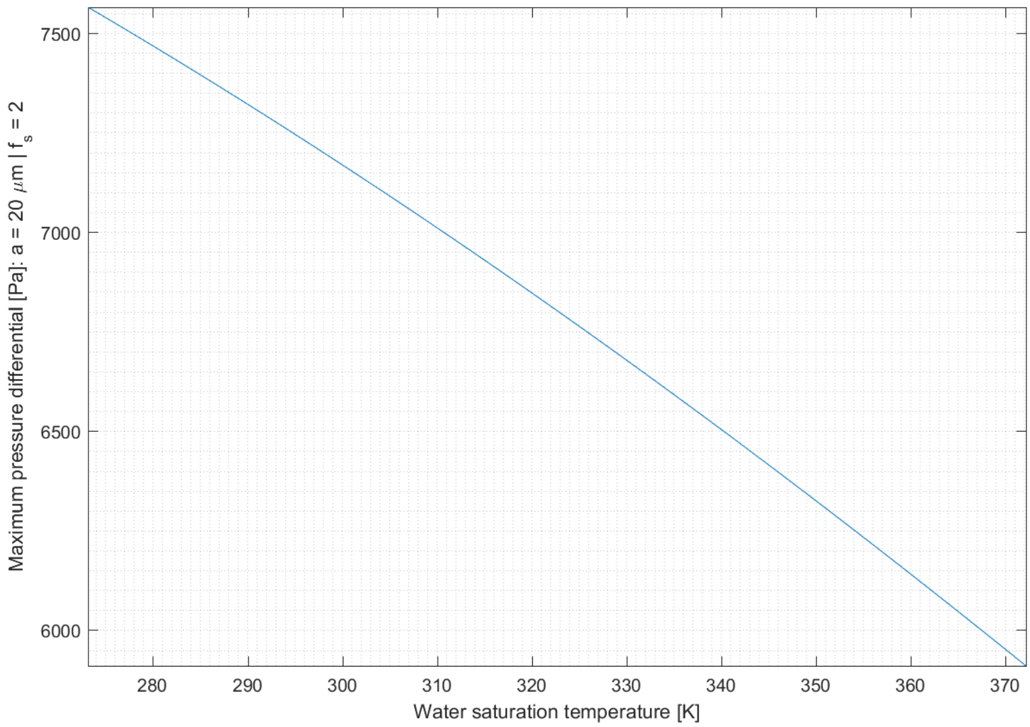

Figure 5.4.4: Maximum pressure drop in $20\mu m$ PTFE mesh

5.4.2 Heat sources

In addition to recovered heat, the system has an electrical resistor that serves as the second source for evaporation. Both the accumulator's wall and the PTFE filter, if their temperature is above the liquid saturation temperature, contribute to evaporation.

A balance must be reached between the needed evaporation and the heat losses: if there are more heat losses than necessary, too much propellant will be evaporated, leading to a loss in performance due to less superheating. Therefore, the inner wall of the water accumulator is electroplated to reduce the heat transfer from the superheater to the evaporator, so that heat losses fall short of the necessary power for evaporation.

The evaporating resistor's analysis is different from the superheater's. A lower temperature in the evaporator allows its resistor to operate at a temperature far from its' operation limit. This enables the usage of thermal pastes that decrease the thermal resistance between the wire and the object in contact with it.

Space thermal greases as Timtronics' High Performal Thermal Greases [32] are thermally conductive and electric insulators, which enable heat transfer from the heating wire to the accumulator's wall. Greases such as Timtronics' 615 Silicone grease have a thermal resistance of $2.9 \cdot 10^{-5} \frac{Wm^2}{K}$ and withstand up to 250°C or 523K, allowing for use in the evaporator, being the highest expected temperature approximately 450K [32].

Figure 5.4.5 shows the components in the evaporator and how the wire is electrically insulated and sealed. Seals are required so that water does not get in contact with the wire. The wire is contained in a cavity, with the thermal grease making contact with an electrically insulating PTFE film or machined component, which has a very similar limit temperature as the grease (260°C or 533K). The wire spires are almost in contact with each other so that the wire acts as a solid at a constant temperature. The spires can also be separated by thermal grease for safety since it has great dielectric strength of $17\frac{KV}{mm}$.

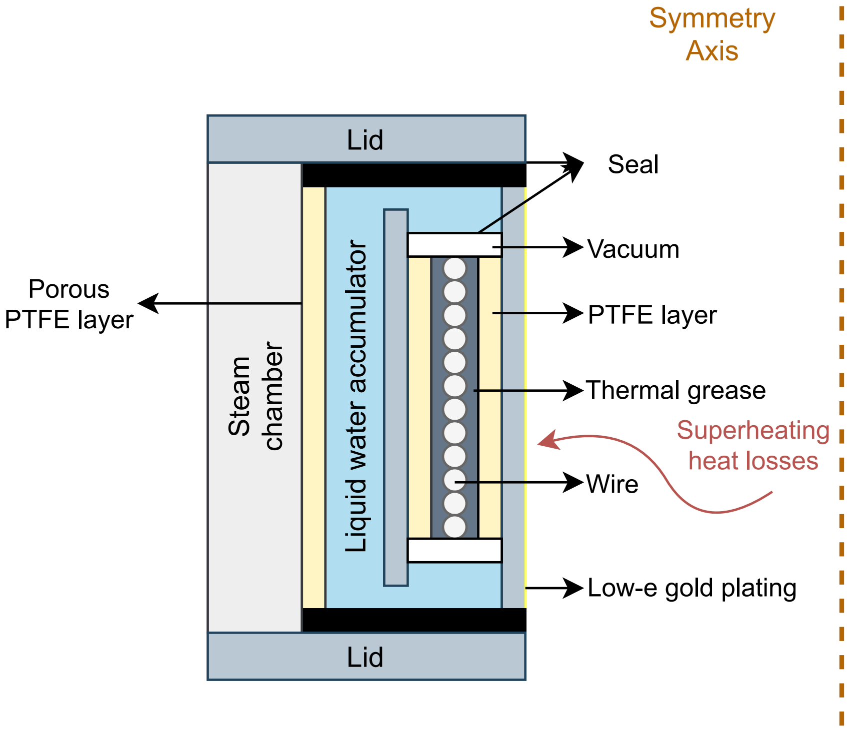

Figure 5.4.5: Evaporator's components and wire disposition

To ensure that the wire's temperature does not exceed degrading temperatures for grease and PTFE, the thermal model in figure 5.4.6 is proposed.

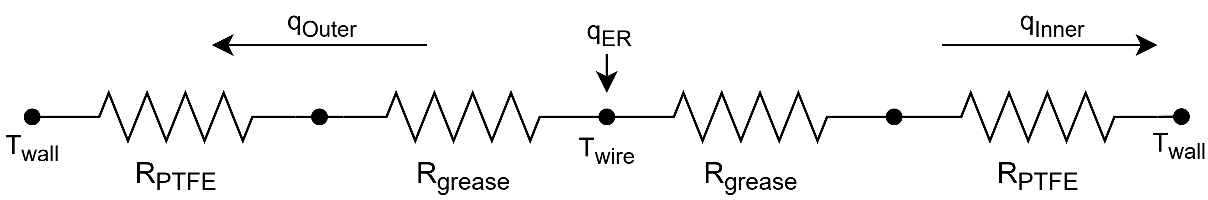

Figure 5.4.6: Thermal circuit for evaporating resistor's temperature

A linear resistance for the thermal grease R_{grease}, with the coil's inner and outer lateral area is assumed, and the PTFE resistance is a cylindrical resistance for a 1mm thickness component. If a film is used, thickness is even lower and the equal heat flux would be reached with less temperature gradient. The evaporating resistor dissipates heat $P_{wire_{superheater}}$ that is directed to the accumulator wall, at a temperature T_{wall} where the evaporation process occurs.

20% of the power and current budget is assigned to the evaporator as a first assumption. Since the superheater dimensions are assumed to be $\phi 20mmx15mm$ the wire's coil diameter is considered 30mm, having 5mm from the superheater's surface to the coil, enough to fit the accumulator and the PTFE layer. The coil's height is 20mm since the accumulator can be longer than the superheater due to the insulation connectors. Thermal conductivity for PTFE is $0.3\frac{W}{mK}$.

Wire diameters between 0.5 and 2mm of Kanthal A1 wire are proposed and for the specified height, a coil of pitch equal to the wire's diameter is proposed, and with aid of the electrical resistance submodel, the correct diameter that would result in the 2A current and 10W power consumption is chosen. The circuit is then solved for $T_{wall} = 443K$ and $P_{wire_{superheater}} = 10W$.

With the specified dimensions results for the circuit are shown in table 5.4.1. The evaporator can successfully transfer over 10W with a very low-temperature difference. This model is revisited when fine-tuning variables to make sure that the device works as intended.

Parameter	Unit	Value
$P_{wire_{superheater}}$	[W]	10
I_{ER}	[A]	2
V_{ER}	[V]	5
R_{ER}	[Ω]	2.5
d_{wire}	[mm]	1.1
l_{wire}	[m]	1.7
q_{Inner}	[W]	4.63
q_{Outer}	[W]	5.37
T_{wire}	[K]	451

Table 5.4.1: Evaporator thermal model results

5.5 Vapor Chamber

The vapor chamber is placed externally with respect to the accumulator, as is shown in figure 5.4.1. A hydrophobic PTFE 20 micron filter separates the two subsystems. The key aspect behind this filter is its hydrophobic nature of it as well as the mesh size. As described in 5.4.1, this allows the filter to act as a barrier for liquid propellant but not for steam. These types of filters are commercially available in cylindrical shapes, which fit the propulsion system's requirements perfectly.

5.6 Tank

The propellant tank is separated into three parts displayed in 5.6.1: the main storage unit and an impulse event pre-tank which can be placed anywhere in the CubeSat, and the water accumulator located surrounding the superheater, where water evaporation occurs. The impulse event pre-tank is a smaller propellant tank, which provides enough fuel for one propulsion event.

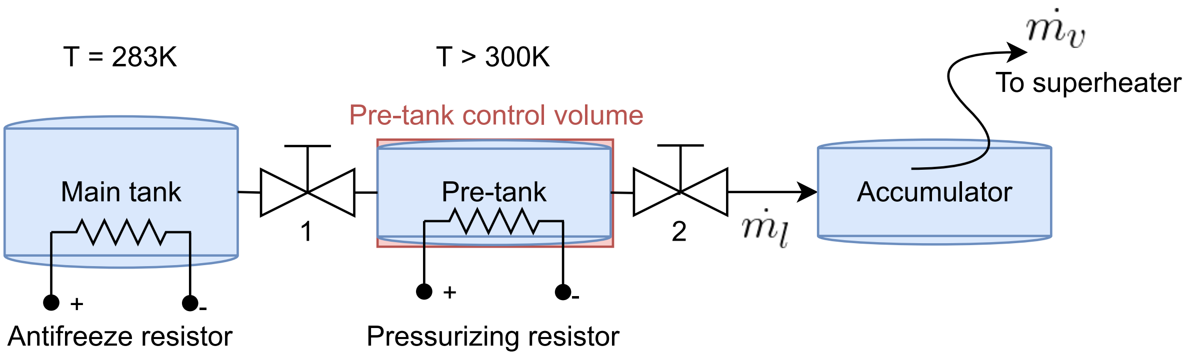

Figure 5.6.1: Main tank, pre-tank and accumulator diagram

Energy in the batteries is to be consumed heating up the pre-tank and the rest of the device, and having both of them working at steady-state. With limited battery capacity, less usage for tank startup and operation result in more energy available for propulsion.

The benefit of this separation is that the amount of propellant heated diminishes greatly, leading to a significant increase in energetic efficiency, while also decreasing the volume of a higher temperature tank and improving power conversion efficiency.

The pre-tank's capacity has to be designed so that when it is emptied, the batteries are fully discharged. If the pre-tank has excess propellant, heated fluid will remain at the tank when the batteries are emptied resulting in energy loss. When the pre-tank is too small, the impulse event ends when the fluid runs out, but energy in the batteries is still available.

Before an impulse event, the tank fills the pre-tank with valve 2 closed. With valves 1 and 2 closed, the tank reaches the pre-tank target temperature. During the impulse event valve 1 between the tank and pre-tank is closed to prevent fluid from flowing "backward", and water in the pre-tank is fed to the water accumulator opening valve 2, where the propellant is evaporated by the incoming heat from the superheater.

Both the main tank and the pre-tank must include electrical resistors to prevent freezing in case the satellite's temperature falls below 273K and to reach the design inlet conditions (pressure and temperature) respectively.

The pre-tank also uses its resistor to regulate the propellant's required temperature compensating for both heat losses of the tank and steam generation through the impulse event. Starting an impulse event, the tank is filled with water but as liquid exits the tank, steam has to be generated to maintain the temperature and the pressure required by the device at a rate $\dot{m}_g$.

When considering work done in the device, only the resistor's dissipated power P_{wire} is present. Heat dissipated by the tank walls q_{lost} is energy coming out of the system.

Strictly, the energy balance for the pre-tank is presented in equation 5.6.1. u, h and v represent internal energy, enthalpy, and velocity respectively. Subindexes v and l represent saturation vapor and liquid states.

$$P_{wire} - q_{lost} - \dot{m}\left(h_{out} + \frac{v_{out}^2}{2}\right) = \dot{m}_g\left(u_v - u_l\right) - \dot{m}u_l \tag{5.6.1}$$

However, terms with mass-flow $\dot{m}$ and steam generation rate $\dot{m}_g$ are negligible:

1. Kinetic energy for the liquid leaving is negligible as mass flow is very low and the fluid is in liquid state.

2. Difference between liquid enthalpy and internal energy is no more than $50\frac{J}{Kg}$ for water below 100°C.

3. At the last instant of the impulse event, the pre-tank is filled with steam. Compared with the initial state where that final amount of propellant is in liquid state, the internal energy difference is given by equation 5.6.2, with m_{v_f} being the final steam mass in the pre-tank. A tank temperature of 343K is assumed. To assign a volume to the pre-tank, an initial mass 1Kg of liquid water mass is considered (exceeding greatly the volume of expected pre-tanks), resulting in approximately 1 liter of volume V_{tank}.

$$\begin{aligned}\Delta H &= m_{v_f}\left(u_v - u_l\right)\\ \Delta H &= \rho_v V_{tank}\left(u_v - u_l\right) = 431J\end{aligned} \tag{5.6.2}$$

   Considering the battery has a capacity of $77Wh$ or $277200J$, the enthalpy change results negligible, therefore $\dot{m}_g$ is negligible.

As a result, heat dissipated by the wire is equal to heat losses in the pre-tank.

Design concerns in the pre-tank are therefore very simple and easy to calculate. The only requirements are propellant supply in any state (if steam travels to the accumulator it flows through the filter), and minimum heat losses for improved efficiency.

5.7 Nozzle

The nozzle is the last system to interact with the propellant before it leaves the propulsion system. To generate thrust most effectively, several aspects need to be evaluated, as shown in sections 5.7.1 to 5.7.4.

5.7.1 Micronozzle effects

When designing regular nozzles, viscous effects are ignored due to the very low surface-to-volume ratio. In micronozzles, viscous effects can no longer be ignored, because of an increased surface to volume ratio and the low Reynolds numbers expected due to low propellant pressure and mass flow [33].

While flow in the convergent region of the nozzle is in the continuum regime, as the fluid approaches outer space pressure decreases drastically.

The Knudsen number Kn describes the degree of rarefaction of the flow and is usually calculated according to equation 5.7.1 at the nozzle's throat [34]. λ is the mean free path of the gas molecule and L is the characteristic length, in this case, the nozzle's diameter. For its calculation, the ratio of specific heat γ, the Mach number Ma, and the Reynolds number Re at the throat (denoted by superscript *) are used.

$$Kn = \frac{\lambda}{L} = \sqrt{\frac{\gamma\pi}{2}}\frac{Ma^*}{Re^*} \tag{5.7.1}$$

Knudsen numbers nearing 0.1 can be found in the throat (see section 7.3.2 further below) due to the low Reynolds number of the fluid (low mass flow and low density due to low pressure), meaning that the divergent region of the nozzle is likely to have flow in the slip flow (Kn>0.1) and transition (Kn>1) regimes due to a sharp decrease in pressure. Rarefied flows and the aforecited viscous effects occur, that are studied with very complex 2-D or 3-D CFD models such as Direct Simulation Monte Carlo (DSMC), which computes the path of a statistical sample of the molecules in the flow, or a hybrid between Navier-Stokes and DSMC models. [33] Rarefied flows and viscous effects are important as they decrease the efficiency of the nozzle, a factor that is key when calculating both specific impulse and thrust.

When Knudsen numbers calculated on the throat exceed 0.01, the flow is considered rarefied due to Kn increasing as the gas expands in the nozzle, impacting the device's performance negatively as described in section 5.7.4.

5.7.2 Thermal losses

The nozzle must be as adiabatic as possible. A low thermal conductivity material allows for less heat transfer between the fluid and the nozzle since the temperature difference between the inner wall and the outer wall of the nozzle is higher. Then, heat transfer between the fluid and the inner wall is reduced, while heat losses remain low.

5.7.3 Manufacturing

The material needs to be easily manufactured as well as have a smooth inner surface to prevent friction-induced losses.

A grade 5 titanium alloy is picked as it complies with all parameters: it has a relatively low thermal conductivity as well as being an electrically conductive material, allowing it to be manufactured using EDM as shown in figure 5.7.1. EDM is an excellent method as it allows for conical nozzles with low diameters, which are not easily made by the use of cutting tools.

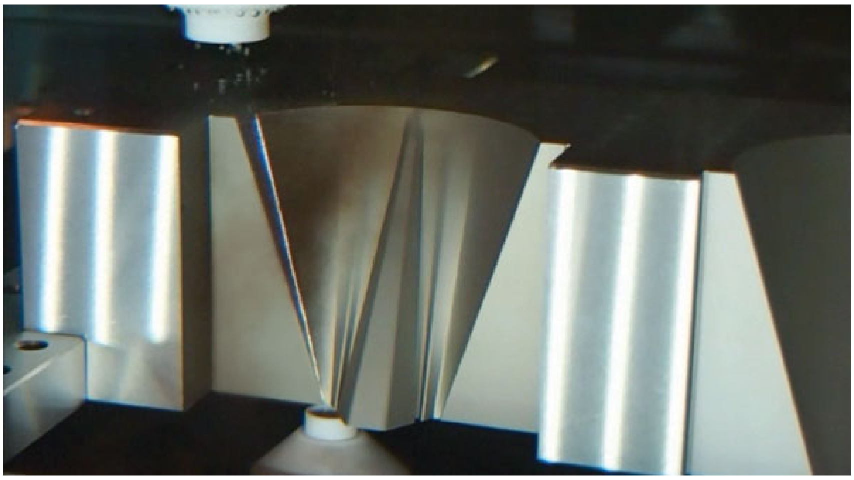

Figure 5.7.1: Wire EDM machining

By EDM manufacturing, a bore with a drill bit is made so that the cutting wire can be threaded through the hole. Then the wire is given the appropriate angle and the wire is revolved to generate the convergent and the divergent cone. Schematics for the process can be seen in figure 5.7.2.

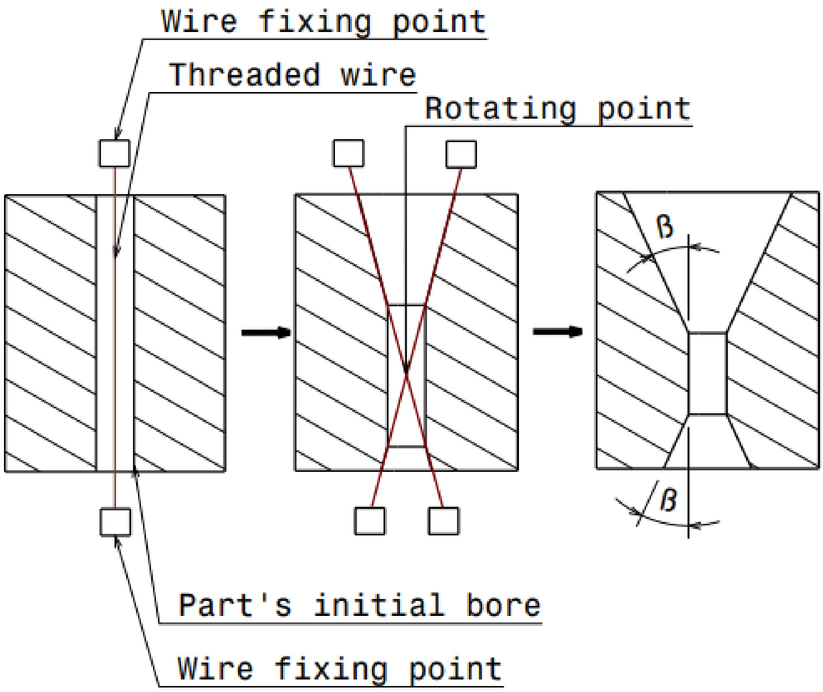

Figure 5.7.2: Wire EDM process for the nozzle

5.7.4 Dimensions

Since the nozzle is manufactured by wire EDM, the convergent and divergent sections share the same half-angle as shown above. In addition, as the cutting wire is straight, the line generating the convergent cone is coincident with the divergent cone as shown in figure 5.7.2. Therefore the nozzle's inner geometry is defined by the inlet diameter (same as the superheater ducts), the nozzle's angle and length, and the choke diameter.

Typical conical nozzles for spacecraft have a divergent half-angle of 15° but in micronozzles the optimal angle changes due to an increase in viscous losses and the rarefaction of the flow.

Extensive research on conical micronozzles has been performed by Louisos [34], LaTorre [33] and Ivanov [35] using the previously mentioned methods, which allows for the determination of the nozzle angle and expected nozzle efficiency for the nozzle's throat Reynolds number.

A 25° half-angle nozzle reaches up to 95% specific impulse efficiency when analyzed with hydrogen peroxide (H_2O_2) and without the modeling of rarefied flow. Due to the lack of data of studies with water and the similar viscosities with hydrogen peroxide (see figure 5.7.3), a half-angle of 25° is chosen for the nozzle. When rarefaction effects are taken into account a 20% drop in efficiency is expected according to Louisos, therefore a 75% specific impulse efficiency is considered for rarefied nozzles. Since no data on thrust efficiency is found, thrust is considered to be impacted by the same percentage as it depends on the exit velocity, which is denoted by I_{sp}.

It has to be taken into account that the efficiency calculated in the cited research is isentropic, therefore when calculating the thrust coefficient C_f, and because the backpressure of the nozzle is zero, an exit Mach number tending to infinity has to be used. If length was taken into account when calculating specific impulse and thrust, both variables would be penalized twice due to the same effect.

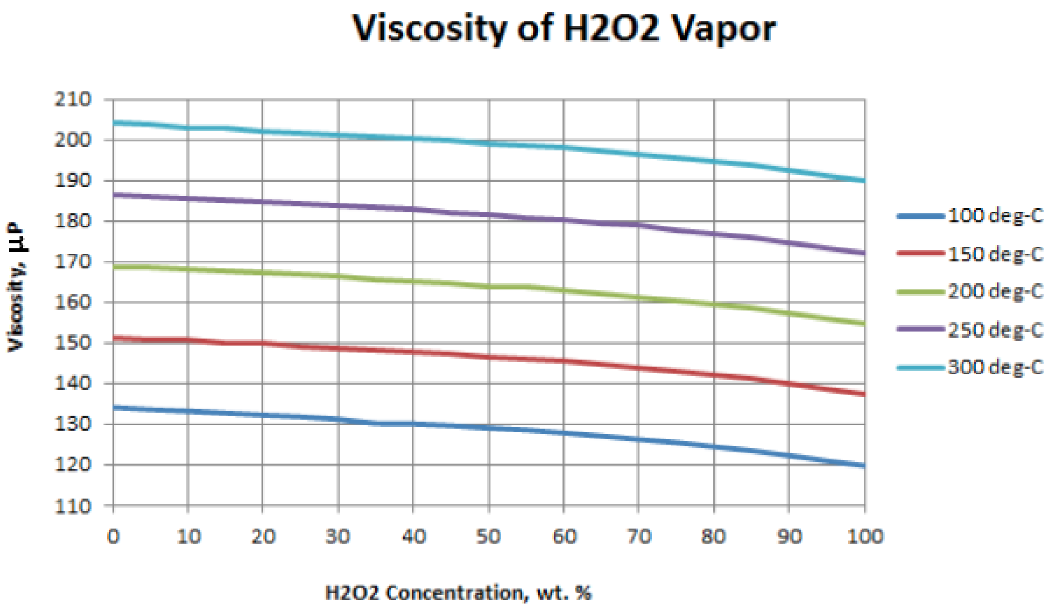

Figure 5.7.3: Viscosity for water (0% wt) and H_2O_2 (100% wt)

Equation 5.7.2 shows the ideal I_{sp} to reach the target of 200 seconds, when considering a specific impulse efficiency of 75%.

$$Isp_{ideal} = \frac{Isp_{real}}{\eta_{I_{sp}}} = \frac{200s}{0.75} = 266.7s \tag{5.7.2}$$

The nozzle inlet temperature for a 266.7s specific impulse is near 1350K according to figure 5.1.1. This is consistent with figure 5.3.2b, in which the fluid reaches more than 1375K for power conversion efficiencies lower than 80%.

As explained in section 3.1.4, the nozzle's length is limited by the fluid's exit temperature to prevent sudden sublimation during the expansion process. Checks are performed so that fluid leaving the nozzle is above the sublimation temperature.

Nozzle's choke diameter selection is explained in section 7. An upper limit for nozzle diameter is not established, but the diameter must be higher than 1mm, as it is the smallest drill bit available to drill a hole in the nozzle and thread the cutting EDM wire.

Outer dimensions for the nozzle are determined by its coupling method to the lid and also by the inner dimensions. The dimensions can be seen in figure 5.7.4.

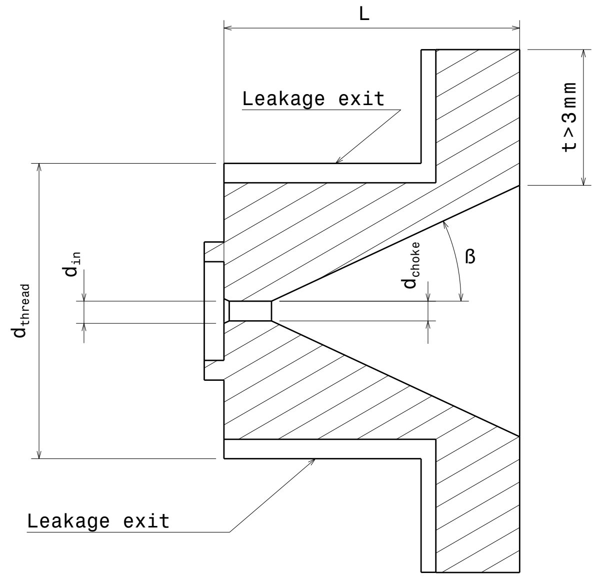

Figure 5.7.4: Nozzle dimensions diagram

5.8 Full thermal model

A summary is presented in this subsection to have an overview of the conceptual design and to determine the simulations to be performed when dimensioning the device.

First, the energy balance for the designed propulsion system is presented. Then, detail for fluid and thermal circuit simulations is given. Nozzle and electric submodels require no further explanations other than the ones given in section 4.

5.8.1 Energy balance

To analyze the full model connecting fluid, solid, and nozzle submodels, a slight modification in the selected control volume for the energy balance in section 3 is made. The pre-tank is isolated and two control volumes are generated. The full steady-state thermal model's control volume for the accumulator, evaporator, and superheater is presented in figure 5.8.1, along with wire powers entering the system, mass flowing in and out, and heat leaving the device. Limits for the control volume are depicted in the figure by the part green and part blue boundary.

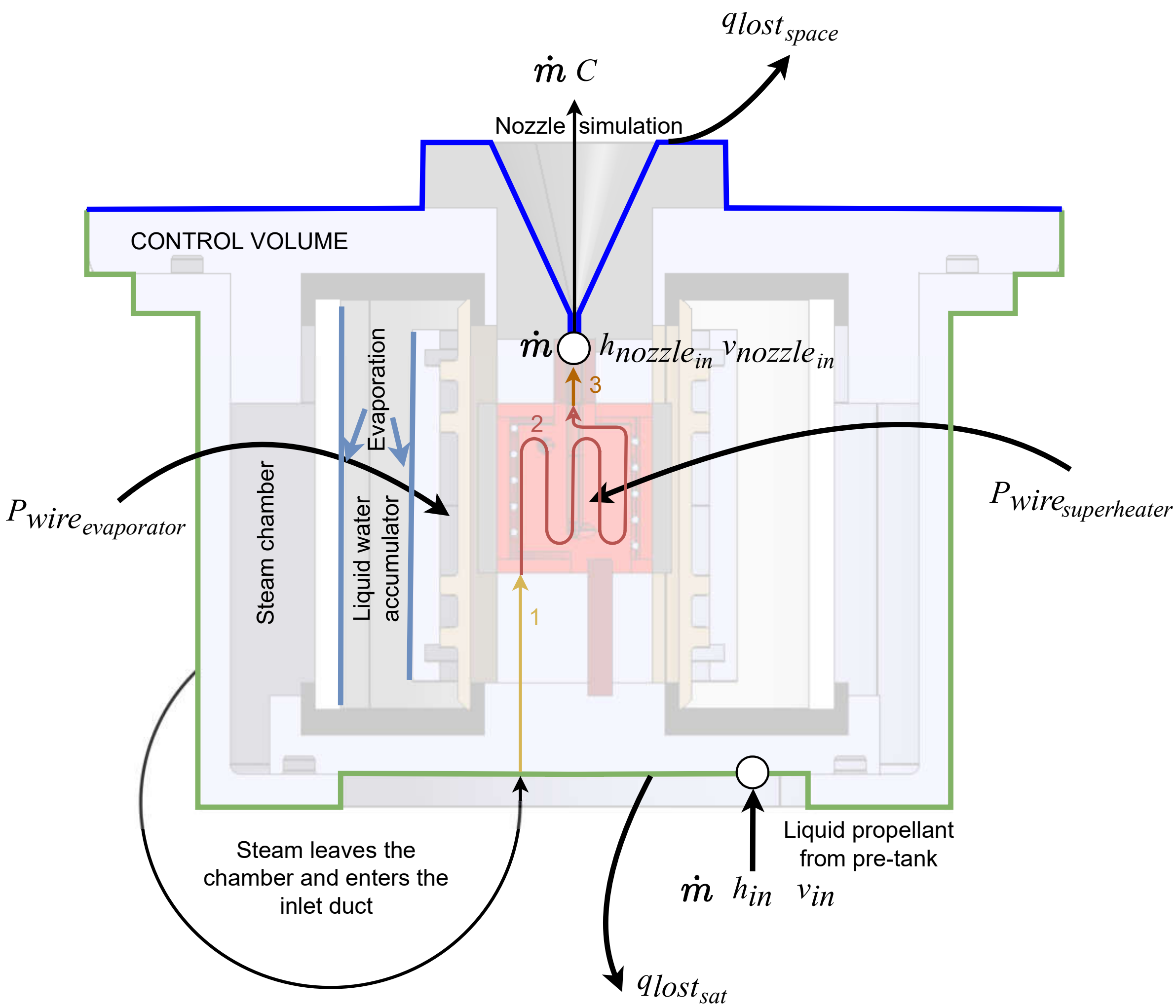

Figure 5.8.1: Detailed control volume with simulations

Energy balance for the accumulator, evaporator, and superheater is separated, according to equation 5.8.1. Mass flowing $\dot{m}$ in at a liquid state is heated and leaves the control volume as steam at a high temperature, to be discharged by the nozzle.

Power is consumed in the wires in the superheater ($P_{wire_{superheater}}$) and evaporator ($P_{wire_{evaporator}}$). Heat is lost to the interior of the satellite ($q_{lost_{sat}}$) through the surface at the blue boundary, and to outer space ($q_{lost_{space}}$) through the surface at the green boundary. Internal energy remains constant as the device is in steady-state, since the tank is outside the control volume.

$$P_{wire_{superheater}} + P_{wire_{evaporator}} - q_{lost_{sat}} - q_{lost_{space}} = \dot{m}\left[\left(h_{nozzle_{in}} + \frac{v^2_{nozzle_{in}}}{2}\right) - \left(h_{in} + \frac{v^2_{in}}{2}\right)\right] \tag{5.8.1}$$

Heat losses from the nozzle surfaces and their connection with other parts of the device are included, but the fluid discharged nozzle is analyzed separately according to the submodel in section 4.2.

Equation 5.8.2 shows the energy balance for the pre-tank, with assumptions as explained in section 5.6. The pre-tank resistor compensates for heat losses to the environment.

$$\begin{gathered} P_{wire_{pre-tank}} - q_{lost_{pre-tank}} - \dot{m}\left(h_{in} + \frac{v^2_{in}}{2}\right) = -\dot{m}u_{in} \\ P_{wire_{pre-tank}} = q_{lost_{pre-tank}} \end{gathered} \tag{5.8.2}$$

5.8.2 Fluid simulations

Three consecutive fluid simulations are performed present in figure 5.8.1, using the submodel described in section 4.1:

1. Inlet duct (yellow): fluid coming from the pre-tank suffers heat exchange in the ceramic duct connecting the inner lid to the superheater. A linear temperature profile for the solid is assumed, with temperatures of the lid and superheater nodes obtained from the thermal circuit.

2. Superheater (red): heat exchange with a duct at constant temperature.

3. Outlet duct (brown): heat exchange in the ceramic duct connecting the superheater to the nozzle. A linear temperature profile for the solid is assumed, with temperatures of the lid and nozzle nodes obtained from the thermal circuit.

5.8.3 Thermal circuit

The thermal circuit connecting fluid simulations and enabling for energy and power consumption is proposed to obtain, while the device is active but also in idle mode, the temperature field for each component as well as heat fluxes from the resistors to the inner part of the satellite and outer space.

Figure 5.8.2 shows the complete thermal circuit. The following color code is adopted:

- Blue nodes - fixed temperature nodes
- Red nodes - nodes with generated heat
- Gray resistances - radiation heat resistances
- White resistances - conductive heat resistances
- Capacitors - contact resistances
- Green arrows - Heat flowing from node to the fluid or viceversa. If the arrow points towards the node it represents heat is transferred from the fluid to the solid component

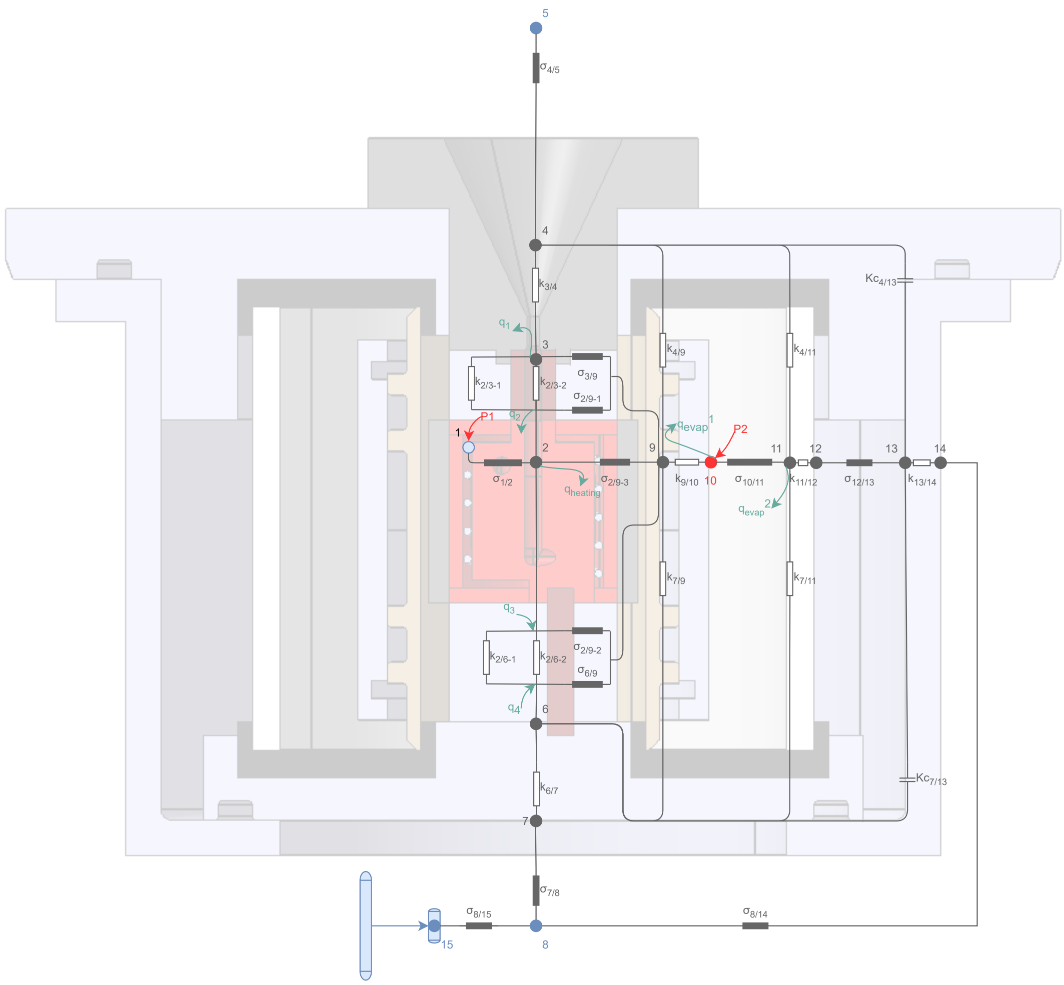

Figure 5.8.2: Thermal circuit showing heat exchange in the resistojet

Boundary conditions are the following for both active and idle mode:

- Outer surfaces (blue boundary in control volume), facing towards outer space radiate to a 0K heat source (node 5).
- Surfaces facing towards the interior of the satellite radiate to a 283K heat source (node 8). This includes the pre-tank surface, assumed as a different control volume.

- Heating wire is at a set temperature: 1670K for active mode, and 400K for idle mode to keep all components at a safe temperature (node 1).

Several hypotheses are made to simplify the thermal modeling:

- Superheater is considered to be at a uniform temperature (node 2): assuming a heat flux of 50W from the wire to the superheater, temperature gradient between the outer surface of the superheater and the heating ducts results of less than 8K.
- Heating wire is also considered a 0-D element (node 1). Superheater is at a uniform temperature and electrical heat generation is uniform, therefore axial heat flux is assumed to be negligible. Temperature at node 1 is set at 1670K, resulting in a generated heat P_1.
- View factor between the wire and superheater as displayed in section 5.3.4 (affects $\sigma_{1/2}$).
- Heat exchanged by the superheater and the fluid is considered a generated heat in the superheater node ($q_{heating}$).
- Heat exchanged by other ducts and the fluid is added as a generated heat in nodes at the duct ends. Heat is split in half for each node (q_1, q_2, q_3 and q_4).
- View factor between the superheater and the accumulator's surface is equal to 1 due to the proximity of the surfaces (calculation of $\sigma_{2/9-3}$).
- View factor between the ceramic insulations (both inlet and outlet) and the accumulator's surface is equal to 1 due to the proximity of the surfaces (calculation of $\sigma_{2/9-1}$ $\sigma_{3/9}$, $\sigma_{2/9-2}$ $\sigma_{6/9}$).
- Radiation heat from the insulations is calculated as a surface at an equivalent temperature as seen in equation 5.8.3, for a duct with nodes i and j at its ends. The temperature field is assumed linear in the insulator (calculation of $\sigma_{2/9-1}$ $\sigma_{3/9}$, $\sigma_{2/9-2}$ $\sigma_{6/9}$).

$$\begin{aligned} T_{eq} &= \frac{1}{L}\left(\int_0^L T(x)^4 dx\right)^{0.25} \\ T(x) &= T_i + \left(\frac{T_j - Ti}{L}\right) x \end{aligned} \tag{5.8.3}$$

- Heat radiated from the insulators is split in half and assigned to nodes at its ends, analog to the heat exchanged by the fluid in the ducts (calculation of $\sigma_{2/9-1}$ $\sigma_{3/9}$, $\sigma_{2/9-2}$ $\sigma_{6/9}$).
- Evaporating resistor's heat is added as generated heat to the accumulator's wall node (P_2 in node 10).
- Heat flux from evaporation is imposed by the mass flow obtained from the fluid submodel, and split between the filter and the accumulator's wall (nodes 10 and 11 respectively) according to the temperature difference, as seen in equations 5.8.4 to 5.8.6.

$$q_{evap} = \dot{m} \cdot h_{evaporation} = q_{evap_1} + q_{evap_2} \tag{5.8.4}$$

$$\begin{aligned} q_{evap_1} &= f_1 \cdot q_{evap} \\ q_{evap_2} &= f_2 \cdot q_{evap} \end{aligned} \tag{5.8.5}$$

$$\begin{aligned} f_1 &= \frac{T_{cage} - T_{liquid}}{(T_{cage} - T_{liquid}) + (T_{filter} - T_{liquid})} \\ f_2 &= \frac{T_{filter} - T_{liquid}}{(T_{cage} - T_{liquid}) + (T_{filter} - T_{liquid})} \end{aligned} \tag{5.8.6}$$

This evaporation modeling is necessary as the critical heat flux curve for nucleate pool boiling in space is yet to be determined. Otherwise, heat flux as a function of liquid temperature and wall temperature could be found. Evaporating resistor's heat needs to be varied to find temperature fields that cover the entire range of possible evaporation: near 0K of temperature difference up to the 100K difference limit, as described previously in section 5.4.

- The lids and the components engulfing the steam chamber (exterior shell) are at a uniform temperature due to aluminum's high thermal conductivity.
- The nozzle is considered at the same temperature as the outer lid.
- Lids and the exterior shell are connected through contact resistances of $3 \cdot 10^{-5} \frac{W}{m^2K}$ according to data for low contact pressure, clean aluminum parts [6] (calculation of $Kc_{4/13}$, $Kc_{6/13}$, .

Table 5.8.1 summarizes the differences between active cases 1, 2 and idle mode for the thermal circuit.

Mode	Active		Idle
Case	1	2	
Fluid heat exchange	Enabled		Disabled
Tank heating	Enabled		Disabled
$T_{wire_{superheater}}$	1670K		400K
$P_{wire_{evaporator}}$	Enabled		Disabled
$max(T_{10}, T_{11}) - T_{15}$	100K	10K	-
σ_{10-11}	Disabled		Enabled

Table 5.8.1: Simulation parameters comparison between active and idle models

5.8.4 Efficiency calculation

Once the final control volume is defined and the thermal circuit is explained, equations for efficiencies in section 4 can be written.

To simplify, all wire powers (pre-tank, evaporator and superheater) are summed into one variable P_{wires}, and all heat lost is summed into q_{lost}.

Equation 5.8.7 shows the power conversion efficiency, which is the ratio of the enthalpy flow difference between the device's inlet and the nozzle inlet, and the used power in the resistors. It measures how much of the used power ends up heating the propellant.

$$\eta_{power} = \frac{\dot{m}\left[\left(h_{in_{nozzle}} + \frac{v_{in_{nozzle}}^2}{2}\right) - \left(h_{in} + \frac{v_{in}^2}{2}\right)\right]}{P_{wires}}$$
$$\eta_{power} = \frac{P_{wire_{superheater}} + P_{wire_{evaporator}} - q_{lost_{sat}} - q_{lost_{space}}}{P_{wires}} \quad (5.8.7)$$

Equation 5.8.8 represents how energy is consumed after a full discharge of the battery. The energy accumulated in the batteries is absorbed by the components until they reach their working temperatures ($E_{startup}$), and leaves the system as as an enthalpy gain by the fluid (E_{fluid}) or as heat losses (E_{lost}) that can be divided in warmup and operation losses.

$$E_{batteries} = E_{startup} + E_{fluid} + E_{lost_{warmup}} + E_{lost_{operation}} \quad (5.8.8)$$

Heat losses during operation are known, and therefore energy losses during operation are calculated by multiplying the heat losses $q_{lost_{sat}}$ and $q_{lost_{space}}$, and the impulse event duration $t_{operation}$. As no transient model is analyzed, losses during warmup are overestimated as equal to heat losses as steady-state. Assuming that during warmup heat losses are the same as in normal operating conditions, a warmup time t_{warmup} can be calculated according to equation 5.8.9. The power used by the wires is also assumed to be equal to operation power.

$$t_{warmup} = \frac{E_{startup}}{P_{wires} - q_{lost_{sat}} - q_{lost_{space}} - q_{lost_{pre-tank}}} \quad (5.8.9)$$

The energy lost during warmup results in the multiplication of the warmup time and the wire power, and the energy balance from equation 5.8.8 is simplified to 5.8.10.

$$E_{batteries} = P_{wires}\left(t_{operation} + t_{warmup}\right) \quad (5.8.10)$$

From 5.8.10 operation time $t_{operation}$ can be obtained as shown in equation 5.8.11.

$$t_{operation} = \frac{E_{batteries}}{P_{wires}} - t_{warmup} \quad (5.8.11)$$

Energetic efficiency can be calculated according to equation 5.8.12, and represents how much energy is used to heat up the fluid, in comparison with the total used efficiency.

$$\eta_{energy} = \frac{E_{fluid}}{E_{batteries}} = \frac{\dot{m}\left[\left(h_{in_{nozzle}} + \frac{v_{in_{nozzle}}^2}{2}\right) - \left(h_{in} + \frac{v_{in}^2}{2}\right)\right] t_{operation}}{E_{batteries}}$$
$$\eta_{energy} = \frac{E_{fluid}}{E_{batteries}} = \frac{\dot{m}\left[\left(h_{in_{nozzle}} + \frac{v_{in_{nozzle}}^2}{2}\right) - \left(h_{in} + \frac{v_{in}^2}{2}\right)\right] t_{operation}}{P_{wires}\left(t_{operation} + t_{warmup}\right)} \tag{5.8.12}$$
$$\eta_{energy} = \eta_{power}\left(\frac{t_{operation}}{t_{operation} + t_{warmup}}\right)$$

If warmup and operation times are expressed in terms of energies and powers, energetic efficiency results as shown in equation 5.8.13.

$$\eta_{energy} = \eta_{power}\left(1 - \frac{E_{startup}}{E_{batteries}}\frac{P_{wires}}{P_{wires} - q_{lost}}\right) \tag{5.8.13}$$

Equation 5.8.12 shows that by reducing startup energy and heat losses, energetic efficiency can improve, with the power conversion efficiency as its upper boundary.

Since the superheater is the hottest element in the device and most of its lost heat needs to be recovered, heat recovery efficiency $\eta_{recovery}$ is the percentage of the heat leaving the superheater that is not ultimately lost by the device. This can be calculated as the amount of heat leaving the superheater that is used to evaporate, versus heat leaving the superheater. It is determined by equation 5.8.14.

$$\eta_{recovery} = \frac{q_{evap_1} + q_{evap_2} - P_{wire_{evaporator}}}{P_{wire_{superheater}} - q_{heating}} \tag{5.8.14}$$

Since no heat is gained by the boundary conditions, contribution from the superheater to evaporation is the difference between heat required to evaporate and power dissipated by the evaporator wire. The superheater receives heat from the superheating's resistor, with heat then either leaving the superheater by raising the fluid's temperature, or transferring heat through/to other components. Heat lost by the superheater can then be expressed as the difference between the resistor's heat and heat exchange with the fluid in the superheater $q_{heating}$.

Calculating these three efficiencies allow for a quick analysis of heat fluxes, and better understanding of where designs need to be improved in the thermal aspect.

6 Design iterations

An iterative approach is used to achieve a final design, analyzing the strengths and weaknesses of each iteration before a redesign is made.

6.1 Iteration 1

The first layout is shown in figure 6.1.1, where a spiraled superheater in red, and an evaporator in blue that encloses the high-temperature components are shown. The strength of this iteration is the space-saving approach, in addition to the usage of the superheater's radiation to evaporate the needed mass flow. However, this model does not contemplate the necessary durability to withstand vibrations during liftoff. Furthermore, it is extremely challenging to manufacture this superheater with a perfectly centered wire.

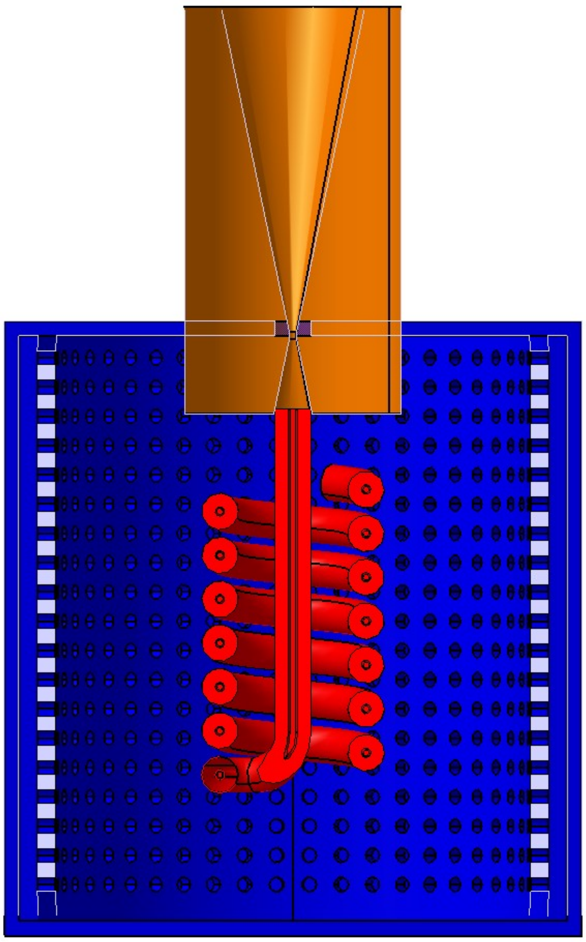

Figure 6.1.1: Iteration 1

6.2 Iteration 2

The vibration problem is dealt with by modifying the superheater and giving it more fixing points: several disks are stacked one on top of the other with a canal machined into them as shown in figure 6.2.2. The complete set is shown in figure 6.2.1. Even though this version provides a solution for the durability needed for take-off, it does not solve the hot fixing points. Also, the volume of the superheater is not a well-taken advantage of, a better design would have a higher channel density.

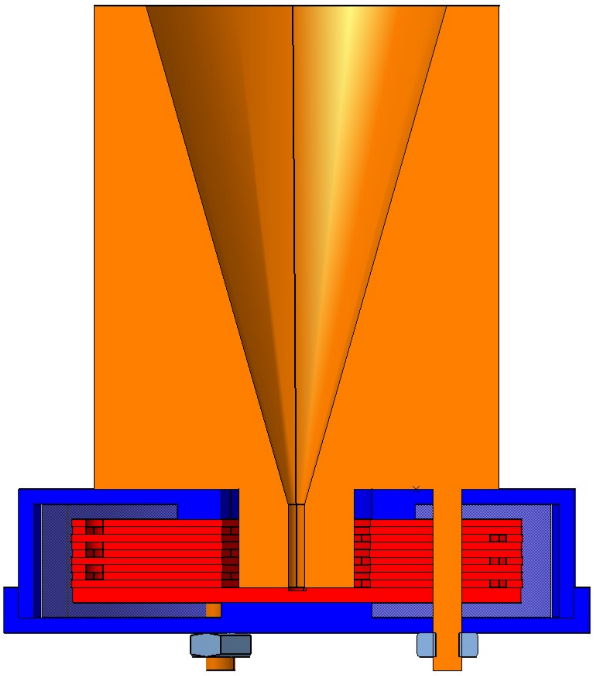

Figure 6.2.1: Iteration 2

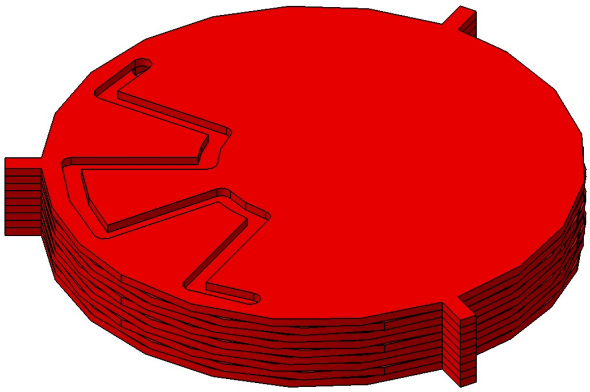

Figure 6.2.2: Detail of a superheater's disk

6.3 Iteration 3

This layout is shown in figure 6.3.1, where the tank connection is shown as well as a steam valve that separates the evaporator from the superheater. This design provides a simpler joint between the two shells, using only a thread to join the whole propulsion system. In this version, superheating and evaporation are almost completely separated. Flaws in this design include a low re-utilization of the lost heat from the superheater to evaporate, as well as unnecessary use of volume, including a long connecting element between the superheater and the nozzle where fluid loses temperature.

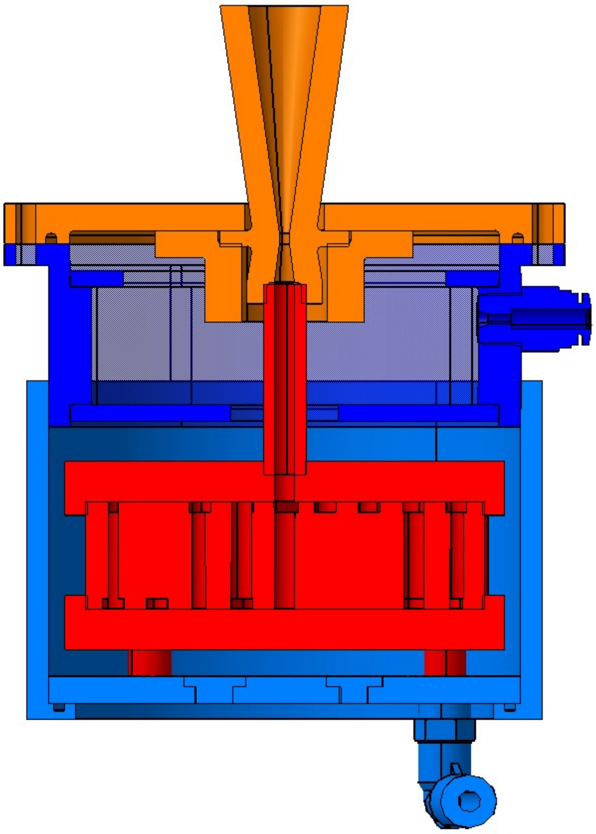

Figure 6.3.1: Preliminary version - Iteration 3

6.4 Final Design

Taking into account the considerations previously described the final design is conceived, reaching a simple yet elegant design. Sealing rings are implemented between the inner lid and the exterior shell, and between the exterior shell and the outer lid. The superheater is almost completely engulfed by the evaporation zone, allowing for a more efficient design. Also, the separation between the superheater exit and nozzle inlet is reduced, allowing for low fluid temperature losses. A threaded connection is chosen between the outer lid and the exterior shell allowing for a simple assembly.

An exploded view of the Resistojet is shown in 6.4.1, further detailed below.

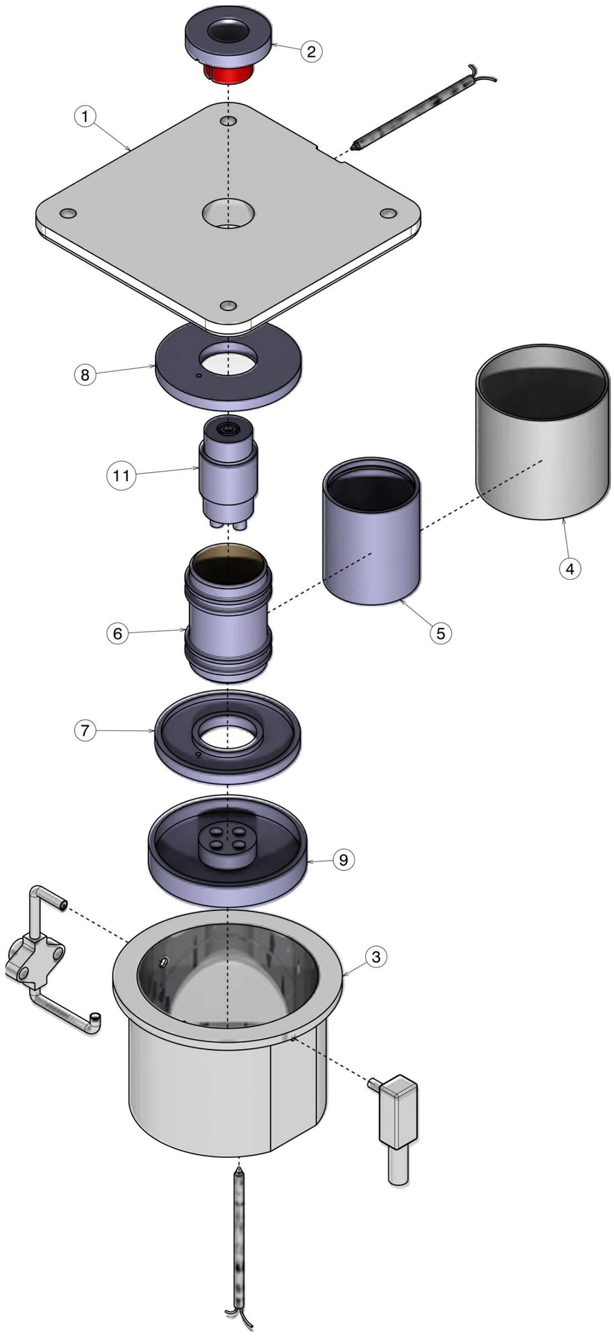

Figure 6.4.1: Exploded view of the final design

6.4.1 Nozzle set

This set is shown as components (1) and (2) shown in figure 6.4.1. This set is exposed to outer space as well as providing the fixing points of the propulsion system to the CubeSat. It provides the fixing points of the propulsion system to the CubeSat. Most of its surface radiates to outer space.

a. Outer Lid

The lid's thickness is considered to provide stiffness for the fixing points. It is made from aluminum due to the moderate temperatures it is subjected to. Component (1) in 6.4.1 shows this lid. It contains threaded connections for the nozzle and the lower case. Its surface-facing outer space requires polishing to reach an emissivity of 0.3 [36].

b. Nozzle

Its material and manufacturing process are discussed in section 5.7. It is shown in component (2) in figure 6.4.1. A threaded connection links the nozzle with the outer lid.

6.4.2 Lower case

This set contains both the evaporator and the superheater. It is made up of components (3) - (10) shown in 6.4.1. It also provides the inlet for both power and water.

a. Filter

The filter's function is to hold a thin layer of water thanks to its superficial tension properties, exposing it to the evaporating resistor. The filter, shown as component (4) in 6.4.1, is a commercially available hydrophobic filter such as the ones found in [37]. This filter is made from Teflon, a material that serves all mechanical and hydrophobic required parameters.

b. Evaporator's resistor

This resistor is used as a complementary heating element to achieve the necessary evaporated mass flow. It is shown as component (10) in figure 6.4.1 as a nichrome helix.

c. Superheater cage

The purpose of the superheater cage is not only to serve as thermal insulation for the superheater as its internal surface contains a specially reflective treatment discussed previously. Furthermore, this piece contains the evaporating resistor and the sealing o-rings to avoid water from being in contact with the resistor. This piece is shown as component (5) in figure 6.4.1.

d. Casing

This casing contains the evaporating resistor between the water reservoir and the thermal insulation of the superheater explained previously. It is fabricated from aluminum, containing grooves for sealing o-rings and gaskets shown as components (6) in figure 6.4.1.

e. Inner Lid

This lid provides closure for the prototype, made from aluminum like all the other outer components. It is also a positioning element due to the machined recesses where the superheater's thermal separators fit. A similar approach is taken with the filter. Most of the sensors described in section 6.5, as well as the flow valve (6.4.2) are mounted on this lid. This is shown as component (9) in 6.4.1.

f. Sealing rings

   The sealing rings shown as components (7) and (8) in figure 6.4.1 further improve the waterproofing of the different components of the propulsion system.

g. Valve

   An NW08 AST valve is chosen as the one shown in figure 6.4.2 [38]. This valve works for low pressure, low mass flow gases for space applications. Even though this is a solenoid valve with a full opening at 36V, due to smaller flows than the nominal flow for this valve, with a 10V bus, enough valve aperture can be obtained for the working flow can be achieved.

Figure 6.4.2: NW08 AST valve

6.4.3 Superheater set

The core of the propulsion system; this set is in charge of heating vapor as well as evaporating a fraction of the necessary mass flow. These components are shown in figure 6.4.3.

a. Core superheater

   The core superheater is shown as component (16) in figure 6.4.3. made from synthesized ceramic, it contains inner conduct of the needed length and diameter to ensure that the mass flow reached the nozzle at the highest possible temperature.

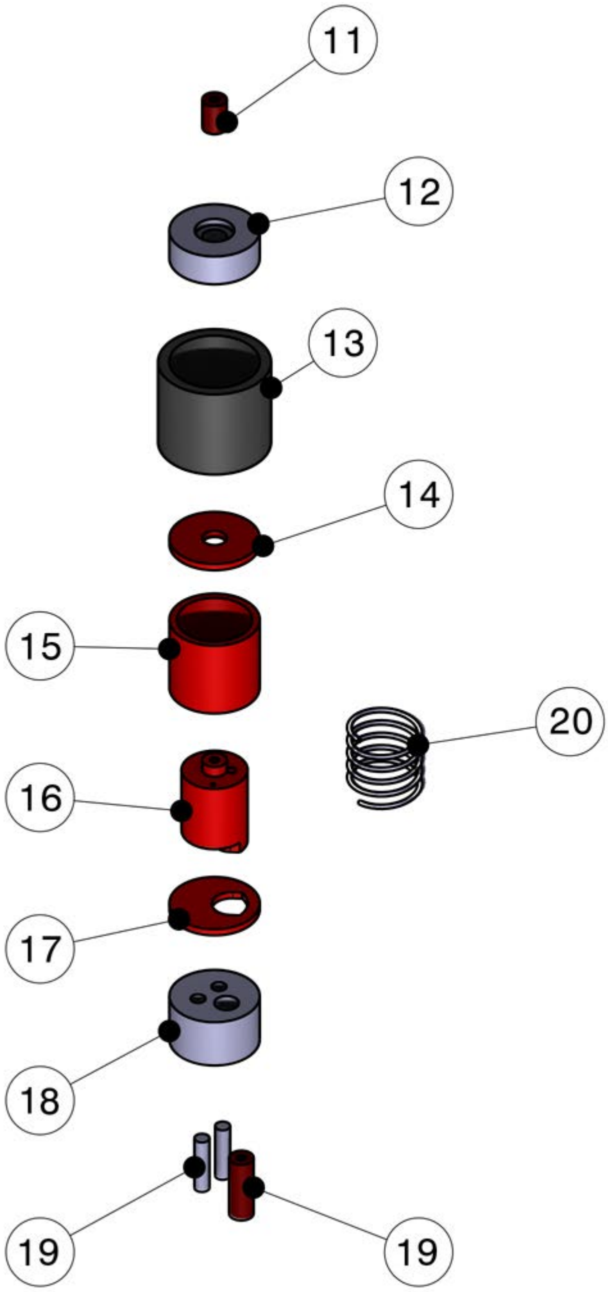

Figure 6.4.3: Exploded view of the superheater

b. Low conductivity insulation

Structural pieces are separated from nonstructural pieces, using a low conductivity, low strength ceramic for the latest, and the opposite for the structural pieces. Low conductivity insulation pieces are shown as components (12) and (18) in figure 6.4.3.

c. Normal conductivity insulation

As described previously, the normal conductivity structural parts of the superheater are shown as components (11), (13) - (17), and (19) in figure 6.4.3.

d. Superheater resistor

The heating resistor is shown as component (20) in figure 6.4.3, where it enters from one of the four legs and exits from another. One of the other three legs serves as the steam inlet, while the other serves as a temperature probe housing.

6.5 Sensors

A series of sensors are used to monitor and control the process. 2 NPT ceramic thermistors [39] are used to measure the tank temperature and the exterior shell temperature. Further explanation as to how the sensors are used in the control is shown in section 9.

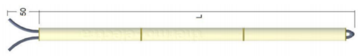

Figure 6.5.1: Temperature sensor

7 Device dimensionining

After a thorough analysis, a conceptual design of the propulsion system is achieved and the full model to be analyzed is described. More detail is required in terms of parameters as the tank temperature or dimensions of the involved components such as the nozzle, the superheater, and the insulating ceramics. Up until now, a target fluid temperature has been set, and preliminary dimensions for the superheater and the heating wire were determined to reach the desired temperature, but can be changed if needed.

Using the design process shown in section 4, with the model described in section 5.8, dimensions in components from section 6 are changed and their impact on the device performance is analyzed by looking at the most important variables: specific impulse, power conversion efficiency, and energetic efficiency.

Decisions to change or maintain dimensions across designs are explained in section 7.1, with the sweeping method explained in section 7.2. Results from the variable-sweep changes are explained in section 7.3, having the final dimensions chosen for the device, along with its performance in section 8.

7.1 Constrained dimensions and swept variables

As it can be seen in section 6, the propulsion system has a considerable number of components, each with its respective multiple dimensions. Changes in dimensions can heavily change either the thermal circuit of the fluid heating simulation, resulting in different temperatures for both solids and fluids, and therefore varying performances for different designs. To simplify the iterative designing process many of these dimensions are kept fixed through the design iterations and a minimum number of variables are adjusted to achieve a design that meets the specifications in table 3.2.4, keeping in mind that a balance needs to be found between the following restrictions:

- Specific impulse: above 200s if possible, maximized if 200s are not reachable.
- Power: below the 50W budget.
- Power conversion efficiency: maximize.
- Controllability: Temperatures for both the water accumulator's wall and the PTFE filter are required to be between 0 and 100K above the tank temperature with different evaporating resistor powers, but temperature difference near zero should be achieved with active heating.
- Bus limitations: voltage and current need to be below 6V and 10.4A (total) respectively.

As all the restrictions are affected by the high temperature of the superheater, its dimensions vary across all the designs. When changing duct diameter and length, the superheater's outer diameter and length change. The superheater diameter and duct length are subject to change, but thicknesses are kept fixed as they only affect the energy consumption. However, these thicknesses are minimized. The superheater's diameter must be greater than the nozzle's, otherwise, a Mach number above 0.5 is reached in the ducts.

Insulation is heavily involved in the thermal circuit and fluid simulation, therefore length for both insulations are variable. The inner diameter for the high insulator changes with the superheater's duct diameter, while its thickness is fixed. The low conductivity insulator's diameter is equal to the superheater's.

The water accumulator has a length equal to the length's sum of the outlet insulation, inlet insulation, and the superheater. The radiation heat from the superheater is heavily influenced by this dimension. To reduce radiation and make the device more controllable the accumulator is as close to the superheater as possible, keeping in mind that enough space needs to be left to thread the nozzle into the outer lid without clashing.

The thermal and fluid simulation is not sensitive to changes in thickness in metallic parts such as the lids, the exterior shell, and the accumulator's walls, as aluminum is a highly conductive material. Thickness is fixed for every design, considering the manufacturability of the components. However, exposed areas change with their lengths and diameters. The exterior lid is a 100mm x 100mm square as it's the fixing point to the CubeSat and is designed to take up 1U. Other dimensions such as the exterior shell outer diameter and length are determined to be as compact as possible, reducing heat losses, startup energy, and weight.

To make the device as compact as possible, spacing between concentric elements remains constant, and all their dimensions change according to the superheater's diameter. Spacing is as minimum as allowed by assembly and manufacturing concerns.

The nozzle diameter is variable within the designs, starting from a minimum of 1mm with a step of .25mm to allow for easy wire EDM manufacturing. Nozzle's length is maximized limited by the propellant's sublimation. The nozzle's thread diameter is the same as the superheater's diameter, and the thread's length is determined so that when the nozzle is fully threaded and preloaded with the outer lid, the gap between the lid's thread and the insulator is very small (<1mm). The nozzle's thickness at the exit diameter is 3mm. By changing the superheater's duct diameter, the throat's diameter and the nozzle's length change, and the nozzle is therefore completely defined.

The superheating wire's length and diameter are very important as they determine the heat exchange area between the superheater and the wire. Temperatures in the device mostly depend on the heat exchange area, but by regulating length and diameter both thermal and electrical requirements can be met. Also if the heat exchange area remains constant, length and diameter can be adjusted with almost no changes to the thermal results. Since the superheater dimensions are fixed when a duct length and diameter are chosen, the wire's length is regulated by the pitch between two spires.

Figure 7.1.1 shows the fixed dimensions in red, while green dimensions are changed to optimize performance.

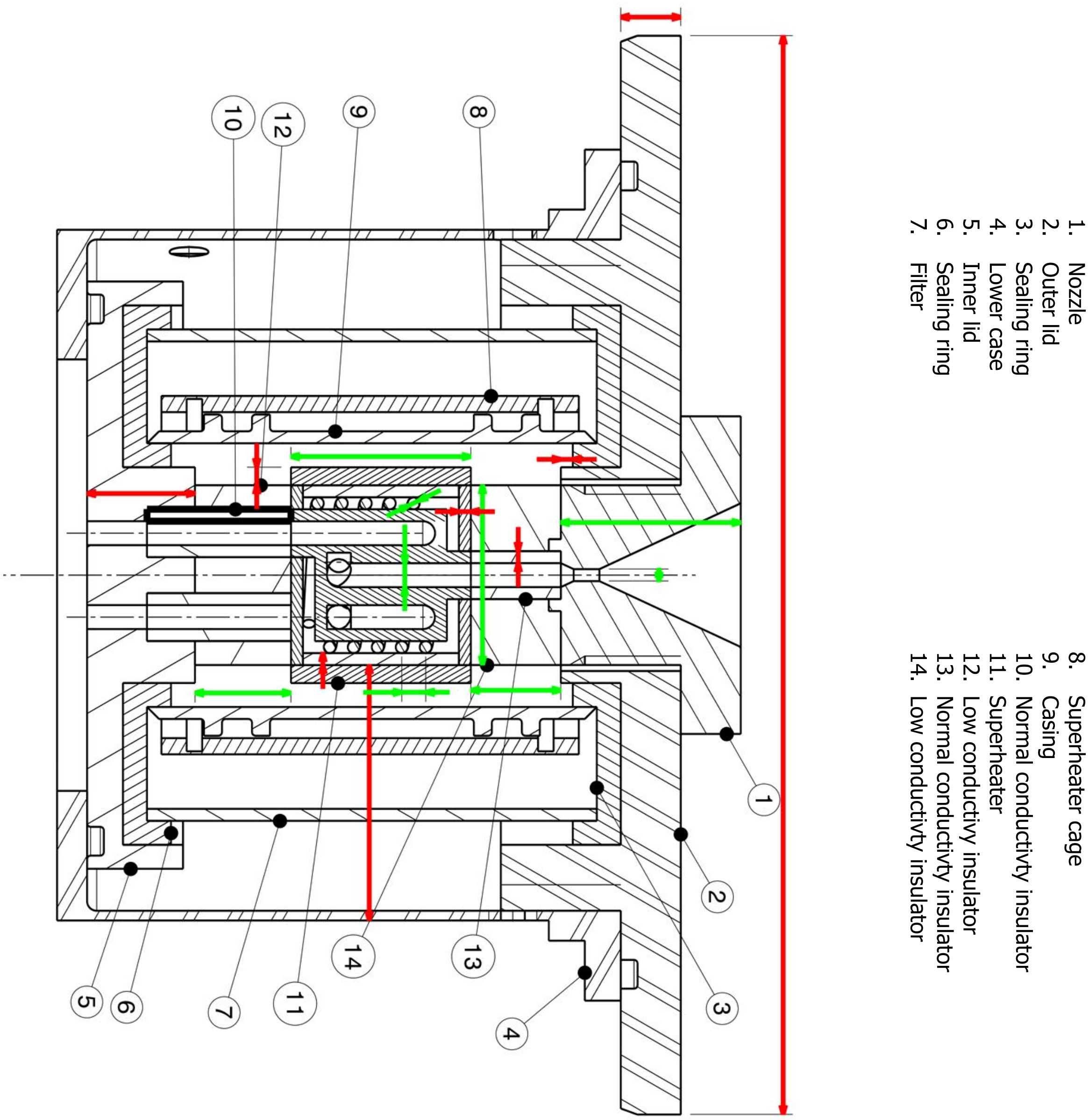

Figure 7.1.1: Section view of the superheater

In addition to component dimensions, thermodynamic variables also affect the device's performance. Regarding the fluid, the only controllable variables are inlet pressure and temperature. Since the tank is self-pressurizing, only the tank temperature is swept. A higher tank temperature and pressure have a direct impact on the amount of mass flowing through the system, and on its final temperature and specific impulse.

The last swept variable is the heat provided to the system by the evaporating resistor. It has been mentioned in section 3.1.2 that this component is a control element to provide the superheater with an adequate mass flow.

In summarizing, 9 variables are changed so that all the restrictions previously listed are met:

a. Nozzle diameter

b. Superheater's duct length

c. Superheater's duct diameter

d. Outlet insulation length

e. Inlet insulation length

f. Tank temperature

g. Superheating wire length

h. Superheating wire diameter

i. Evaporating resistor heat

Table 7.1.1 shows all chosen variables and how they impact each of the restrictions. By observing the results of a complete simulation, these variables can be adjusted to meet the requirements and reach a propulsion system with a high specific impulse while maintaining adequate power and energetic efficiencies. When fine-tuning, changing values for a variable can result in a requirement (i.e. specific impulse) passing from unfulfilled to fulfilled at the expense of failing to fulfill other requirements.

Section 7.2 describes the chosen approach to sweep across the 9 variables in an orderly and effective way.

		Specific impulse	Power	Power conversion efficiency	Controllability	Bus limitations
Nozzle diameter	+	Decreases. Increased mass flow causes reduced temperature jump in the superheater	Increases. Increased mass flow lowers superheater temperature, enabling more heat exchange	Decreases. Bigger superheater, more heat lost to evaporation.	Decreases. Bigger superheater, more heat lost to evaporation.	Increases both current and voltage due to increased power
	-	Increases	Decreases	Increases	Increases	Decreases both current and voltage
Superheater's duct length	+	Increases (more heat exchange area)	Increases. More heat exchange area for wire to heat superheater.	Decreases. Bigger superheater, more heat lost to evaporation.	Decreases. Bigger superheater, more heat lost to evaporation.	Increases both current and voltage due to increased power
	-	Decreases	Decreases.	Increases	Increases	Decreases both current and voltage
Superheater's duct diameter	+	Not connected	Increases (see superheater's duct length)	Decreases. Bigger superheater, more heat lost to evaporation.	Decreases. Bigger superheater, more heat lost to evaporation.	Increases both current and voltage due to increased power
	-	Not connected	Decreases (see superheater's duct length)	Increases	Increases.	Decreases both current and voltage
Outlet insulation length	+	Decreases. Increased area for heat transfer between hot fluid and cold walls.	Decreases. Higher insulation increases superheater temperature and decreases heat exchange between wire and superheater	Unknown. Radiation surface is increased, but conduction losses decrease.	Decreased. Surface area receiving radiation from the superheater increases.	Decreases both current and voltage due to decreased power
	-	Increases	Increases	Unknown.	Increases.	Increases both current and voltage
Inlet insulation length	+	Increases. Increased area for heat transfer between cold fluid and hot walls.	Decreases (see outlet insulation length)	Unknown. Radiation surface is increased, but conduction losses decrease.	Decreased. Surface area receiving radiation from the superheater increases.	Decreases both current and voltage due to decreased power
	-	Decreases	Increases (see outlet insulation length)	Unknown.	Increases.	Increases both current and voltage
Superheating wire diameter	+	Increases. Higher temperature in the superheater due to increased area for heat transfer between wire and superheater.	Increases. Increased heat transfer area	Unknown. More heat losses with hotter superheater but total heat exchanged also increases.	Decreases. Higher temperature in the superheater increases evaporation.	More current, less voltage
	-	Decreases	Decreases.	Unknown.	Increases	Less current, more voltage
Superheating wire length	+	Increases (see superheating wire diameter)	Increases. Increased heat transfer area	Unknown (see superheating wire diameter)	Decreases (see superheating wire diameter)	Less current, more voltage
	-	Decreases (see superheating wire diameter)	Decreases.	Unknown (see superheating wire diameter)	Increases (see superheating wire diameter)	More current, less voltage
Tank temperature	+	Decreases. Increased mass flow causes reduced temperature jump in the superheater	Increases. Increased mass flow lowers superheater temperature, enabling more heat exchange	Increases. Lower superheater temperature reduces heat losses	Increases. Higher backpressure increases mass flow, and total heat needed for evaporation	Increases both current and voltage due to increased power
	-	Increases.	Decreases	Decreases.	Decreases.	Decreases both current and voltage
Evaporating resistor heat	+	Unknown	Increases	Decreases. Less heat from superheating is used to evaporate	Increasing it does not affect controllability itself. Evaporating resistor's heat is tuned for each design to be controllable.	Increases current
	-	Unknown	Decreases	Increases.	Decreasing it does not affect controllability itself (see row above)	Decreases current

Table 7.1.1: Swept variables for iterations and their impact on the device restrictions.

7.2 Variable sweeping method

Due to the complexity of the calculation process and its great amount of results, the iterative process in which the remaining dimensions and operating points of the device are determined is manual.

Initially, a superheater's duct length l_{sh}, the superheater's duct diameter d_{sh}, the nozzle's diameter d^* and the tank's temperature T_{tank} are chosen, and different combination of evaporating resistor's heat $P_{wire_{superheater}}$, inner and outer insulation lengths l_{ii} and l_{io}, and wire diameter d_w and length l_w are simulated and evaluated.

Then, l_{sh}, d_{sh}, and d^* remain fixed, but T_{tank} is changed, to find new values of $P_{wire_{superheater}}$, l_{ii}, l_{io}, d_w and l_w.

After runs for different tank temperatures are found, d^* is changed and swept across T_{tank}, and the rest of the variables are found again.

The superheater duct's diameter d_{sh} is swept afterward, with the superheater duct's length l_{sh} being the last variable to be swept.

Performing the sweeps in order allows for the finding of trends, that indicate the range in which the variables have to be swept, including values that are quasi-fixed.

Section 7.3 shows the simulation results for the full model, and a selected design.

7.3 Variable sweeping observations

Having set preliminary dimensions for most of the components, complete simulations are performed as described in section 4 to determine the dimensions for the 9 swept variables that maximize specific impulse in the device.

Before results for the sweep are displayed, a few observations are made on the variables changed continously ($P_{wire_{superheater}}$, l_{ii}, l_{io}, d_w and l_w), that can be seen in the tables with the simulation results such as 7.3.2 and 7.3.4.

- Increasing the length of either of the insulators results in increased evaporation due to a more insulated superheater, and a larger surface of the accumulator receiving radiated heat. As temperature increases, the wire transfers less heat, and power usage is reduced.
- Increasing the outlet insulator length is one of the main reasons for specific impulse loss due to fluid cooling. Decreasing the heat exchange area decreases heat lost by the fluid.
- If insulation is insufficient extending the inlet insulation is preferred instead of extending outlet insulation, as the fluid becomes slightly preheated instead of cooled. However, if the outlet is inadequately insulated, the superheater temperature decreases due to the high heat losses and specific impulse is affected.
- As expected, increasing evaporating resistor heat increases the temperature in the accumulator's wall and the filter.
- Superheating wire's heat exchange area must be increased when both used power is low and evaporating is insufficient.
- Superheating wire's heat exchange area must be decreased when used power is high and the temperature difference between the wet walls and the liquid is above 100K.
- As long as the wire's heat exchange area is kept constant, changing the wire diameter and length has very little impact on the thermal results as it changes the superheater area very slightly. This means that once a wire length and diameter are found that fulfills the thermal requirement, electric requirements can be met with a quick change (decrease diameter and increase length if the voltage is exceeded, increase diameter and decrease length if the current is exceeded).

- Evaporation resistor heat is kept mostly at 5W since it was found that it was a power that allowed the device to be controllable. When using lower evaporation power to reach 100K of temperature difference between the liquid and the evaporator's walls, some devices had positive temperature differentials when disabling the evaporating resistor. This means that the simulation is not valid according to the thermal model used, since the temperature difference could be insufficient to evaporate the mass flow required by the nozzle.

As mentioned previously, the tank temperature is the first variable to be studied.

7.3.1 Tank temperature sweep

Tank temperature sweep is performed for a device with the characteristics in table 7.3.1. d_{sh} is 0.25mm bigger than the nozzle's choke diameter so that the Mach number does not exceed the 0.5 limits while maintaining a small superheater.

l_{sh} [mm]	d_{sh} [mm]	d^* [mm]
75	1.25	1

Table 7.3.1: Fixed dimensions for tank temperature analysis

After several iterations, configurations that meet all requirements are found for tank temperatures ranging between 343K and 347K. Specific impulse values are displayed taking into account the fixed nozzle efficiency of 75%. I_{sp} never reaches 200s, a maximum of 172s is found as seen in table 7.3.2. In this table temperature differences between the wet walls and the liquid ΔT_{wl_1} and ΔT_{wl_2} are included to show that the design is stable, reaching temperature differences above 100K consuming less than 50W, and having temperature differences of near-zero with an evaporating resistor's heat above 0. Electrical restrictions are met since the voltage required for the superheater V_{sh} is less than 6V and current I_{sh} is below 10.4A.

T_{tank} [K]	d_w [mm]	l_w [mm]	l_{io} [mm]	l_{ii} [mm]	$P_{wire_{superheater}}$ [W]	Power [W]	I_{sp} [s]	ΔT_{wl_1} [K]	ΔT_{wl_2} [K]	T_{sh} [K]	η_{power} [%]	V_{sh} [V]	I_{sh} [A]
343.15	0.57404	107.6	2.75	2.75	4.5	49.6	167.4	107	54	1209.9	67.9	5.1	8.1
343.15	0.57404	107.6	2.75	2.75	1.5	47	166.4	6	4	1201.2	72.5	5.2	8.2
344.15	0.57404	110.6	3.25	3.5	5.25	49.7	168.5	102	42	1241.6	71.8	5.2	7.9
344.15	0.57404	110.6	3.25	3.5	2.75	47.6	167.7	8.5	4	1235.5	75.6	5.2	8
345.15	0.57404	124.5	4	4.25	4.5	49.9	171.4	108	39	1299.8	73.8	5.5	7.6
345.15	0.57404	124.5	4	4.25	2	47.7	170.7	9	3.5	1295.3	77.5	5.6	7.6
346.15	0.57404	128.5	4.5	7	5	49.9	171.8	99.3	25	1323.7	77.7	5.6	7.4
346.15	0.57404	128.5	4.5	7	3.25	48.4	171.3	16	4	1320.8	80.5	5.6	7.4
347.15	0.57404	128.5	5	14	5.25	50	170.9	106	17	1326.5	79.5	5.6	7.4
347.15	0.57404	128.5	5	14	3.5	48.4	170.4	7	1	1323.9	82.3	5.6	7.4

Table 7.3.2: Simulations for 1mm nozzle diameter, 75mm superheater's duct length and 1.25mm superheater's duct diameter.

It is clear in table 7.3.2 that specific impulse reaches a maximum of 172s for a tank temperature of 346.15K (73°C). The tank temperature range in which the device can operate is limited:

- At low temperatures evaporation is achieved only with very small insulators, which cause a decrease in the superheater's temperature. Low superheater temperatures result in a decrease in specific impulse due to the fluid lacking heating, as seen in figure 7.3.1.

- At high temperatures the length of the insulation required to evaporate is too high. A decrease in specific impulse is seen due to the excessive length of the outer insulator (see figure 7.3.1). Power conversion efficiency increases with tank temperature due to longer superheater insulators.

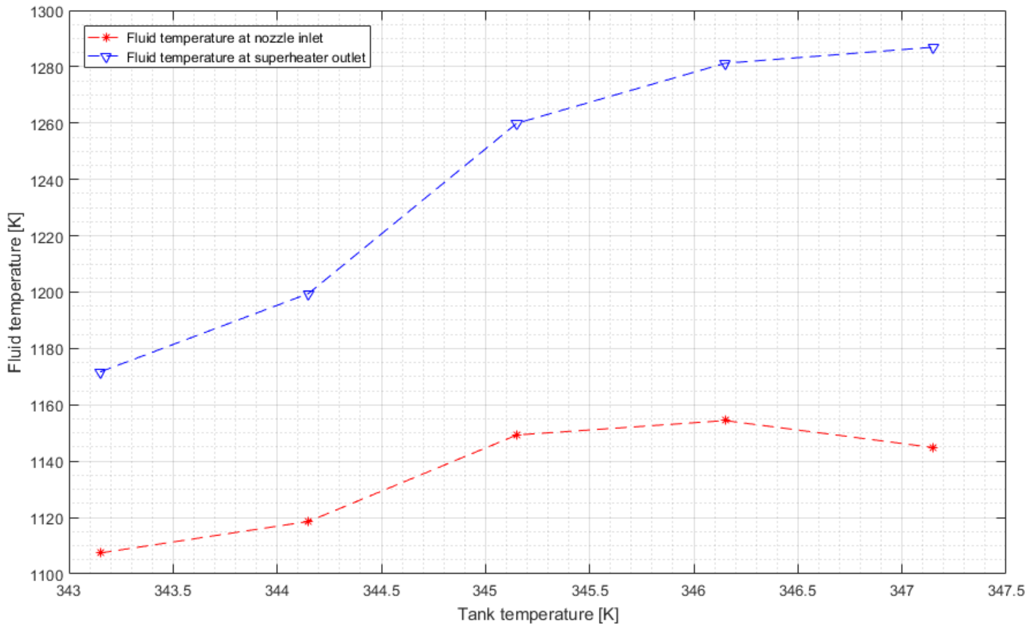

Figure 7.3.1: Fluid temperature at the superheater outlet and the inlet of the nozzle

Table 7.3.3 shows heat fluxes for different simulations. The difference in heat fluxes q_{io} and $q_{lost_{outer\ lid}}$ shows that not all of the conducted heat through the insulators is lost. In addition to heat losses through the outer lid, part of the heat is used to evaporate, and part is conducted to the exterior shell and then lost to the interior of the satellite. This highlights the importance of the nested design where the evaporator can receive heat at a quasi-constant temperature, and how it diminishes heat losses.

Poorly insulated superheaters such as the 343.15K design have huge heat losses by conduction, while higher tank temperatures lose less heat and have a higher heat recovery ratio, impacting both the power and energy efficiency, even when increasing the tank temperature is more energy and power demanding itself. Heat recovery increase is generally related to more heat being directly radiated to the accumulator's wall (due to longer insulators, the accumulator's wall has a greater surface), instead of leaving through the solid insulators, returning only a fraction to the evaporating walls.

T_{tank} [K]	q_{io} [W]	q_{ii} [W]	$q_{i_{rad}}$ [W]	$q_{lost_{outer\ lid}}$ [W]	$q_{lost_{inner\ lid}}$ [W]	$q_{lost_{shell}}$ [W]	$q_{lost_{tank}}$ [W]	$q_{lost_{total}}$ [W]	$P_{wire_{superheater}}$ [W]	$q_{recovered}$ [W]	$\eta_{recovery}$ [%]	η_{power} [%]	η_{energy} [%]
343.15	11.97	10.44	4.42	8.26	0.83	5.29	3.29	17.67	4.50	16.94	50.5%	67.9%	46.1%
344.15	10.92	8.75	5.11	7.15	0.71	4.65	3.35	15.86	5.25	17.54	54.9%	71.7%	50.6%
345.15	9.77	7.85	6.43	6.49	0.63	4.32	3.40	14.84	4.50	17.12	59.5%	73.8%	53.0%
346.15	9.24	5.04	7.57	5.18	0.48	3.59	3.47	12.72	5.00	17.61	65.6%	77.7%	57.9%
347.15	8.61	2.60	9.01	4.09	0.36	3.15	3.55	11.14	5.25	17.88	70.5%	79.5%	60.6%

Table 7.3.3: Heat fluxes for every tank temperature (with highest $P_{wire_{superheater}}$)

The tank temperature sweep indicates that to maximize specific impulse, an intermediate tank temperature has to be found for each nozzle diameter, superheater's duct length, and superheater's duct diameter. Since the lowest tank temperature is limited by the insulation length, iterations are performed by finding the tank temperature with very short insulators that results in a controllable device. Afterwards tank temperature is raised, while also increasing the insulation length.

7.3.2 Nozzle diameter sweep

The tank temperature sweep is repeated, but for nozzle throat diameters of 1.75, 1.5, 1.25 and 1mm. Characteristics of the device are displayed in table 7.3.4, including superheater duct's length l_{sh}, superheater duct's diameter d_{sh}, nozzle throat diameter d^*, nozzle divergent length l_{div} and nozzle exit diameter d_{exit}.

l_{sh} [mm]	d_{sh} [mm]	d^* [mm]	l_{div} [mm]	d_{exit} [mm]
75	1.25	1	12.6	12.7
75	1.5	1.25	13.8	14.1
75	1.75	1.5	17.3	17.6
75	2	1.75	21	21.3

Table 7.3.4: Fixed dimensions for nozzle throat diameter analysis

Figure 7.3.2 shows that for choke diameters between 1 - 1.5mm a tank temperature providing maximum specific impulse is found, with 1mm choke diameter reaching the highest specific impulse of 172s. However, variation is very small, resulting in differences of 4s of I_{sp} between the smallest and largest nozzle. Smaller nozzles require higher tank temperature partly because of increased pressure losses due to smaller duct diameters (see equation 5.3.3).

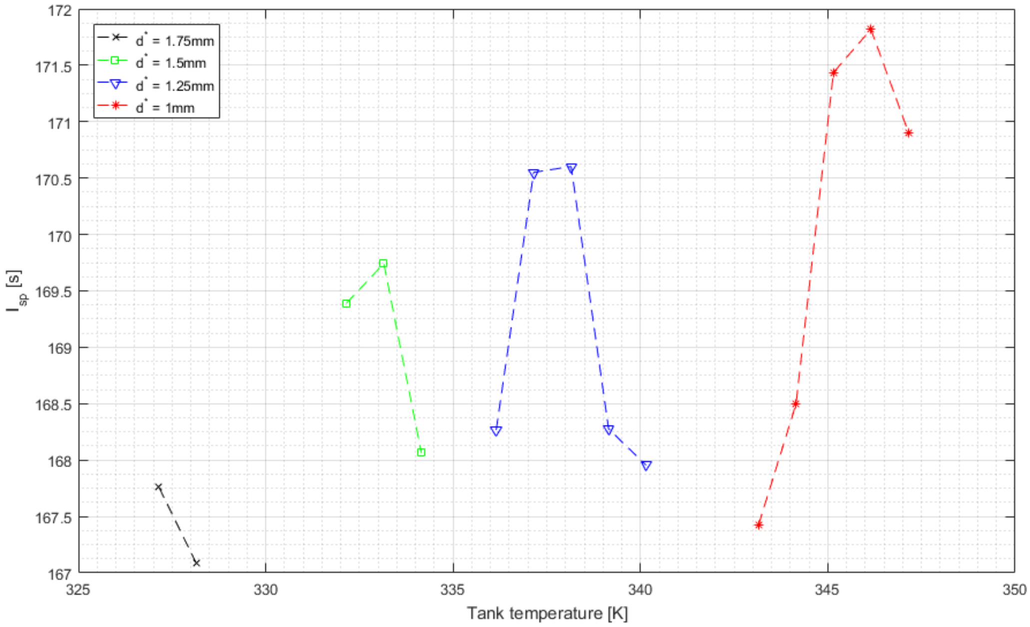

Figure 7.3.2: Specific impulse versus tank temperature for all nozzle throat diameters

Thermal resistance decreases when increasing choke diameter. A larger nozzle throat diameter implies a larger superheater duct's diameter, and therefore a larger superheater's diameter. An increased heat exchange area provides the same result as decreasing the insulator's length, an effect seen in the tank temperature sweep. Lower superheater temperatures are obtained for larger throat diameters, as shown in figure 7.3.3. In this case, fluid cooling in the superheater-nozzle connection is similar in all cases, as they end up having similar lengths.

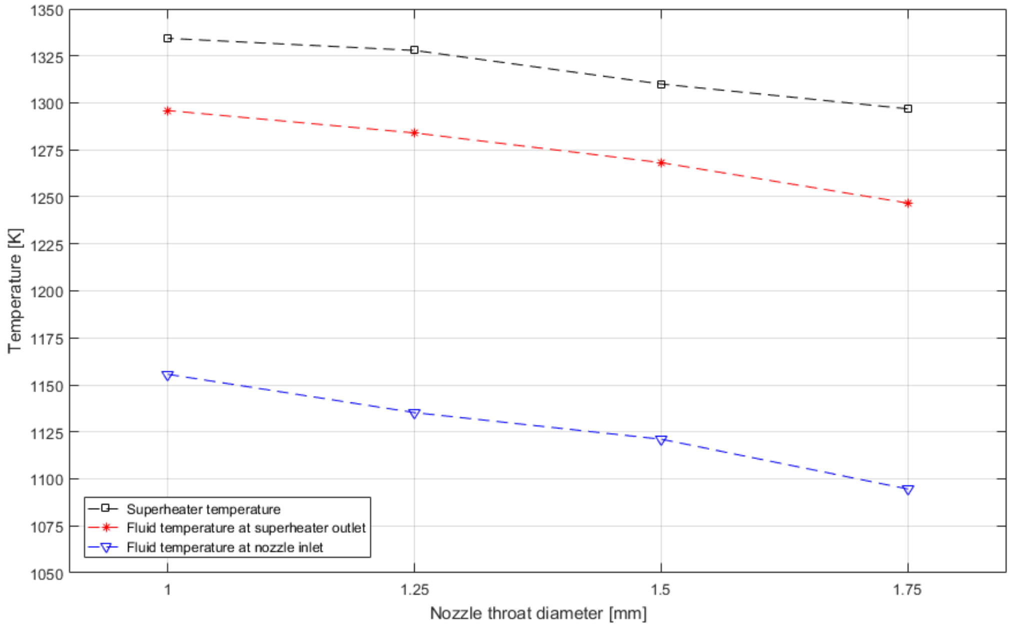

Figure 7.3.3: Superheater and fluid temperatures for all nozzle throat diameters

Regarding efficiency, no clear correlation between nozzle diameter and power or energetic efficiency is found, caused by decreasing superheater temperatures with diameter, while also being less insulated. Results are displayed in table 7.3.5. This is due to the superheater temperature decreasing with diameter, while also being less insulated.

d^* [mm]	T_{tank} [K]	η_{power} [%]	η_{energy} [%]
1	346.15	77.7%	57.9%
1.25	338.15	76.1%	55.8%
1.5	333.15	79.0%	60.4%
1.75	327.15	74.1%	53.3%

Table 7.3.5: Efficiencies for various nozzle diameters

Fluid exit temperature is checked to avoid sublimation, ensuring that the length of the nozzle is chosen adequately. Both fluid exit temperature and sublimation temperature are shown in 7.3.6. $T_{sublimation}$ is the temperature at which the gas expanding isentropically in the nozzle would reach sublimation. Temperature differences nearing 20K show that the fluid is as expanded as possible in order not to lose specific impulse.

d^* [mm]	Kn^*	$T_{sublimation}$ [K]	$T_{nozzle_{out}}$ [K]
1	0.0469	201.6	223.8
1.25	0.0583	198.5	235.1
1.5	0.0667	196.4	228
1.75	0.0788	194.7	218.2

Table 7.3.6: Knudsen numbers for studied nozzle throat diameters

Table 7.3.6 also includes Knudsen numbers calculated in the nozzle's throat. Kn remains above 0.01, indicating that rarefaction effects in the divergent section of the nozzle will occur. Figure 7.3.4 shows the increasing Kn as the gas expands in a 1mm isentropic nozzle, exceeding 0.1 on a 2mm diameter area, and therefore justifying the selection of the diminished specific impulse efficiency of 75%. Due to the XSteam function limitations Kn is not calculated at more expanded stages, and since the fluid at 600K is not close to being fully expanded (400K above exit temperature), rarefaction is expected to be more intense as fluid expands.

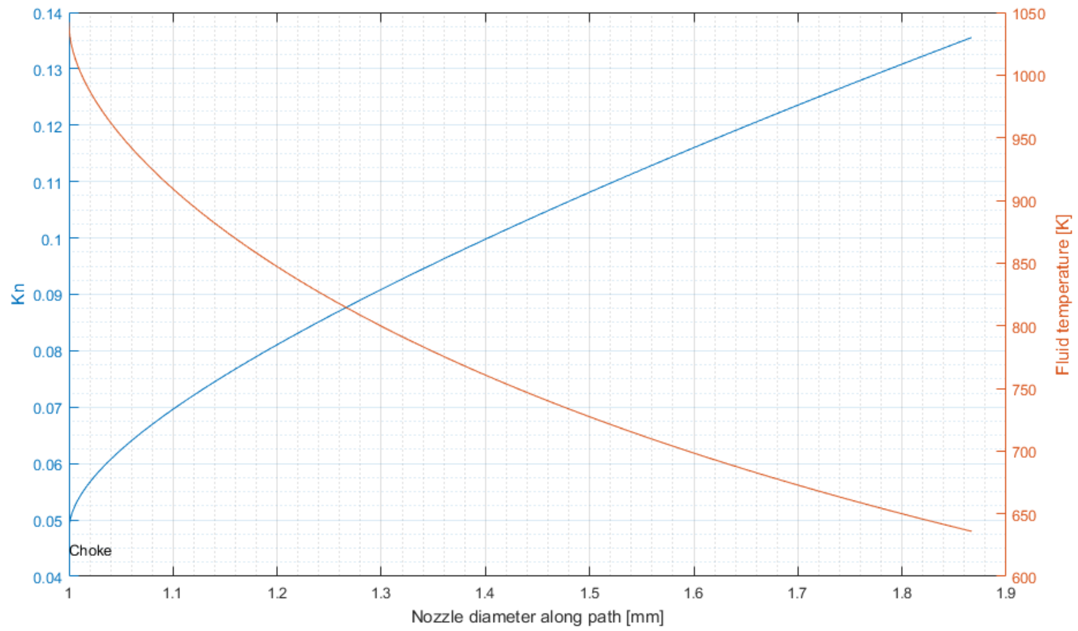

Figure 7.3.4: Knudsen number and fluid temperature in the divergent section of a 1mm nozzle throat diameter

Nozzle diameter sweep shows that the nozzle should be kept at 1mm, achieving the highest specific impulse and comparable power and energy efficiencies. Diameters below the manufacturing limit are not studied, but since the insulation diameter plays a major role in heat transfer, a smaller nozzle would enable hotter superheaters, with short insulators and little fluid cooling, increasing specific impulse.

Rarefaction effects are unavoidable and one of the major limitations on reaching the target specific impulse of 200s. If a specific impulse efficiency of 95% could be reached, as in flows that do not experience rarefaction, the resulting I_{sp} would be of 206s instead of 172s.

7.3.3 Superheater duct's diameter sweep

In previous sections 7.3.1 and 7.3.2 the superheater's duct diameter is kept 0.25mm larger than the nozzle diameter to prevent the fluid from reaching Mach 0.5. In this section the superheater's duct diameter is increased to analyze its impact in the device's performance. Section 5.3.2 shows that specific impulse itself should not be affected with a larger duct, as long as the superheater remains at the same temperature. Since the superheater changes in size, heat transfer is affected and an analysis is necessary to check if the same temperatures can be achieved with larger ducts, and how it impacts efficiency.

For a 1mm nozzle, the superheater's duct diameter is increased by 0.25mm to 1.5mm and the results are compared.

Specific impulse for smaller superheaters is slightly higher as seen in table 7.3.7. Larger superheaters are poorly insulated, therefore their temperature T_{sh} does not reach temperatures as high as the superheater with 1.25mm ducts. Propellant's temperature in the superheater outlet $T_{p_{sh\ out}}$ shows that smaller superheaters result in higher temperature propellant, but when looking at the propellant's temperature at the nozzle inlet $T_{p_{nozzle\ in}}$, increased fluid cooling in 1.25mm ducts causes temperatures (and therefore specific impulse) to be comparable for both 1.5mm ducts and 1.25mm ducts. This is attributed to the fact that 1.25mm ducts have outlet insulators that are 0.5mm shorter than 1.5mm ducts since outer lid temperatures are similar (around 450K) for both cases.

Pressure drop across the ducts Δp_{sh} (includes insulators) decreases for larger diameters as expected. The nozzle diameter does not change and nozzle fluid inlet temperatures are similar, therefore to satisfy equation 4.6.1, mass flow through 1.5mm ducts is higher than in 1.25mm ducts.

d_{sh} [mm]	T_{tank} [K]	I_{sp} [s]	T_{sh} [K]	$T_{p_{sh\ out}}$ [K]	$T_{p_{nozzle\ in}}$ [K]	Δp_{ducts} [Pa]	$p_{p_{nozzle\ in}}$ [Pa]
1.5	337.15	167.67	1207.07	11762	1119.69	9671	10994
	338.15	170.30	1254.47	1223.10	1147.26	10223	11550
	339.15	171.10	1296.86	1262.48	1155.64	10774	12149
	340.15	168.87	1315.59	1273.24	1133.31	11224	12893
1.25	344.15	168.50	1241.64	1199.51	1118.61	17547	11813
	345.15	171.44	1299.78	1259.92	1149.30	18638	12155
	346.15	171.82	1323.72	1281.23	1154.41	19492	12788
	347.15	170.91	1326.53	1286.93	1144.84	20704	13117

Table 7.3.7: Simulation results for superheater duct's diameters of 1.5 and 1.25mm.

When looking at lost heat and efficiencies, 1.25mm duct results are favored due to increased insulation. As displayed in table 7.3.8, heat recovery, power conversion efficiency, and energy efficiency make the 1.25mm duct the choice for the superheater duct's diameter.

Reduced duct diameters, even if they require higher tank temperatures to compensate for the increased pressure drop, result beneficial due to their smaller size, therefore a 1.25mm duct is chosen. At a temperature 30K higher than the 1.5mm duct superheater, the superheater with 1.25mm ducts conducts less heat through the connectors with the outer and inner lids (q_{io} and q_{ii}). Radiation surface is decreased at smaller superheater diameters, but a hotter superheater compensates and results in more radiation heat directly reaching the evaporator ($q_{i_{rad}}$), enhancing heat recovery with an improvement from 55.3 to 57.7%. Insulators smaller in diameter also allow for fewer heat losses through the lids and exterior shell (q_{lost}), since their high thermal resistance cause decreased heat flux with an increased temperature differential (superheater is hotter and lids are colder), raising both the power and energy efficiency by 3.4% and 4% respectively.

d_{sh} [mm]	I_{sp} [s]	q_{io} [W]	q_{ii} [W]	$q_{i_{rad}}$ [W]	$q_{lost_{outer\ lid}}$ [W]	$q_{lost_{inner\ lid}}$ [W]	$q_{lost_{shell}}$ [W]	$q_{lost_{tank}}$ [W]	$q_{lost_{total}}$ [W]	$P_{wire_{superheater}}$ [W]	$q_{recovered}$ [W]	$\eta_{recovery}$ [%]	η_{power} [%]	η_{energy} [%]
1.5	171.10	10.79	7.70	6.75	6.33	0.61	4.34	2.99	14.27	3.25	13.95	65.9%	74.3%	53.9%
1.25	171.82	9.24	5.04	7.57	5.18	0.48	3.59	3.47	12.72	5.00	12.61	61.8%	77.7%	57.9%

Table 7.3.8: Heat fluxes for both superheater diameters (with highest I_{sp})

7.3.4 Superheater duct's length sweep

Analysis for the superheater duct's length is presented in this section, as changes in this variable affect both the fluid heating by providing more heat exchange area and making it more likely that the fluid reaches the temperature of the superheater, but it also affects the superheater geometry and therefore its heat losses and final temperature. As it was previously stated, short duct superheaters have reduced superheater overall length and therefore less exposed area radiating to the evaporator's wall. For a nozzle throat diameter of 1mm and duct diameter of 1.25mm, lengths of 55, 65, 75, and 85mm are analyzed.

The first result to be analyzed is the specific impulse, seen for all four lengths in figure 7.3.5. Although the heat transfer area for the fluid is larger in 85mm ducts, the 65mm simulation gives the best results, nearing 172s of specific impulse.

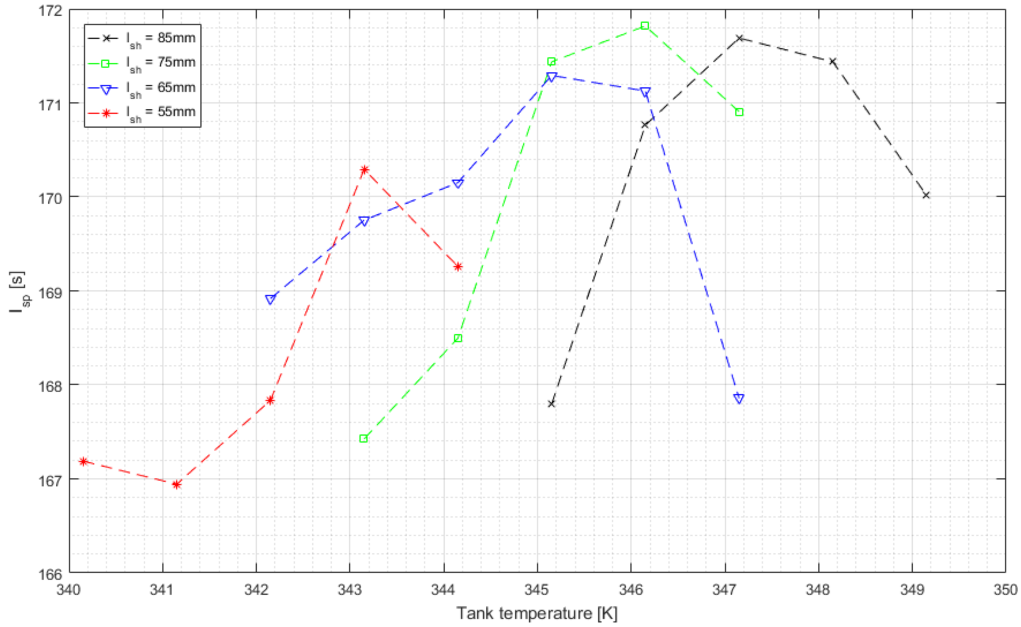

Figure 7.3.5: Specific impulse versus tank temperature for all duct lengths

The I_{sp} maximum found for 75mm is explained by the superheater temperature, the fluid's temperature at the superheater outlet, and the nozzle's inlet, seen in figure 7.3.6.

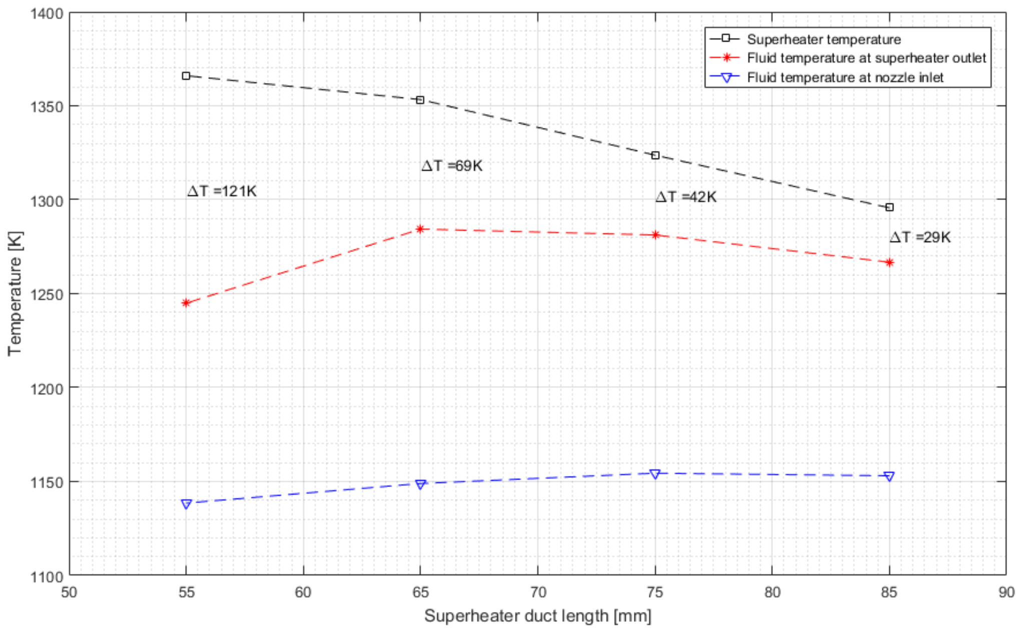

Figure 7.3.6: Fluid and solid temperatures for all duct lengths

Only tank temperatures with maximized I_{sp} for each duct length are selected. As expected, the temperature difference between the fluid at the superheater outlet and the superheater itself decreases with a longer duct, but longer ducts are usually at a lower temperature, resulting in the maximum temperature reached for the fluid for a 65mm duct.

The 65mm duct reaches a higher temperature than the 75mm simulation due to the higher temperature of the superheater, with mass flow being very similar (33 vs 32.3 $\frac{g}{h}$)). However, the connector for the 65mm duct is slightly longer (5mm vs 4.5mm) and at a lower temperature (459K vs 471K), and fluid is cooled more than for the 75mm duct superheater. This causes the 75mm duct to have the highest specific impulse for all four lengths.

Efficiencies have a greater variation than specific impulse, shown in table 7.3.9. In addition to fluid heating phenomenons explained previously, the 55mm duct fails to radiate as much as the 65mm duct due to its lower area even if it reaches a temperature 20K higher. Increased radiation heat transfer boosts the heat recovery percentage, and adding this to decreased conducted heat through the superheater insulators, makes the 65mm duct the most efficient in both power and energy usage. It has an adequate balance between the superheater's temperature and the heat transfer areas, both for the fluid and radiation heat transfer.

l_{sh} [mm]	T_{tank} [K]	q_{io} [W]	q_{ii} [W]	$q_{i_{rad}}$ [W]	$q_{lost_{outer\ lid}}$ [W]	$q_{lost_{inner\ lid}}$ [W]	$q_{lost_{shell}}$ [W]	$q_{lost_{tank}}$ [W]	$q_{lost_{total}}$ [W]	$P_{wire_{superheater}}$ [W]	$q_{recovered}$ [W]	$\eta_{recovery}$ [%]	η_{power} [%]	η_{energy} [%]
85	347.15	9.99	4.87	7.26	5.29	0.49	3.77	3.55	13.10	5.00	12.57	56.8%	76.9%	56%
75	346.15	9.24	5.04	7.57	5.18	0.48	3.59	3.47	12.72	5.00	12.61	57.7%	77.7%	57.9%
65	345.15	8.71	4.33	8.20	4.76	0.43	3.28	3.41	11.88	5.00	12.77	60.1%	79.1%	60.0%
55	343.15	9.70	4.63	7.78	5.11	0.47	3.36	3.27	12.22	5.00	13.16	59.5%	78.3%	59.5%

Table 7.3.9: Heat fluxes for several superheater duct's lengths (with highest I_{sp})

If the total energy used to achieve a target ΔV is calculated, the 65mm superheater is the one that uses the least energy, compensating for a very slight decrease in I_{sp} with increased power and energetic efficiency, as seen in table 7.3.10, and also the design with the highest $\Delta V_{impulse\ event}$. If a ΔV and propellant mass ratio is calculated, the 65mm duct is 0.56% worse than the 75mm duct, as expected as ΔV and propellant mass are only related by specific impulse. When comparing ΔV per impulse event, the 65mm duct's performance is 3.5% better than the 75mm duct. This occurs due to the extended impulse duration for the 65mm duct thanks to its improved energetic efficiency.

The difference between obtained $\Delta V_{impulse\ event}$'s is small. If a ΔV common in resistojet missions of $50\frac{m}{s}$ is considered, all devices require at least 7 impulse events to reach the desired ΔV. In the case a resistojet is needed for larger missions, choosing this duct could reduce the number of impulse events, helping to a faster deployment due to the diminished needed energy (assuming that the rate of solar energy harvesting is kept constant).

l_{sh} [mm]	$m_{p_{impulse\ event}}$ [g]	$E_{impulse\ event}$ [Wh]	$\Delta V_{impulse\ event}$ $\left[\frac{m}{s}\right]$	$\frac{\Delta V_{impulse\ event}}{m_{p_{impulse\ event}}}$ $\left[\frac{\frac{m}{s}}{g}\right]$
85	36.44	77	5.95	0.1632
75	37.25	77	6.09	0.1635
65	38.71	77	6.30	0.1628
55	38.57	77	6.24	0.1618

Table 7.3.10: Propellant mass, total used energy and ΔV per impulse event

With a selected duct's length of 65mm, all the dimensions of the device have been set, with its operation points determined. Detailed results for the device's performance and its analysis are presented in section 8.

8 Simulation model results and final device

This section presents the final device, with its performance and information about temperatures and heat fluxes in both idle and active modes. This design uses results from section 7, with minor tweaks that enable the use of standard components such as sealing o-rings. Changes occur especially in energetic consumption from the solid parts. Final values for the swept variables are displayed in table 8.1.

The swept variables final values are displayed in table 8.1

Variable	Unit	Value
d^*	[mm]	1
d_{sh}	[mm]	1.25
l_{sh}	[mm]	65
T_{tank}	[K]	345.15
l_{wire}	[mm]	131.7
d_{wire}	[mm]	0.6438 (AWG 22)
l_{io}	[mm]	4.5
l_{ii}	[mm]	7
$P_{wire_{superheater}}$	[W]	2.9 - 4.8

Table 8.1: Swept variables final values

Results for the model are separated into temperatures and heat fluxes for both solids and the fluid, mass, and energy distribution according to the obtained temperatures, and efficiencies. Subsection 8.6 adds a summary of the results, in which data is arranged to match commonly provided specifications sheets from resistojet manufacturers.

8.1 Solid temperatures and heat fluxes

In this section heat fluxes and temperatures for solids are displayed, split into three to analyze active cases 1 and 2, and the idle case separately.

8.1.1 Active case 1

Figure 8.1.1 shows heat fluxes and temperatures in nodes for active case 1. The transparent device is added with the final dimensions. It should be taken into account that heat fluxes were rounded to the closest 0.01W and temperatures to the closes 0.01K. Heat fluxes added by electrical resistors are shown in orange, while heat fluxes with fluid are depicted in green.

As it is observable, the superheater reaches temperatures higher than 1350K. Evaporator walls (nodes 10 and 11) are 101K above liquid temperature (345.15K), the limit temperature for pool boiling reported by Oka. Nodes for the lids and the exterior shell, 4, 7, and 14, reach a temperature of 440K achieving a low temperature difference with the accumulator's walls. This

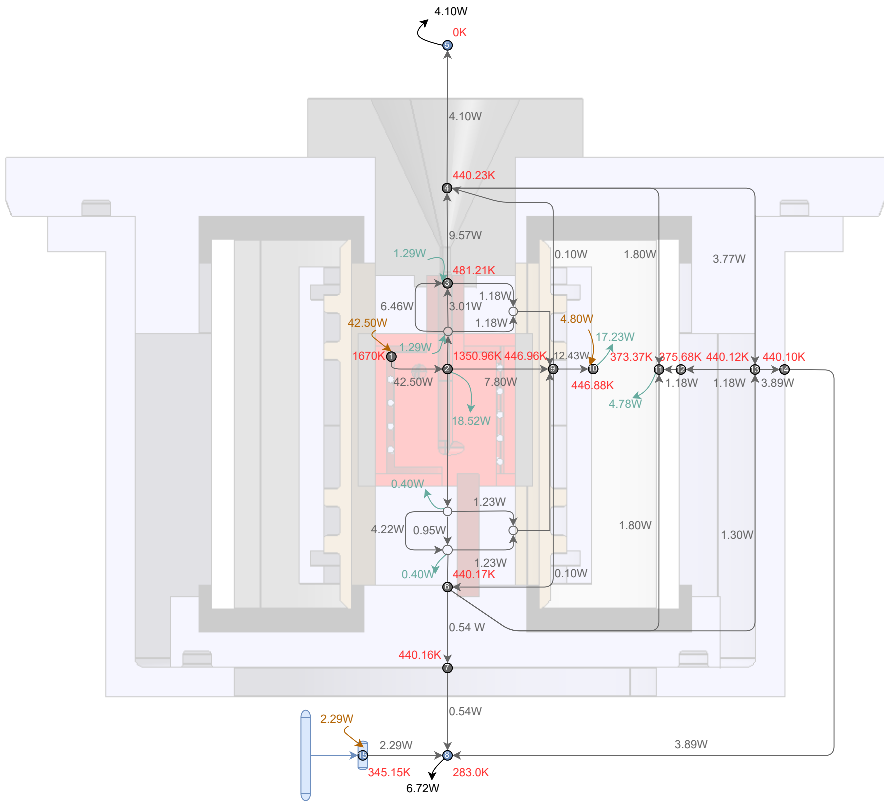

Figure 8.1.1: Heat fluxes and temperatures for active mode 1

indicates that evaporation sets the temperature of the outer surface and is useful to have an overall low device temperature.

Evaporating resistor's temperature is not displayed in the thermal circuit, but its temperature does not exceed 450K thanks to the high thermal conductivity grease and low thickness insulating films, allowing for adequate heat transfer with a low-temperature difference.

The temperature gradient from the superheater to the outer part of the propulsion system occurs in the insulators, with heat being transferred to the lids where heat flows back to the evaporator, to the exterior shell, or leaves the system.

More than 42W of power is dissipated by the superheating resistor, of which only 18.52W reaches the superheated fluid. The rest of the heat is split between conducted heat through the insulators and radiated heat to the evaporator.

Around 12.6W flow by radiation from the superheater and insulators to the evaporator. 0.10W flow from the accumulator to each of the lids, but the lids also transfer 3.6W to the PTFE filter that is used to evaporate, along with the 1.18W that are radiated from the exterior shell to the filter, evaporating in total 4.78 W.

Heat losses are seen in heat fluxes to 8 and 5. Contrary to what was expected, most of the heat is lost to the interior of the satellite. If heat losses from the exterior shell (nodes 14 to 8) are observed, they are comparable in magnitude to heat losses to outer space (nodes 4 to 5). Although radiating to a higher temperature source, the exterior's shell area and the pre-tank area are greater than the area of the outer lid and the divergent part of the nozzle, radiating both to outer space. 62% or 6.72W of the losses are to the interior of the satellite.

Of the 42.5W dissipated by the superheater's resistor, only 18.52W end up in the fluid, meaning that 23.98W leave the superheater. With 22W used to evaporate and 4.8W provided by the evaporator's resistor, 71.8% if the lost heat is reused.

The evaporating resistor dissipates 4.8W, with the pre-tank power reaching values of 2.29W. Added to the 42.5W of the superheater, total power consumption reaches 49.59W.

Nodes 2, 3, 6, 10, and 11 have input heat from the fluid submodel. It is observable that fluid is pre-heated in the inlet duct, absorbing 0.8W, and cooled in the outlet duct, losing 2.58W. An in-depth analysis for fluid heat transfer is presented in section 8.2.

8.1.2 Active case 2

For case 2, temperature distribution is similar as shown in figure 8.1.2. A 1348K superheater loses heat to lids at 420K, with an evaporator 7K above liquid propellant temperature.

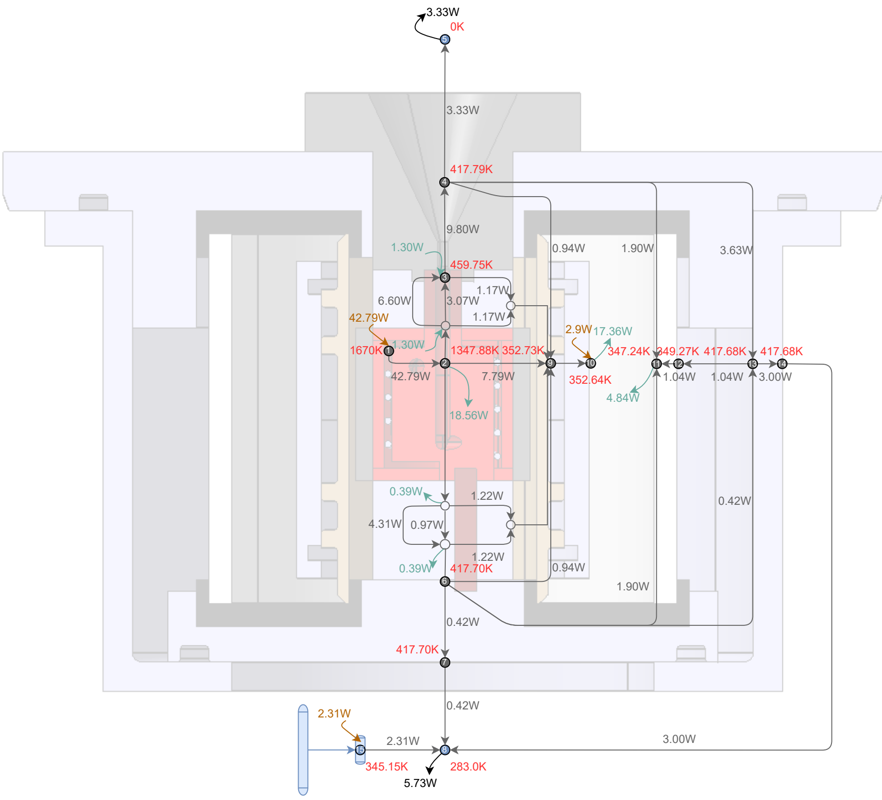

Figure 8.1.2: Heat fluxes and temperatures for active mode 2

Of the 42.49W dissipated by the superheater's resistor, only 18.56W end up in the fluid, meaning that 24.23W leave the superheater. With 22.2W used to evaporate and 2.9W provided by the evaporator's resisotr, 79.7% of the los heat is resued.

2.9W is used in the evaporating resistor to reach an adequate mass flow. 2.31W are lost in the pre-tank, slightly different from active case 1 since the pre-tank for case 2 carries more mass due to the lower energy consumption of the device. Total power of 48W is used in the system.

8.1.3 Idle mode

At idle, with a set temperature of 400K in the superheating resistor, as shown in figure 8.1.3, the power consumption is 0.2W, seen as the input heat in node 2. Components' temperatures are within their safe operation ranges. Aluminum and PTFE components have a temperature between 257 and 260K, while the superheater's minimum temperature is 269K or -4°C.

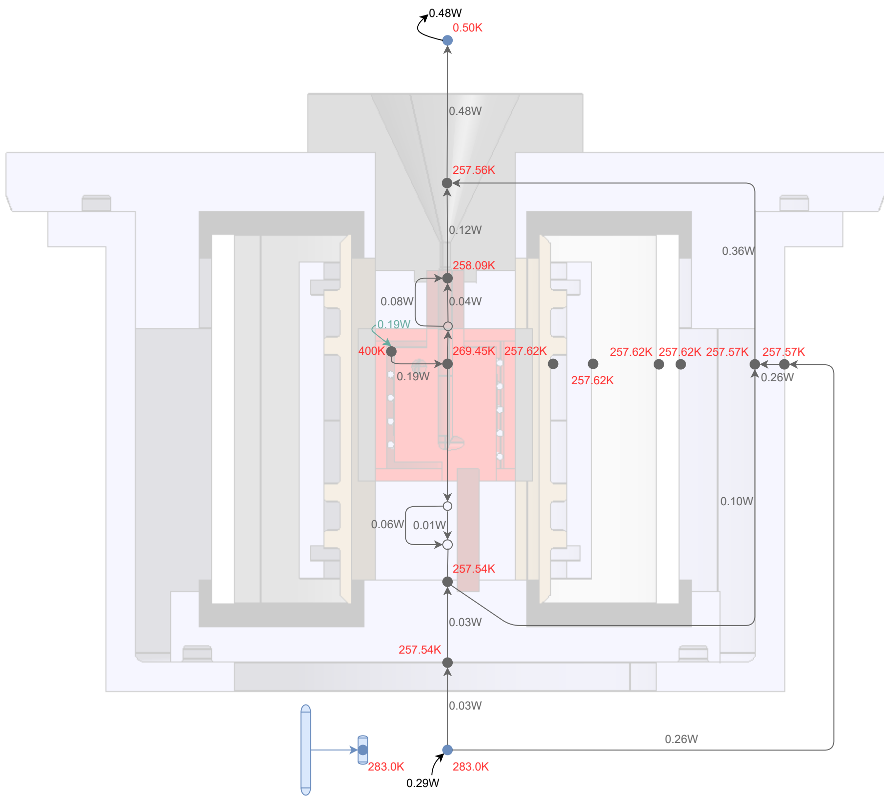

Figure 8.1.3: Heat fluxes and temperatures for idle mode

8.2 Fluid temperatures and heat fluxes

With solid temperatures already shown in section 8.1, fluid temperatures and exchanged heats are presented in this section.

8.2.1 Evaporator

Evaporated mass flow obtained in the simulation is of $34.03\frac{g}{h}$ for case 1 and $34.32\frac{g}{h}$ for case 2.

Table 8.2.1 shows how much heat is used to evaporate and the mass evaporated in each wall. The accumulator's wall receives the radiation from the superheater and the resistor's heat and, as expected, it evaporates much more mass flow than the PTFE filter.

The pre-tank is at a temperature of 345.15K, with its saturation pressure being 34000Pa. With the safety factor for the filter being 2, the steam chamber pressure is 30790Pa for both cases 1 and 2. As the discharge of the steam through the filter is isenthalpic, the inlet temperature to the superheater is slightly below 345.15K but this effect is negligible.

Case	$P_{wire_{superheater}}$ [W]	$q_{e_{wall}}$ [W]	$q_{e_{PTFE}}$ [W]	ΔT_{wall} [K]	ΔT_{PTFE} [K]	$\dot{m}_{e_{wall}}$ $[\frac{g}{h}]$	$\dot{m}_{e_{PTFE}}$ $[\frac{g}{h}]$
1	4.8	17.22	4.78	101.7	28.2	26.40	7.39
2	2.9	17.36	4.84	7.5	2.1	26.84	7.48

Table 8.2.1: Evaporation results

8.2.2 Inner insulation duct

The fluid, after leaving the steam chamber, flows through the inner insulator duct starting at a temperature of 345K and a pressure of 30790Pa, and exchanges heat with a solid at temperatures that start at 400K and nears 1345K as the fluid is closer to the superheater. Table 8.2.2 shows a comparison between the variables at the inlet and outlet of the duct. q also represents the heat gained by the fluid. Speed is not high, but low pressure and therefore low density result in a Mach number of near 0.1 at both ends of the inner insulator.

Case	T_{in} [K]	p_{in} [Pa]	v_{in} $[\frac{m}{s}]$	T_{out} [K]	p_{out} [Pa]	v_{out} $[\frac{m}{s}]$	q [W]
1	344.8	30793	39.5	388.0	30597	44.9	0.80
2	344.8	30793	39.5	386	30597	45.1	0.78

Table 8.2.2: Inlet and outlet conditions for the inner connector duct

For both cases 1 and 2, the fluid is slightly preheated and along with the heating, velocity is raised. The pressure drop in the inner duct is very low. Heat exchanged is slightly higher for case 1 due to a lower mass flow and higher overall solid temperature.

Heat values 0.8W and 0.78W are split in half and served as generated heat to nodes 6 and 2 as seen in figures 8.1.1 and 8.1.2.

8.2.3 Superheater

When in the superheater, due to the high-temperature difference and duct length, the fluid's temperature is raised and pressure drops accordingly. Also, the fluid gets greatly accelerated, reaching Mach numbers nearing 0.5, the simulation's model limit.

Figure 8.2.1 shows how, for case 1, the fluid's temperature raises as it travels through the superheater duct. An interesting effect occurs in the duct, where heat exchange per unit area finds a maximum at an intermediate temperature due to steam's thermal conductivity increasing with the duct position (see table 8.2.3 for thermal conductivity at the inlet and outlet of the superheater). The convection coefficient for the fluid increases proportionally with thermal conductivity. For the final stages of the duct, with a reduced temperature difference, heat transfer decreases as well.

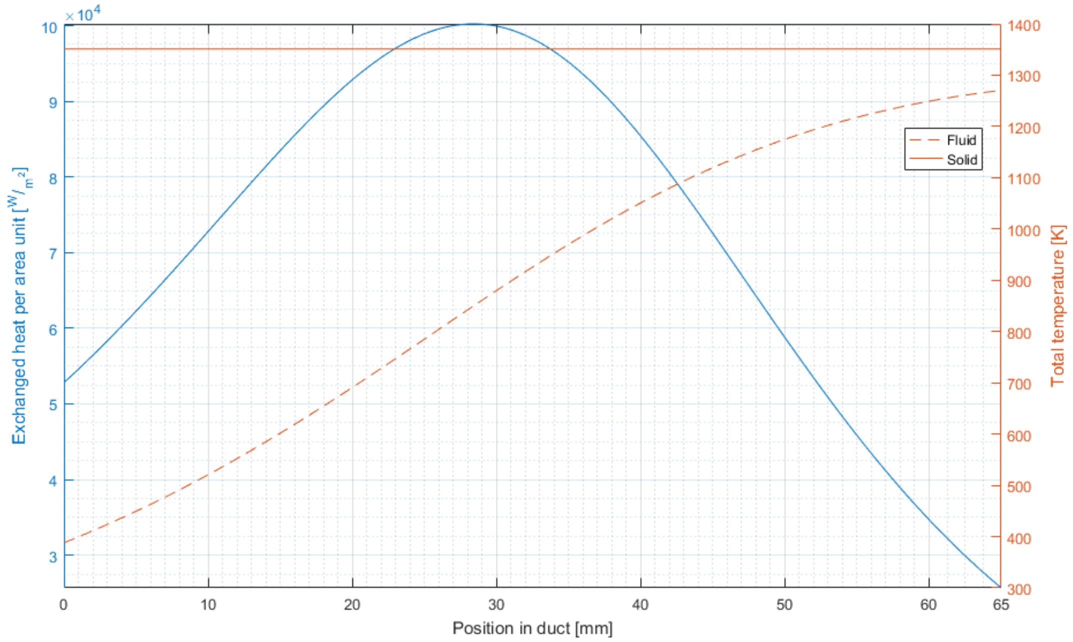

Figure 8.2.1: Fluid temperature raise in the superheater

In figure 8.2.2 increasing velocity and decreasing pressure of the fluid are observable. Mach numbers nearing 0.4 are reached. Pressure decreases by almost 50% in the superheater, because the fluid heating increases speed, and increased speed is associated with more pressure drop.

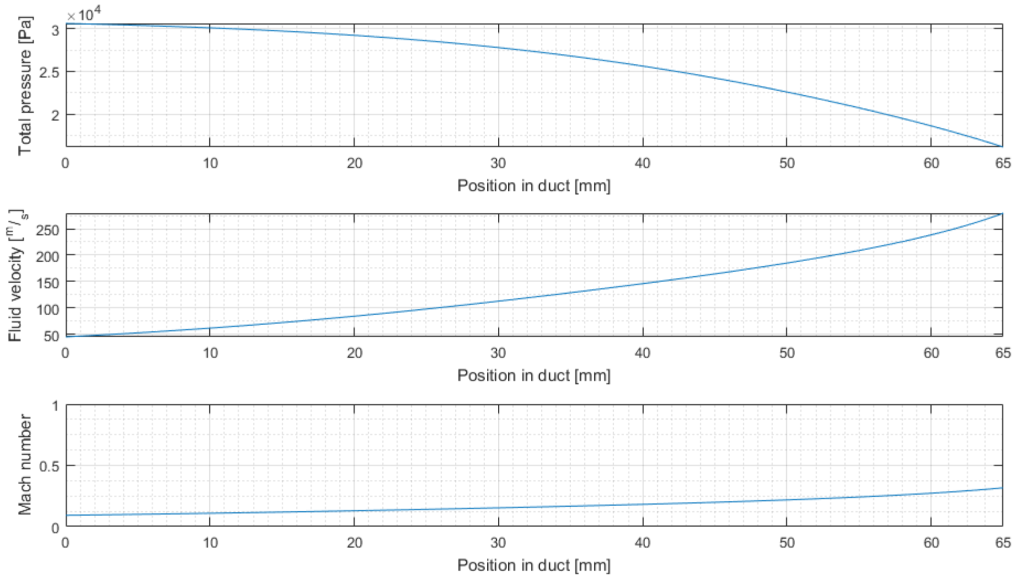

Figure 8.2.2: Fluid pressure, velocity and mach numbers in the superheater

Table 8.2.3 provides a summary of the conditions at the inlet and outlet of the superheater for cases 1 and 2. In this case, thermal conductivity is included to explain part of figure 8.2.1.

Over 18W are required to superheat the flowing $34\frac{g}{h}$ of steam, raising its temperature by almost 900K. Only 18W are utilized of the over 40W dissipated by the superheating resistor, losing more than 50% of the power used in the superheater, part of which is later reutilized.

Case	T_{in} [K]	p_{in} [Pa]	v_{in} $[\frac{m}{s}]$	Ma_{in}	k_{in} $\left[\frac{W}{mK}\right]$	T_{out} [K]	p_{out} [Pa]	v_{out} $[\frac{m}{s}]$	Ma_{out}	k_{out} $\left[\frac{W}{mK}\right]$	q [W]
1	388.0	30597	44.9	0.093	0.025	1270.0	15949	283.0	0.333	0.139	18.52
2	386	30597	45.1	0.093	0.025	1263.2	16000	283.2	0.334	0.138	18.56

Table 8.2.3: Inlet and outlet conditions for the superheater duct

8.2.4 Outer insulator duct

The outer insulator is the last duct to be analyzed. As seen in figure 8.2.3 the fluid is cooled since the insulation connects the superheater and the nozzle, at a lower temperature than the superheater. Temperature increases slightly in the first millimeter of the duct, but heat flux is negative afterward and the temperature drops.

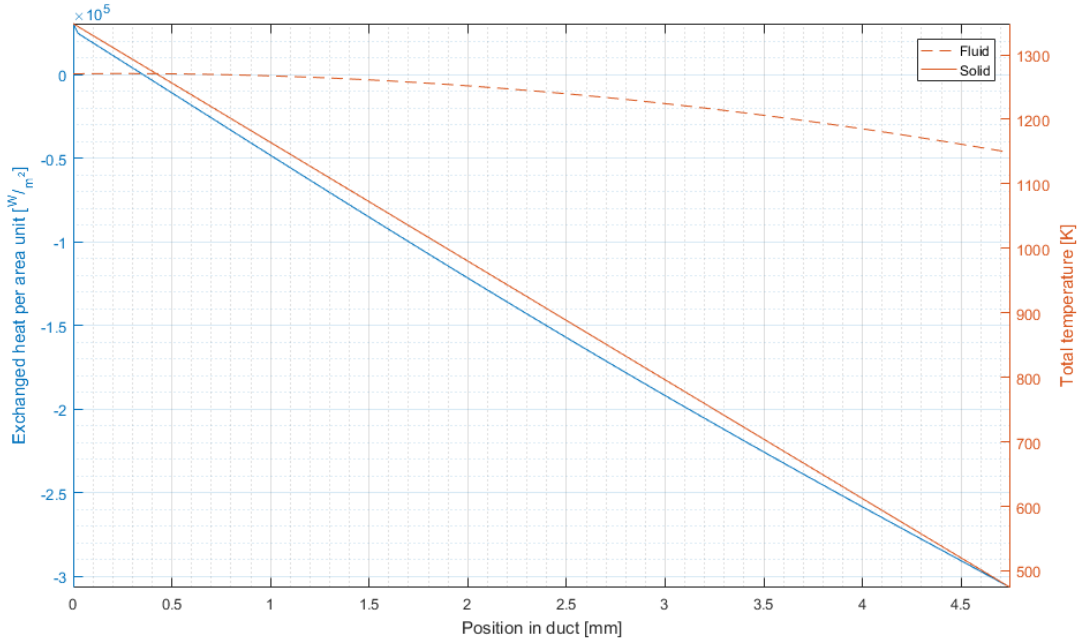

Figure 8.2.3: Fluid temperature and heat flux in the outer insulator

Pressure keeps decreasing, and the Mach number increases. Mach reaches a value very close to 0.5. Inlet and outlet conditions for fluid in the outer insulator are presented in table 8.2.4, where exchanged heat values exceed 2W. Even with a very short connecting duct of 4.5mm, 13.5% of the enthalpy gained by heating is lost, causing a decrease in fluid temperature of 115K for both cases 1 and 2. This temperature loss has a great impact on specific impulse since the ideal I_{sp} for 1270K and 1155 fluid are 252s and 238s respectively. This represents a 5.6% ideal specific impulse loss.

Case	T_{in} [K]	p_{in} [Pa]	v_{in} $[\frac{m}{s}]$	Ma_{in}	T_{out} [K]	p_{out} [Pa]	v_{out} $[\frac{m}{s}]$	Ma_{out}	q [W]
1	1270.0	15949	283.0	0.333	1155.8	13455	305.3	0.376	-2.57
2	1263.6	16000	283.2	0.334	1148.6	13529	304.4	0.376	-2.61

Table 8.2.4: Inlet and outlet conditions for the outer insulator duct

8.2.5 Nozzle

Fluid static properties at the nozzle inlet are T_{out} and p_{out}, with v_{out} as the fluid's velocity. When calculating total temperature, T_{0out} results in 1167.8K and 1160.6K for cases 1 and 2 respectively, differing slightly from temperatures in table 8.2.4. I_{sp} and thrust are therefore calculated and penalized by the 75% nozzle efficiency due to the low Knudsen number, displayed in table 8.2.5 along with other results. Exit temperature is checked to be above sublimation temperature.

Case	$T_{0_{nozzle}}$ [K]	$p_{0_{nozzle}}$ [Pa]	I_{sp} $[\frac{m}{s}]$	F [mN]	$T_{out_{nozzle}}$ [K]	$T_{sublimation}$ [K]	Kn
1	1175.2	13454	171.95	15.94	224.1	202.0	0.046
2	1168.0	13529	171.27	16.02	222.3	202.4	0.045

Table 8.2.5: Nozzle inlet conditions, specific impulse, thrust and sublimation checks

Two very important characteristics of the propulsion system are obtained as I_{sp} and F. Specific impulse ranges between 170 and 172s, slightly lower than the specific impulse reported by Bradford's COMET and SpaceJet's TunaCan Thruster. The thrust of 16mN is lower than COMET's 17mN, with similar power consumption. The TunaCan thruster has 6mN thrust but it only consumes 20W of power. If the thrust to power ratio is analyzed results are very similar to competitors. The designed device reaches a value of $0.32\frac{mN}{W}$, while the COMET and TunaCan present values of $0.31\frac{mN}{W}$ and $0.3\frac{mN}{W}$ respectively.

8.3 Mass and energy distribution

Mass and energy consumption for each of the components is identified and compared in this section. Both variables are very impactful and taken into account when designing the device, as has been stated previously.

Figure 8.3.1 shows the mass distribution for the components of the propulsion device, with the propellant and the aluminum components of the satellite such as the lids and the exterior shell taking up aluminum lids.

Total weight without the tank structure of 230g is achieved. With a propellant mass of 250g taking up 52% of the mass, aluminum parts (lids, exterior shell, and water accumulator) accumulate 38% of the device's weight (80% if the tank is not included). The superheater, nozzle, and heating wires end up being very small, enabling the device to be efficient even if working at high temperatures.

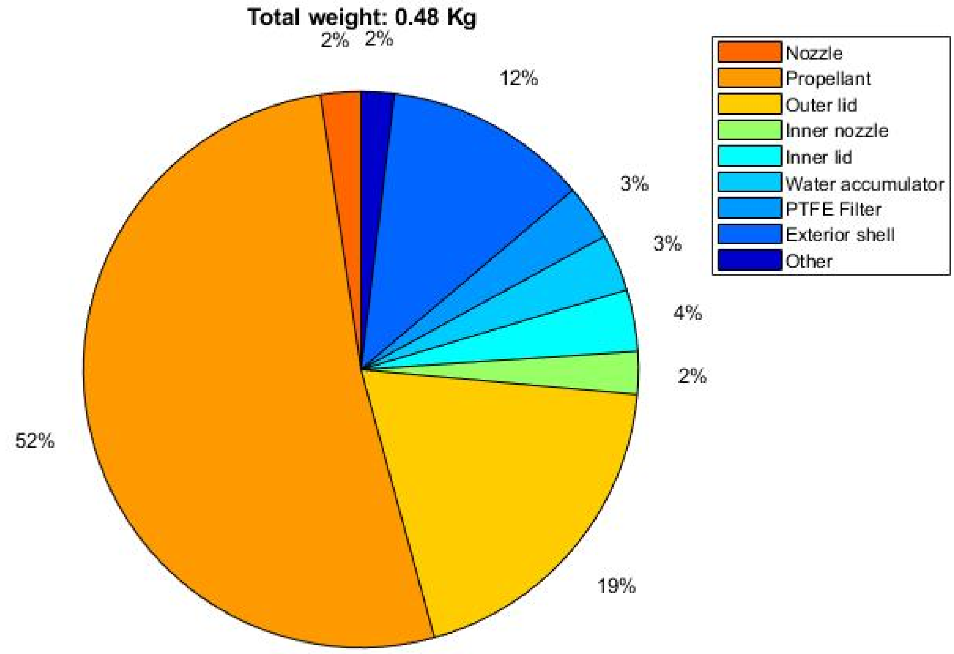

Figure 8.3.1: Mass distribution

The energy distribution is shown in figure 8.3.2 for case 1 since it's the most energy demanding. Energy is impacted by the components' mass, constant pressure specific heat, and temperature difference between idle and active states. While propellant takes up more of the mass budget, energy is stored in the outer and inner lids, and the exterior shell ends up representing most of the energy in the propulsion system, consuming 4.2Wh, 0.7Wh, and 2.6Wh respectively, and a total of 7.5Wh or 52% of the budget. Startup energy amounts to 14.39Wh if propellant is taken into account. Without propellant, 11.49Wh are consumed at startup. With the proposed pre-tank only 40g of propellant are heated instead of the full 250g tank. Heating the 250g of propellant from 283K (temperature at idle) to 345K would result in 17Wh of energy consumed by the propellant, more than the entirety of the current design. If only the pre-tank is heated, energy consumption decreases to 2.9Wh, resulting in a smarter use of the battery's energy.

Other inner components at higher temperatures store less energy even if the temperature difference between idle and active states is large. The superheater is the component with the second highest temperature difference aside from the superheater's resistor, storing 10% of the startup energy with a mass of less than 1% of the total. Aluminum parts require high startup energies due to their mass and their idle-active temperature differences of nearly 200K.

With 77Wh available, consumption of 14.4Wh represents 18.7% of the energy used in an

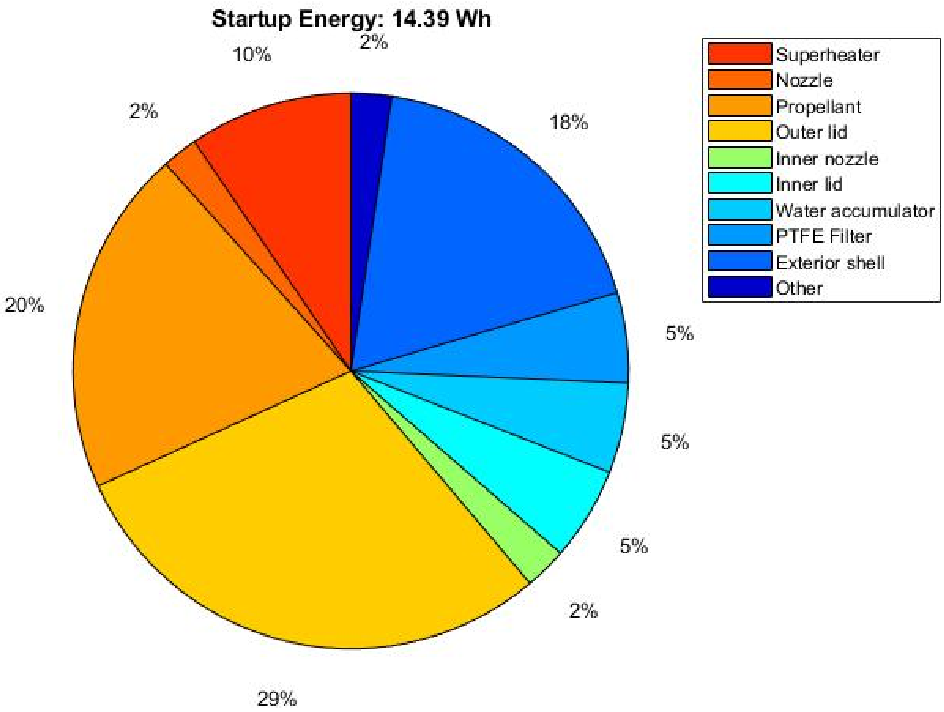

Figure 8.3.2: Startup Energy Distribution

impulse event, leaving 81.3% that is either used to heat the mass flow or is lost.

8.4 Resistors voltages and currents

Wire diameters and lengths that fulfill the energy bus requirements are found. Wire geometries, as well as their currents and applied voltages, are found in table 8.4.1 for active and idle cases.

	Superheater				Evaporator			
Case	l [mm]	d [mm]	V [V]	I [A]	l [mm]	d [mm]	V [V]	I [A]
Idle			0.34	0.56			0	0
Active 1	131.7	0.6438 (AWG 22)	5.12	8.31	1250	0.57404 (AWG 23)	5.78	0.83
Active 2			5.13	8.33			4.51	0.64

Table 8.4.1: Resistors geometry and electrical results

Both resistors operate at voltages below 6V and currents below 10.4A. When summing the active currents, 9.1A is consumed between the evaporator and superheater's resistors, allowing up to 1A consumption in the pre-tank. With a power consumption of 2.31W, 2.31V would establish the required current of 1A, or even better, with 6V a pre-tank current of 0.35A is required.

At idle, with power consumption at the superheater of 0.2W, voltage and current are below 1V and 1A respectively.

Different voltages are required to be applied in the resistors due to their geometries and how they interact with the solid components from a heat transfer standpoint, therefore at least 3 voltage regulators are required to achieve the required current and dissipated power in the resistors.

8.5 Efficiencies

Power conversion efficiency, energetic efficiency, and heat recovery from the superheater are calculated for the propulsion system. Efficiencies for both cases 1 and 2 are displayed in table 8.5.1.

	η_{power} [%]	η_{energy} [%]	$\eta_{recovery}$ [%]
Active 1	78.2	62.6	71.7
Active 2	81.1	67.6	79.7

Table 8.5.1: Efficiency results

Active case 2 has a higher energy and power conversion efficiency due to colder lids and exterior shell, which radiate less heat and also take up less of the battery's energy to reach adequate operation temperatures. Heat recovery for case 2 is higher since in this case, the accumulator's walls are at a lower temperature than the lids, therefore heat flowing through the insulation connectors is used to evaporate instead of leaving through the lids (see heat flow between nodes 4 and 9, and 6 and 9 in figures 8.1.1 and 8.1.2).

8.6 Specification sheet and comparison with existing products

Once all results are analyzed and presented a summary table is presented with the final specifications of the propulsion system. Table 8.6.1 shows all obtained variables for the device at this stage. Bradford's COMET and SteamJet's TunaCan Thruster are included so that specifications are compared. The minimum impulse bit for the device is not stated since it has to be tested, and the total mass with the tank is not yet given since the propellant to be carried depends on each mission.

Characteristic	Unit	Proposed Design	COMET-1000	TunaCan Thruster
Thrust	[mN]	16	17	6
Specific impulse	[s]	171-172	175	172
Active Power	[W]	48-49.6	55	19.9
Idle Power	[W]	0.2	0.25	0.12
Dimensions (without tank)	[mm x mm x mm]	75x75x70	100x100x90	ϕ80x40
Maximum Voltage	[V]	6	34-8	14-9
Required Current	[A]	9-10		
Satellite temperature	[K]	283-345	278-333	
Dry Mass (no tank, no propellant)	[g]	235		
Dry Mass (no propellant)	[g]		740	410
Startup energy (no tank)	[Wh]	11.49		
Startup time	[min]	23	10	

Table 8.6.1: Resistojet specifications

When comparing to existing superheated steam resistojets, the achieved thrust to power ratio for the designed device is within reported values, reaching values of $0.32\frac{mN}{w}$, with COMET and TunaCan Thruster reporting values of 0.31 and $0.30\frac{mN}{W}$ respectively, with similar specific impulse and using the same propellant.

A reasonable assumption to make is that nozzle efficiency is constant across the thrusters, since mass flow for the COMET should be similar and mass flow for the TunaCan Thruster should be even lower, occurring in both cases flow rarefaction, the main cause for nozzle's efficiency drop. With similar specific impulses, nozzle efficiencies, and thrust to power ratios, power conversion efficiencies should be comparable.

The designed device's startup time is more than doubles that of the COMET thruster. Since their power consumptions are almost equal, and as commented previously power efficiencies can be considered comparable, startup energy is a major fault of the proposed design. Although a pre-tank enabled energy savings during startup, the lids and the exterior shell should take a much less percentage of the battery's energy. Other hot components' startup energies can't be reduced since they are made as small as possible, with temperatures unable to be reduced due to fluid heating concerns and specific impulse loss.

Improvements could be made if another layer of insulation is designed between the evaporator and the lids. In this redesign, only the evaporating walls reach temperatures of 450K, instead of the entirety of the casing of the device. Assuming idle temperatures remain constant if temperatures of 350K are reached in the lids and exterior shell, energy consumption of these components would be halved. Considering they take up 52% of the startup energy, savings of a maximum 25% percent of the energy could be achieved, as the addition of new components would in part, reduce the energy efficiency gain as more mass is being added to the system.

The devices are similar in dimensions, all occupying less than 1U if the tank is not included.

9 Operation control proposal

The device's conceptual design is already determined. Dimensions are not yet fully defined but how the system will operate can be described. The control sequence for the first impulse event, and how each of the following events is described in this section.

Figure 9.1 shows the sensor and valve layout for the device. Information taken from sensors is used to open the various valves, with the control sequences described in the following sections.

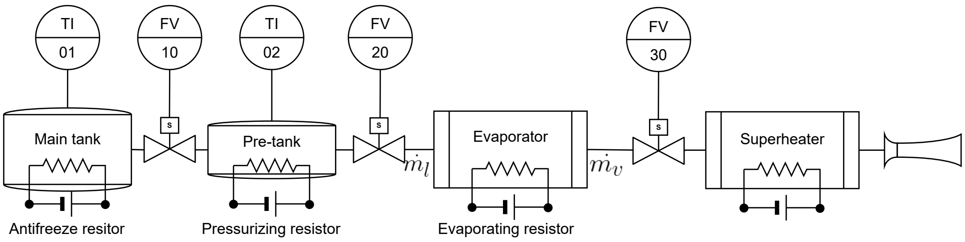

Figure 9.1: Propulsion system sensors layout

Sensing temperature in the superheater would be ideal, but at that temperature range, only metal thermocouples are available, and they can't be fit in a device this small without impacting efficiency negatively. Temperature is instead sensed at the inner lid, at temperatures below PTFE limit temperatures. This enables for use of cable thermocouples or even thermistors.

9.1 Operation preparation

As the operation begins, all valves are closed and valve 1 opens to fill the pre-tank, storing the necessary propellant for an impulse event. Both superheater and evaporator must be preheated through their resistors at lower voltages than at full operation since fluid doesn't take heat from the solid components. The superheater mustn't reach a temperature high enough which results in too overheated evaporating walls. The superheater is at a much lower temperature than at normal operating conditions since there is no fluid evaporation to act as a heat sink. The temperature difference between the walls and liquid propellant can't exceed 100K. The inner lid has a similar temperature to the accumulator walls, and the temperature sensor can provide information to regulate power in the superheater.

When the fuse is fully melted, valve 3 closes, and valve 2 opens slightly to allow flow into the evaporator. When walls reach an adequate temperature from preheating, they evaporate the lingering propellant and establish the target chamber pressure that along the filter retains fluid coming from a now open valve 2.

Once the water accumulator is filled, the superheater's temperature can be raised to its limit temperature at maximum power. If current and voltage are regulated, the wire never exceeds its limit temperature. When the solid components that receive heat from the wire are colder, the wire can dissipate the power determined by the electrical variables at a lower temperature.

In the transient stage, water keeps being evaporated, but valve 3 needs to be closed, otherwise, very low specific impulse fluid is discharged. This causes an increase in pressure, which is relieved by brief openings of valve 3. If valve 3 does not open, heat pressurizes the steam in the vapor chamber and liquid flows from the accumulator to the tank.

A fraction of the propellant is discharged at a lower specific impulse than the optimum at continuous operation due to exiting in the transient stage with a low-temperature superheater. This is unavoidable due to the chosen design. Water must be present at all times in the accumulator: evaporation imposes a temperature for the evaporating walls and most of the components as the lids and the exterior shell.

When the superheater is being heated and the evaporating resistor is turned off, at a given point the superheater finds an equilibrium temperature, at which the superheater's heat losses are enough to evaporate the mass flow imposed by the nozzle. At this stage valve, 3 is constantly open. When constant pressure is achieved, the evaporating resistor needs to be turned on and the system experiences a last unsteady state until a stationary state is reached.

9.2 Active control

The temperature at the superheater is unknown throughout the whole process, even if the temperature sensor in the inner lid helps when the device is turned on. Thermal inertia in the superheater, insulation, and inner lid is considerable, making it difficult to control power in the superheater due to the delay between the sent signal and the change in the temperature system. Once the superheater is safe to operate at full power, the system is only regulated by changing the power in the evaporating resistor.

The setpoint for the system is the chamber pressure which establishes the adequate mass flow to the superheater, obtained with the simulation model and later validated with experimental tests.

Chamber pressure will determine if the system is evaporating the correct amount of mass. An increase in pressure chamber occurs when evaporated mass $\dot{m}_{evap}$ is higher than the mass exiting through the nozzle $\dot{m}_{out}$. However, according to the left-hand side of equation 4.2.4 if pressure increases mass flow also increases, finding a new equilibrium between evaporation and mass exiting the system. If pressure at the vapor chamber is sensed, having the superheater working at its maximum power, power in the evaporator resistor can be regulated to change the mass flowing through the superheater.

According to the chamber pressure changes, different control actions are taken:

- Increase in pressure: evaporated mass flow too high, evaporating resistor's power should be decreased.
- Decrease in pressure: mass flow in the superheater is higher than evaporated mass, evaporating resistor's power should be increased. Decreases in pressure could be critical to the system if the mass flow reaches a point where the filter and water's surface tension can't hold the propellant in place and the steam chamber is flooded with liquid propellant.

9.3 Turning off

When the pre-tank is emptied, the remaining liquid water in the accumulator is evaporated quickly since the mass is low. Pressure in the chamber then descends abruptly, indicating that both superheating and evaporating resistors must be turned off. When chamber pressure reaches 0 valves 2 and 3 close. Once the batteries are charged, the system is ready to fire again.

9.4 Impulse bit operation

With a preheated superheater, valve 3 opens and closes as fast as possible, allowing very little mass into the superheater that will eventually exit through the nozzle. This can result in thrust during a short amount of time that can be measured during experimental testing. However, if this operation mode is used with the current design, preheating the superheater involves evaporating mass. With a closed valve 2, evaporating more mass and also heating the steam in the chamber leads to an increase in pressure that can lead to steam passing through the filter and to the liquid water accumulator and tank. In addition, the components can reach higher temperatures than in a steady-state, making it not safe for the propulsion system to operate under this regime.

10 Experimental setup

An experiment must be carried out to demonstrate the possibility of a low-pressure water vapor superheater with high energetic efficiency, reaching high vapor temperatures without intervening in chemical reactions. The following experiment is restricted to the ITBA's laboratory capacity.

A custom-built, vacuum chamber built-in 2012 for Satellogic is shown in figure 10.1. This vacuum chamber is fully instrumented for propulsion experiments and allows low-pressure experiments (approx 1.5 mbar) with mass flows below 0.5 g/min of non-condensable propellants. Due to the usage of water as a propellant, lower vacuum pressure is expected to be measured.

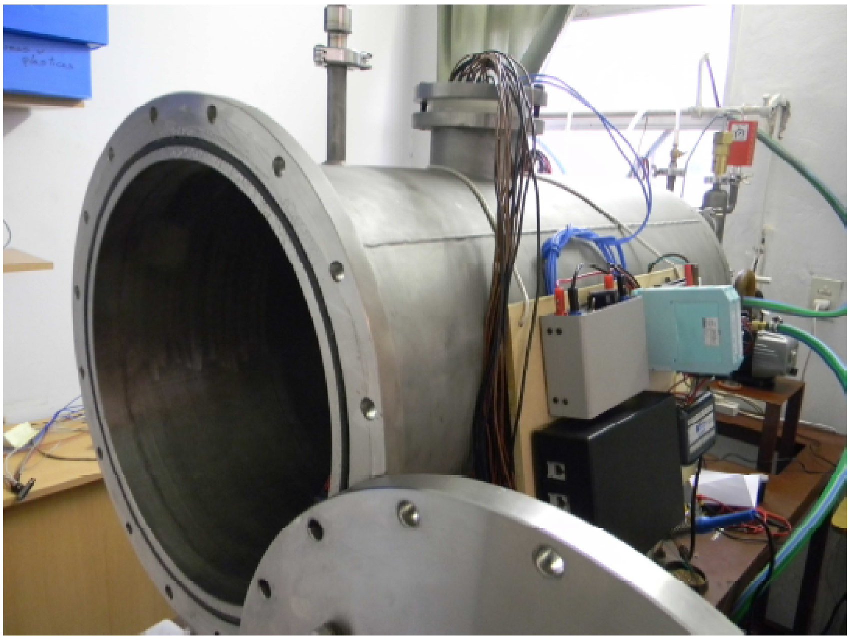

Figure 10.1: Vacuum chamber setup

To replicate real-life conditions whilst maintaining the individuality of each component, an experimental layout shown in figure 10.2 is proposed. Each component shows the necessary instrumentation needed. This setup allows the measurement of each subsystem individually. Redundant temperature measurements are taken to estimate and compensate for the heat losses due to the dismemberment of the propulsion system. Conceptually, the dismemberment is convenient because it allows the individual assessment of each subsystem's efficiency.

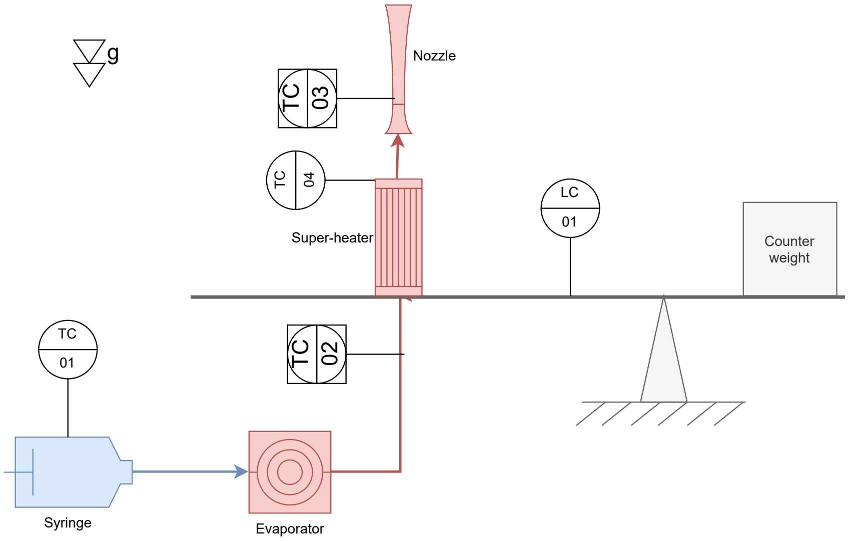

Figure 10.2: Experimental setup

With this dismemberment, the evaporator maintains a hydrophobic liquid/vapor barrier but presents a different geometrical distribution. The superheater element is, in essence, the same as the final piece - the only difference is the enclosure to fit into the vacuum chamber.

Electrical power applied to the superheater's resistor is obtained by measuring current and voltage independently. The voltage drop is measured directly in each resistance connection. DC regulated sources are used as a power source, which leads to stable measurements, although real-life applications are most likely to use switch voltage sources - much less stable. Power measurements resulting from experiments are expected to be different from both the simulation models and the final device, since heat recirculation is not present in the proposed experiment, and factors affecting heat transfer such as the vacuum chamber's area will greatly change heat losses from the superheater.

A challenging measurement is determining the mass flow of the system. Ideally, a microflow liquid adjusted sensor would be used, but, due to budget restrictions, an optical level sensor can be used - a graduated glass micropipette with a 3ml capacity. Triple distilled, deionized water is filled to a determined level and the level drop is measured. Taking care of placing the upper level of the micropipette above the discharge nozzle, a wireless camera will record the level drop at determined time intervals. A better measurement would become by measuring the time it takes for the water level to drop at regular intervals.

As in all resistor-heated elements, the system presents considerable thermal inertia. An additional reservoir is needed to compensate for the preheating process. A microvalve switches water intake from the reservoir to a graded micropipette once the regime is established.

Finally, once the correct instruments are determined, error propagation is needed to establish the uncertainty range. Estimates establish this range below the 5% threshold, although, to be conservative, a 10% is established.

11 Conclusions

Even though no experimental results have been obtained at this point, a series of conclusions can be made with the work described in sections 1 to 10. First and foremost, a green, non-toxic propulsion system with few moving parts is designed.

A parametric thermal model is achieved, in which a previous design can be adapted for any mission requirement, or if new thermal circuits are created, the performance of various designs can be evaluated. This model allows the user to quickly determine dimensions, resistors, and powers needed depending on their requirements.

According to the models used, with the final resistojet design the proposed specifications are met, except for the specific impulse target. One of the problems found is related to the low volume to be occupied by the device, limiting insulation strategies with the need to achieve a very high thermal gradient between the superheater and the radiating surface. In addition, the type of propulsion system along with the chosen propellant makes nozzle efficiency losses unavoidable. Rarefaction impacts nozzle efficiency by 20% according to previously cited studies and is always present when low pressures and low mass flows are required. If tank pressure is to be raised to avoid this effect, the main advantages of choosing a self-pressurizing resistojet are lost, having a more complex, heavier tank with high startup energy requirements. The model can be used with a lower viscosity propellant resulting in reduced rarefaction, but since the system is a complex equilibrium where a lot of thermodynamic variables such as latent heat, vapor pressure, and specific enthalpy among others are involved, knowledge from this design can not be extrapolated.

Clever design leads to a viable propulsion system able to fit in a single CubeSat unit. Utilization of heat losses from a high-temperature zone as the superheater, and quasi-constant I_{sp} and thrust are obtained at a satellite temperature range between 0 and 60°C. However, impulse bit operation is very limited for the device when the evaporator and the superheater are so heavily coupled.

The designed propulsion system shows promise of respectable specifications for CubeSats up to 12U, using typical power buses for its category. I_{sp}, F, and η obtained are comprable to those from existing water resistojet systems such as SteamJet Space Systems' TunaCan Thruster or Bradford's COMET. This indicates that even if the model is not fully calibrated and could be further improved, especially to evaluate transient responses, understanding of a very complex thermal system is achieved, and the thermodynamic limitations for improving the resistojet performance are identified.

Testing needs to be performed on every subsystem separately, allowing for model corrections according to experimental data. Models can then be readjusted and final tuning of the system can be performed once again.

Experimental testing of the subsystems to achieve up to TRL 3 (concept validation) can be achieved in the university's vacuum chamber for every subsystem, except for the evaporator which would need an extended period of microgravity, reachable with a zero-g flight or, even better, the experimental deployment of one of these devices.

References

[1] Poghosyan Armen and Golkar Alessandro. "CubeSat evolution: Analyzing CubeSat capabilities for conducting science missions". In: *Progress in Aerospace Sciences* 88 (Jan. 2017), pp. 59–83. DOI: 10.1016/j.paerosci.2016.11.002.

[2] ESA Earth Observation Data. *Flock 1 Constellation*. https://earth.esa.int/web/eoportal/satellite-missions/f/flock-1. Accessed on 2020-08-05.

[3] ESA Earth Observation Data. *MarCO*. https://directory.eoportal.org/web/eoportal/satellite-missions/content/-/article/marco. Accessed on 2020-08-05.

[4] Wiley J. Larson and James R. Wertz. In: *Space mission analysis and design*. 3rd ed. Kluwer Academic Publishers, 2005. Chap. 7, 17.

[5] A.R. Tummala and A. Dutta. "An Overview of Cube-Satellite Propulsion Technologies and Trends". In: *Aerospace* 4 (Dec. 2017). DOI: 10.3390/aerospace4040058.

[6] Robert P. Benedict. *Fundamentals of Pipe Flow*. Wiley-Interscience Publication, 2011. Chap. 1, pp. 588, 589.

[7] California Polytechnic State University. *CubeSat Design Specification*. https://static1.squarespace.com/static/5418c831e4b0fa4ecac1bacd/t/56e9b62337013b6c063a655a/1458157095454/cds_rev13_final2.pdf. Accessed on 2020-08-05.

[8] Bradford. *Comet - Water-based smallsat propulsion*. https://www.bradford-space.com/products-comet-smallsat-propulsion.php. Accessed on 2020-08-05.

[9] SteamJEt. *Steamjet - Water-based Smallsat Propulsion*. https://steamjet.space/. Accessed on 2020-08-05.

[10] Stefano Rossi and Anton Ivanov. "THERMAL MODEL FOR CUBESAT: A SIMPLE AND EASY MODEL FROM THE SWISSCUBE'S THERMAL FLIGHT DATA". In: Sept. 2013.

[11] Haibo MA et al. "Thermal Analysis Modeling and On-orbit Temperature Prediction for a Microsatellite with Multilayer Insulation". In: *TRANSACTIONS OF THE JAPAN SOCIETY FOR AERONAUTICAL AND SPACE SCIENCES* 60.2 (2017), pp. 93–102. DOI: 10.2322/tjsass.60.93.

[12] GOMspace. *GOMspace NanoPower BPX Datasheet*. https://gomspace.com/UserFiles/Subsystems/datasheet/gs-ds-nanopower-bpx-3-18.pdf. Accessed on 2020-08-05.

[13] AAC Clyde Space. *AAC Clyde Space OPTIMUS Battery Datasheet*. https://www.aac-clyde.space/assets/000/000/079/OPTIMUS_original.pdf?1564954960. Accessed on 2020-08-05.

[14] AAC Clyde Space. *AAC Clyde Space STARBUCK-NANO Power conditioning and distribution units Datasheet*. https://www.aac-clyde.space/assets/000/000/103/STARBUCK-NANO_original.pdf?1565681302. Accessed on 2020-08-05.

[15] Frank Kreith. *Principles of heat transfer*. Cengage Learning, 1980. Chap. 1, all.

[16] Alak Bandyopadhyay and Alok Kumar Majumdar. "Modeling of Compressible Flow with Friction and Heat Transfer Using the Generalized Fluid System Simulation Program (GF-SSP)". In: 2007.

[17] NASA. *Isentropic flow equations*. `https://www.grc.nasa.gov/WWW/K-12/rocket/isentrop.html`. Accessed on 2020-08-05.

[18] Jonathan Dyer. *Rocket Performance and Efficiency*. Notes from class. Dec. 2020.

[19] Magnus Holmgren. *X Steam, Thermodynamic properties of water and steam*. (https://www.mathworks.com/matlabcentral/fileexchange/9817-x-steam-thermodynamic-properties-of-water-and-steam), MATLAB Central File Exchange. Retrieved December 8, 2020. Dec. 2020.

[20] Wolfgang Wagner et al. "New Equations for the Sublimation Pressure and Melting Pressure of H2O Ice Ih". In: *Journal of Physical and Chemical Reference Data* 40.4 (2011), p. 043103. DOI: `10.1063/1.3657937`.

[21] Robert D. Cook. *Concepts and Applications of Finite Element Analysis*. Wiley; 4th edition, 2001. Chap. 1, all.

[22] Kanthal. *Kanthal APM*. `https://www.kanthal.com/en/products/material-datasheets/wire/resistance-heating-wire-and-resistance-wire/kanthal-apm/`. Accessed on 2021-08-05.

[23] G. Neuer. *Spectral and total emissivity measurements of highly emitting materials*. 1995. Chap. 16, pp. 257, 265.

[24] Isidoro Martinez. *Radiative View Factors*. `http://webserver.dmt.upm.es/~isidoro/tc3/Radiation%20View%20factors.pdf`. Accessed on 2021-05-05.

[25] *Technical Ceramics*. `https://www.final-materials.com/gb/199-technical-ceramics`. Accessed on 2021-05-05.

[26] Fiberfrax. *Durablanket Spec Sheet*. `http://www.aislantessh.com.ar/web/wp-content/uploads/2018/07/Fibra-ceramica-manta.pdf`. Accessed on 2021-05-05.

[27] Final Advanced Machined Materials. *Landing Page*. `https://www.final-materials.com/gb/`. Accessed on 2021-05-05.

[28] AZO Materials. *Zirconia - ZrO2, Zirconium Dioxide*. `https://www.azom.com/properties.aspx?ArticleID=133`. Accessed on 2021-05-05.

[29] John H. Henninger. *Solar absorptance and thermal emittance of some common spacecraft thermal-control coatings*. NASA, 1984. Chap. 1, all.

[30] Toshiharu Oka et al. "Pool Boiling Heat Transfer in Microgravity : Experiments with CFC-113 and Water Utilizing a Drop Shaft Facility". In: *JSME International Journal Series B* 39.4 (1996), pp. 798–807. DOI: `10.1299/jsmeb.39.798`.

[31] Christopher Konishi and Issam Mudawar. "Review of flow boiling and critical heat flux in microgravity". In: *International Journal of Heat and Mass Transfer* 80 (Jan. 2015), pp. 469–493. DOI: `10.1016/j.ijheatmasstransfer.2014.09.017`.

[32] TIM Tronics. *Red Ice Series*. https://www.timtronics.com/high-temperature/#Thermal-Greases. Accessed on 2021-07-05.

[33] F. Torre. "Gas flow in miniaturized nozzles for micro-thrusters". In: (Feb. 2022).

[34] W. Louisos et al. "Design considerations for supersonic micronozzles". In: *IJMR* 3 (Jan. 2008), pp. 80–113. DOI: 10.1504/IJMR.2008.016453.

[35] M. Ivanov et al. "Numerical Study of Cold Gas Micronozzle Flows". In: (Jan. 1999), p. 15. DOI: 10.2514/6.1999-166.

[36] Feng Zhang et al. "Normal spectral emissivity measurement of Al6061 in air environment". In: *Proceedings of SPIE - The International Society for Optical Engineering* 9623 (Aug. 2015). DOI: 10.1117/12.2193513.

[37] Classic Filters. *New 40 micron grade PTFE Filter Elements*. https://www.classicfilters.com/blog/new-40-micron-grade-ptfe-filter-elements. Accessed on 2020-08-05. Jan. 2020.

[38] *LPV NW08 Low Pressure Valve*. http://www.ast-space.com/Files/Other/Documents/low%20pressure%20valve%20LPV%20datasheet%20NW08.pdf. Accessed on 11/24/2020.

[39] *KE 1092 Bare wire thermocouple*. https://www.thermo-electra.com/getpdf.php?product=200&taal=en. (Accessed on 11/22/2020).